Hierarchical modeling of length-dependent force generation in cardiac muscles and associated thermodynamically-consistent numerical schemes

François Kimmig, Philippe Moireau, Dominique Chapelle

Hierarchical modeling of length-dependent force generation in cardiac muscles and associated thermodynamically-consistent numerical schemes

François Kimmig[1,2], Philippe Moireau[2,1], and Dominique Chapelle[2,1]

[1]LMS, CNRS, École polytechnique, Institut Polytechnique de Paris, France
[2]Inria, France

Abstract

In the context of cardiac muscle modeling, the availability of the myosin heads in the sarcomeres varies over the heart cycle contributing to the Frank-Starling mechanism at the organ level. In this paper, we propose a new approach that allows to extend the Huxley'57 muscle contraction model equations to incorporate this variation. This extension is built in a thermodynamically consistent manner, and we also propose adapted numerical methods that satisfy thermodynamical balances at the discrete level. Moreover, this whole approach — both for the model and the numerics — is devised within a hierarchical strategy enabling the coupling of the microscopic sarcomere-level equations with the macroscopic tissue-level description. As an important illustration, coupling our model with a previously proposed simplified heart model, we demonstrate the ability of the modeling and numerical framework to capture the essential features of the Frank-Starling mechanism.

Keywords – Cardiac modeling, numerical methods, biomechanics, Frank-Starling mechanism, multi-scale modeling

1 Introduction

Cardiac muscles are made of a set of fibers themselves composed of elementary contractile units in series called sarcomeres. The sarcomeres are mainly made of two types of protein filaments: myosin filaments (also called thick filaments) and actin filaments (also called thin filaments). The myosin heads of the thick filaments interact with the actin sites of the thin filament in a cycle that involves, among other stages, the attachment of the myosin head on an actin site, the production of force and the detachment of the myosin heads. The macroscopic muscle shortening is then the result of the microscopic relative sliding between the myosin and actin filaments. At rest, the binding of the myosin heads on the actin sites is prevented. The contraction is triggered by the release in the muscle cell cytosol of calcium ions that bind to the actin sites and activate them, ultimately allowing the attachment of myosin heads. The thin filament activation is a transient process composed of an activation phase when calcium is released and a deactivation phase when calcium is taken from the cytosol.

In living conditions, the heart contraction is regulated by two main pathways: an *intrinsic* one, which varies the force as a function of the sarcomere stretch – a higher sarcomere length being generally associated with a higher force – and an *extrinsic* pathway corresponding to the control of the nervous system through neuroendocrine mediators [Silverthorn et al., 2009]. These two regulations modulate the force developed by the muscle cells. At the organ level, the intrinsic regulation results in the so-called *Frank-Starling effect* [Frank, 1895; Patterson & Starling, 1914]. This regulation ensures that there is a monotone relation between the end-diastolic volume and the ejection pressure [de Tombe et al., 2010]. It implies that the ejected volume (called *stroke volume*) varies in the same way as the filling volume.

The exact origin of these intrinsic variations is still the subject of active research [de Tombe & ter Keurs, 2016; Sequeira & Velden, 2017]. In all generality, the modulation of the force with the sarcomere length may result either from an change in the force generated by each cross-bridge or from a change in the number of attached cross-bridges (or from both mechanisms combined). The works of Wannenburg

et al. [1997], Amiad Pavlov & Landesberg [2016] and Caremani et al. [2016] show that the cross-bridge properties are not affected by variations of the sarcomere length or the level of calcium supply, leading to the conclusion that neither is the force developed by each cross-bridge. This statement has been recently further supported by a direct assessment of the non-variation of the cross-bridge force with the level of thin filament activation that has been performed by Pinzauti et al. [2018]. As a result, the force variation with the sarcomere length is only due to a change in the number of cross-bridges formed. This effect itself may have two distinct origins: a variation of the number of available myosin heads or a change in the level of the thin filament activation. In this paper, we focus on the variation of the number of available myosin heads as a function of the sarcomere length.

To isolate the effects of this variation, we consider experimental data in which the possibility of a variation of the thin filament activation is eliminated. To create these conditions, experimentalists either used skinned cells so that they can artificially maintain the "intracellular" calcium concentration at a high value ensuring that all actin sites are activated [Kentish et al., 1986; Dobesh et al., 2002], or force a large enough release of calcium in intact cells and maintain this state [ter Keurs et al., 2008], in which case the cells are said to be in a tetanised state. The experimental results show a monotonous increase of the force with increasing sarcomere length that is solely due to the thick filament activation variation (the experimental data points are presented in Figure (8)b).

The time scale of the force adaptation to the sarcomere length has been studied by [Mateja & de Tombe, 2012]. Comparing the force dynamics for muscle samples starting at different sarcomere lengths and brought to the same sarcomere length just before activation, they observe no significant difference in the muscle behavior for pre-activation length changes as fast as 5 ms. This shows that the regulation dynamics occurs at a much lower time scale. The time scale of the attachment and detachment rates being 25 ms and 100 ms, respectively, if the calibration focuses on the tension rise dynamics [de Tombe & Stienen, 2007], and 4 ms and 16 ms, respectively, if the calibration focuses on the classical force-velocity curve [Kimmig & Caruel, 2019], the thick filament regulation thus occurs at a time scale that is smaller than that of the attachment-detachment process. As was also concluded by [Mateja & de Tombe, 2012], we will thus assume that the regulation mechanism can be considered as instantaneous.

Muscle contraction is often described by a family of models deriving from the seminal Huxley'57 model [Huxley, 1957; Eisenberg et al., 1980; Piazzesi & Lombardi, 1995; Marcucci & Truskinovsky, 2010; Marcucci & Yanagida, 2012; Caruel et al., 2019; Kimmig & Caruel, 2019]. To account for the regulation mechanisms involving the variation of the thick and thin filament level of activation, modifications of the Huxley'57 model equations have been previously proposed [Zahalak & Motabarzadeh, 1997; Chapelle et al., 2012]. They consist in modifying the expression of the law of mass action that describes the attachment-detachment process. However, this approach suffers from some limitations. In particular, it fails to be thermodynamically compatible. An alternative approach has been proposed by Marcucci et al. [2017] to model the varying thick filament activation. It considers the newly discovered myosin head state called off-state (as opposed to the classical on-state) in which the myosin head is folded back on the thick filament backbone. The on- and off- states are related by chemical transitions. A myosin head in the off-state cannot participate in the attachment-detachment process; to do so it must first transition to the on-state. It remains nevertheless unclear — because of a lack of data for cardiac muscle — whether the time scale of the on-off transition is compatible with the time scale of the length dependent thick filament activation.

In this paper, we propose an original and general paradigm that extends the Huxley'57 model equations to include the varying myosin heads availability. We introduce two groups of myosin heads and deduce the governing equations from conservation laws. The consistency with the thermodynamic principles of this modeling framework is then demonstrated. Note that we focus on the modeling of the thick filament activation mechanism, the thin filament activation being phenomenologically represented. The regulation of the myosin availability contributes to the Frank-Starling mechanism, which operates at the organ level. We thus want to link our new model with a numerical heart model to evaluate its capability to transfer properties from the micro-scale to the macro-scale. Such a multi-scale approach has indeed shown essential for performing physiologically relevant simulations in various area of cardiac modeling [Sugiura et al., 2012; Chabiniok et al., 2012; Baillargeon et al., 2014; Rossi et al., 2014; Chabiniok et al., 2016; Hirschvogel et al., 2017; Quarteroni et al., 2017; Niestrawska et al., 2020]. This motivates the introduction of dedicated discretization methods of our model that we design with the aim of satisfying discretized versions of the thermodynamical principles. Some elements of validation of our model are

presented with the simulation of heartbeats. These results are obtained through the coupling of our model with a simplified geometry heart model [Caruel et al., 2013a].

This paper is organized as follows. In Section 2, we briefly recall the Huxley'57 model and present the derivation of our new paradigm. The thermodynamic principles associated with this new model are established in Section 3. In Section 4, we explore the limits of our model and its relation with the previously proposed formulations. Adapted numerical methods are developed for our model in Section 5 and the thermodynamic compatibility of the discretization scheme is justified. The model calibration and the numerical results illustrating the ability of the model to reproduce the Frank-Starling mechanism are finally presented in Section 6.

2 Model presentation

Our goal is to propose a modeling framework that is able to incorporate the variation of the myosin heads availability into the classical equations describing the actin-myosin interaction. We first summarize present the muscle contraction models based on the seminal work of A.F. Huxley [Huxley, 1957]. Then, we introduce our formalism and derive the equations governing the dynamics of the system from the conservation of myosin heads. Finally, we put our new approach into perspective by comparing it to existing formulations.

2.1 Contraction model - Huxley'57 model family

The mathematical description of muscle contraction has its origin in the seminal work of Huxley [1957], which has been abundantly extended since then [Huxley & Simmons, 1971; Eisenberg & Hill, 1978; Eisenberg et al., 1980; Piazzesi & Lombardi, 1995; Zahalak, 2000] but remains the standard framework of modern models [Caremani et al., 2015; Marcucci et al., 2016; Caruel et al., 2019]. In particular, this approach has proven to be well-adapted to the modeling of mammals cardiac muscles [Månsson, 2010; Pertici et al., 2018; Kimmig & Caruel, 2019]. This family of models considers a collection of chemical states representing attached and detached myosin heads, interacting with each other according to the law of mass action. A general presentation of the Huxley'57 model and its extensions can be found in [Kimmig et al., 2019].

We will restrict our presentation to a two-state model – with one attached state and one detached state – which is sufficiently refined to capture the essential features of cardiac muscle contraction [Kimmig & Caruel, 2019]. However, the modeling ingredient presented in the present work could be easily extended to any model derived from the Huxley'57 model. The dynamics of attachment and detachment is described in the framework of the so-called *sliding filament theory*. The myosin and actin filaments are assumed to be rigid, meaning that the distance between consecutive myosin heads or consecutive actin sites is constant. Moreover, we assume that each myosin head interacts with its nearest actin site only. Actin sites are uniformly distributed along the actin filament and are separated by a distance d_a. Myosin heads are also uniformly distributed along the myosin filament but with a different spatial periodicity. The approach is centered on the myosin heads and a myosin head is parametrized by the distance between its rest position and its nearest actin site. This distance is denoted by s (see Figure 1) and we denote the interval of possible values of s by $[s^-, s^+]$ with $s^+ - s^- = d_a$. Note that this interval may be non-symmetric. Due to the difference in spatial periodicity between the actin and the myosin filaments, all positions $s \in [s^-, s^+]$ of the myosin heads are equiprobable in the population.

We now consider the subset of myosin heads located at distance s to their nearest actin site. The energy of the attached heads is given by $w_1(s)$ and that of the detached heads by w_0, which does not depend on the spatial variable. When a myosin head detaches, it uses an energy input μ_T brought by ATP to retrieve its original energy level. The transitions between the attached and the detached states are governed by the transition rate $k_+(s)$ for the attachment and $k_-(s)$ for the detachment. We assume that these two transitions are each associated with a reverse transition (see Figure 1) whose rate satisfies the detailed balance [Hill, 1977]

$$\frac{k_+(s)}{k_+^{\text{rev}}(s)} = \exp\left[\frac{w_0 - w_1(s)}{k_B T}\right], \qquad \frac{k_-(s)}{k_-^{\text{rev}}(s)} = \exp\left[\frac{w_1(s) + \mu_T - w_0}{k_B T}\right],$$

where T is the temperature and k_B the Boltzmann constant.

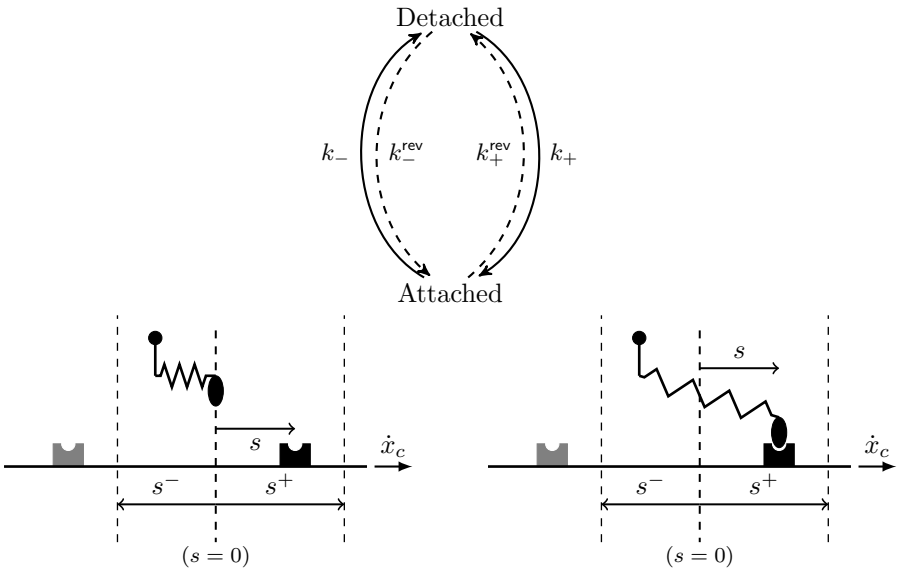

Figure 1: Presentation of the two-state model. Top: transitions between the attached state and the detached state and the associated transition rates. Bottom left: detached state model parametrization. Bottom right: attached state model parametrization.

The probability of being attached for a head in this subset at time t is denoted by $P_1(s,t)$ and we denote by $P_0(s,t)$, the probability of being detached. The conservation of matter leads to the following dynamics equations, for all $t>0$ and all $s\in[s^-,s^+]$

$$\begin{cases}\partial_t P_1(s,t)+\dot{x}_c\partial_s P_1(s,t)=\big(k_+(s)+k_-^{\text{rev}}(s)\big)P_0(s,t)-\big(k_-(s)+k_+^{\text{rev}}(s)\big)P_1(s,t),\\ \partial_t P_0(s,t)+\dot{x}_c\partial_s P_0(s,t)=\big(k_+(s)+k_-^{\text{rev}}(s)\big)P_0(s,t)-\big(k_-(s)+k_+^{\text{rev}}(s)\big)P_1(s,t),\end{cases} \tag{1}$$

where x_c is defined as the sarcomere extension and $\dot{x}_c$ is its time derivative. Note that the Eulerian nature of this description leads to the presence of transport terms which take into account the change in position when the myosin and actin filaments slide along each other with the velocity $\dot{x}_c$.

The single actin site assumption implies that the probability of being attached must vanish on the boundaries of the interval $[s^-,s^+]$. As proposed by Kimmig et al. [2019], we choose periodic boundary conditions $P_1(s^-,t)=P_1(s^+,t)$ and enforce the property $P_1(s^-,t)=P_1(s^+,t)=0$ through an appropriate choice of the transition rates.

Enforcing the necessary initial conditions $P_1(s,t=0)+P_0(s,t=0)=1,\ s\in[s^-,s^+]$, the probability P_0 is given for all $t>0$ and for all $s\in[s^-,s^+]$ by $P_0(s,t)=1-P_1(s,t)$ and (1) becomes

$$\begin{cases}\partial_t P_1(s,t)+\dot{x}_c\partial_s P_1(s,t)=\big(k_+(s)+k_-^{\text{rev}}(s)\big)P_0(s,t)-\big(k_-(s)+k_+^{\text{rev}}(s)\big)P_1(s,t),\\ P_0(s,t)=1-P_1(s,t).\end{cases}$$

Note that the original Huxley'57 model equations can be straightforwardly retrieved by defining the aggregated attachment rate f and detachment rate g by

$$\begin{vmatrix} f(s)=k_+(s)+k_-^{\text{rev}}(s),\\ g(s)=k_-(s)+k_+^{\text{rev}}(s).\end{vmatrix}$$

2.2 Incorporation of the variations in myosin availability level in the model equations

As part of the intrinsic regulation of the thick filament, the sarcomere stretch directly influences the level of availability of the myosin heads. To build our model, we extend the two-state model presented in Section 2.1. In addition to its natural assumptions, we assume that only a subpart of the myosin

heads population is available for attachment, while the remaining part is not available. Depending on their availability status, the myosin heads are grouped into two pools. In each pool, myosin heads can be attached or detached. The repartition of the heads between the two pools depends on the sarcomere stretch. For thermodynamical reasons, heads that are not available for attachment are not strictly prevented from attaching, but their attachment rate is much reduced compared to heads available for attachment. We also assume that heads change from one pool to the other independently of their attachment state (attached or detached). In this exchange process, we do not track the myosin heads individually but instead focus on average quantities. We thus propose a homogenized description of the myosin heads within the pools. Since we know that the thick filament regulation occurs at a fast time scale compared to the cycling time scale, the transfers between pools are supposed to take place instantaneously.

It is important to note that this modeling framework is not specific to any particular mechanism underlying the regulation of the myosin heads availability, but is instead fully general.

To describe the state of a myosin head, we introduce an additional – discrete and deterministic – internal variable γ that is equal to one if the head is available for attachment and equal to zero if it is not. As a consequence, we are now considering $P_1(s,t,\gamma)$ the probability of being attached for the subset of heads located at a distance s to their nearest actin site and belonging to the pool γ at time t. The probability of being detached for the same subset is denoted by $P_0(s,t,\gamma)$; it is linked to P_1 through the relationship

$$P_1(s,t,\gamma) + P_0(s,t,\gamma) = 1, \quad s \in [s^-, s^+],\ t > 0,\ \gamma \in \{0,1\}.$$

Note that γ is somewhat comparable to s meaning that both can change when following actual myosin heads, albeit γ is discrete while s is continuous.

We call scaled number of heads the number of heads considered divided by the total number of heads (sum of the number of heads in each pool). The scaled number of heads available for attachment is denoted by $n_0(e_c)$. It solely depends on the relative extension e_c, which is linked to the relative displacement of the rigid filaments x_c by $x_c = \ell_{hs} e_c$, where ℓ_{hs} is the *half-sarcomere slack length*. The latter is defined as the half-sarcomere length corresponding to zero passive force in the sarcomere. The total probability of being attached is obtained as the weighted average between the two pools. It is given by

$$P_1(s,t) = n_0 P_1(s,t,1) + (1-n_0) P_1(s,t,0). \tag{2}$$

The energy levels of the attached and detached states are the same in each pool because the transfer of a myosin head from one pool to the other is not associated with any energy input. The attached and detached state energy levels are still denoted by $w_1(s)$ and w_0, respectively. However, myosin heads experience two distinct chemical cycles in the two pools. The transitions rates are still defined as in Figure 1, but are now indexed by the variable γ. They satisfy the detailed balance in each pool, i.e.

$$\frac{k_{+,\gamma}(s)}{k^{\text{rev}}_{+,\gamma}(s)} = \exp\Big[\frac{w_0 - w_1(s)}{k_B T}\Big], \quad \frac{k_{-,\gamma}(s)}{k^{\text{rev}}_{-,\gamma}(s)} = \exp\Big[\frac{w_1(s) + \mu_T - w_0}{k_B T}\Big],\ \gamma \in \{0,1\}. \tag{3}$$

The non-availability of the myosin heads in the pool $\gamma = 0$ is modeled with the choice $k_{+,1} \gg k_{+,0}$.

To describe the dynamics of the system, we write the conservation of myosin heads in a closed system. For that purpose, we consider the sub-ensemble of heads that, in each pool, are located at a distance s to their nearest actin site. We describe the dynamics of these heads following them "in their motion". We obtain the following dynamics for all $s \in [s^-, s^+]$

$$\begin{cases} \dfrac{\mathrm{d}}{\mathrm{d}t} P_1(s,t,1) = \big(k_{+,1}(s) + k^{\text{rev}}_{-,1}(s)\big) P_0(s,t,1) - \big(k_{-,1}(s) + k^{\text{rev}}_{+,1}(s)\big) P_1(s,t,1), \\ \dfrac{\mathrm{d}}{\mathrm{d}t} P_1(s,t,0) = \big(k_{+,0}(s) + k^{\text{rev}}_{-,0}(s)\big) P_0(s,t,0) - \big(k_{-,0}(s) + k^{\text{rev}}_{+,0}(s)\big) P_1(s,t,0), \\ P_0(s,t,\gamma) = 1 - P_1(s,t,\gamma). \end{cases} \tag{4}$$

Equation (4) uses total derivatives, which follow the myosin heads in their evolution. To fully establish the system dynamics, we need to make these total derivatives explicit. Note that γ is a discrete parameter and thus cannot be treated with the classical chain rule formula. We consider the ensemble of heads located at distance s of the nearest actin site, and that are in the pool $\gamma = 1$. The probability of being attached for this ensemble of heads at time t is given by $P_1(s,t,1)$.

At time $t+\tau$, we denote by $\hat{P}_1$ the probability of being attached for this very same ensemble of heads, now at distance $s+\delta$ from the nearest actin site. Because of the system evolution happening between t and $t+\tau$, some of the heads in the ensemble considered, which are in the pool of available heads ($\gamma=1$) at time t, may move to the pool of unavailable heads ($\gamma=0$) at time $t+\tau$. This has to be taken into account in the computation of $\hat{P}_1$.

We define

$$|x|_+ = \begin{cases} x & \text{if } x \geq 0, \\ 0 & \text{otherwise,} \end{cases} \qquad \text{and} \qquad |x|_- = \begin{cases} -x & \text{if } x \leq 0, \\ 0 & \text{otherwise,} \end{cases}$$

so that

$$x = |x|_+ - |x|_-. \tag{5}$$

The scaled number of heads in the ensemble considered that are in the pool $\gamma=1$ being given by n_0, the scaled number of heads switching from the pool $\gamma=0$ to the pool $\gamma=1$ between the times t and $t+\tau$ is given by $|\dot{n}_0|_+\tau + o\big(\tau\big)$ and the scaled number of heads switching from the pool $\gamma=1$ to the pool $\gamma=0$ in the same time interval is given by $|\dot{n}_0|_-\tau + o\big(\tau\big)$.

We first consider the case where $\dot{n}_0 > 0$. Note that, with our homogenized description, this implies that there is no head switching from the pool $\gamma=1$ to the pool $\gamma=0$. At time $t+\tau$, the myosin heads in the ensemble considered are the heads of the pool $\gamma=1$ minus the heads that switched from the pool $\gamma=0$ in the time interval τ. The count of attached heads thus gives

$$n_0\hat{P}_1 = \big[n_0 + |\dot{n}_0|_+\tau\big]P_1(s+\delta, t+\tau, 1) - |\dot{n}_0|_+\tau P_1(s,t,0) + o\big(\tau\big) + o\big(\delta\big). \tag{6}$$

At the first order, (6) becomes

$$n_0\hat{P}_1 = n_0 P_1(s+\delta, t+\tau, 1) + |\dot{n}_0|_+\tau\big[P_1(s,t,1) - P_1(s,t,0)\big] + o\big(\tau\big) + o\big(\delta\big). \tag{7}$$

We now consider the case where $\dot{n}_0 < 0$. At time $t+\tau$, the myosin heads in the ensemble considered are the heads of the pool $\gamma=1$ plus the heads that switched to the pool $\gamma=0$ in the time interval τ. We thus have

$$n_0\hat{P}_1 = \big[n_0 - |\dot{n}_0|_-\tau\big]P_1(s+\delta, t+\tau, 1) + |\dot{n}_0|_-\tau P_1(s,t,1) + o\big(\tau\big) + o\big(\delta\big). \tag{8}$$

At the first order, (8) becomes

$$\hat{P}_1 = P_1(s+\delta, t+\tau, 1) + o\big(\tau\big) + o\big(\delta\big). \tag{9}$$

Altogether, for $\dot{n}_0$ positive or negative, (7) and (9) yield

$$\hat{P}_1 = P_1(s+\delta, t+\tau, 1) + \frac{|\dot{n}_0|_+}{n_0}\tau\big[P_1(s,t,1) - P_1(s,t,0)\big] + o\big(\tau\big) + o\big(\delta\big).$$

We obtain

$$\frac{\mathrm{d}}{\mathrm{d}t}\Big(P_1(s,t,1)\Big) = \lim_{\tau\to 0}\frac{\hat{P}_1(s,t) - P_1(s,t,1)}{\tau} = \partial_t P_1(s,t,1) + \dot{x}_c\partial_s P_1(s,t,1) + \frac{|\dot{n}_0|_+}{n_0}\big[P_1(s,t,1) - P_1(s,t,0)\big].$$

Considering the sub-ensemble of heads that are located at distance s, at time t and in the pool $\gamma=0$, we similarly establish that

$$\frac{\mathrm{d}P_1(s,t,0)}{\mathrm{d}t} = \partial_t P_1(s,t,0) + \dot{x}_c\partial_s P_1(s,t,0) + \frac{|\dot{n}_0|_-}{1-n_0}\big[P_1(s,t,0) - P_1(s,t,1)\big].$$

Finally, combining (4) and the total derivative expressions, we obtain the complete system of evolution equations

$$\begin{cases} \partial_t P_1(s,t,1) + \dot{x}_c\,\partial_s P_1(s,t,1) + \dfrac{|\dot{n}_0|_+}{n_0}\big[P_1(s,t,1) - P_1(s,t,0)\big] \\ \qquad\qquad = \big(k_{+,1}(s) + k^{\mathrm{rev}}_{-,1}(s)\big)P_0(s,t,1) - \big(k_{-,1}(s) + k^{\mathrm{rev}}_{+,1}(s)\big)P_1(s,t,1), \\ \partial_t P_1(s,t,0) + \dot{x}_c\,\partial_s P_1(s,t,0) + \dfrac{|\dot{n}_0|_-}{1-n_0}\big[P_1(s,t,0) - P_1(s,t,1)\big] \\ \qquad\qquad = \big(k_{+,0}(s) + k^{\mathrm{rev}}_{-,0}(s)\big)P_0(s,t,0) - \big(k_{-,0}(s) + k^{\mathrm{rev}}_{+,0}(s)\big)P_1(s,t,0), \\ P_0(s,t,\gamma) = 1 - P_1(s,t,\gamma). \end{cases} \tag{10}$$

We emphasize that, as in the original two-state model, the boundary conditions are chosen periodic for both pools, i.e. $P_1(s^-,t,\gamma) = P_1(s^+,t,\gamma)$. The property that no head should be attached on the boundaries of interval $[s^-,s^+]$ – which intrinsically comes with the assumption that the myosin heads can only attach to their nearest actin site – is ensured by the choice of appropriate transition rate parameter functions satisfying the conditions for all $\gamma \in \{0,1\}$ [Kimmig et al., 2019]

$$\left|\begin{array}{l} \lim\limits_{s\to s^-} k_{+,\gamma}(s) = \lim\limits_{s\to s^+} k_{+,\gamma}(s) = \lim\limits_{s\to s^-} k^{\mathrm{rev}}_{-,\gamma}(s) = \lim\limits_{s\to s^+} k^{\mathrm{rev}}_{-,\gamma}(s) = 0, \\ \lim\limits_{s\to s^-} \displaystyle\int_s^0 \big(k_{-,\gamma}(s) + k^{\mathrm{rev}}_{+,\gamma}(s)\big) = \lim\limits_{s\to s^+} \int_0^s \big(k_{-,\gamma}(s) + k^{\mathrm{rev}}_{+,\gamma}(s)\big) = +\infty. \end{array}\right. \tag{11}$$

The active force per myosin head developed by the system aggregates the contributions of the myosin heads in the two pools. It is given by

$$\tau_c(t) = \frac{1}{d_a}\int_{s^-}^{s^+} \big[n_0 P_1(s,t,1) + (1-n_0)P_1(s,t,0)\big]\partial_s w_1(s)\,\mathrm{d}s.$$

We point out that, in the framework presented here, we do not track the availability of the myosin heads individually, but we consider instead an average behavior for the population of myosin heads. Moreover, we assume that the heads switch pools randomly, i.e. all heads have the same probability to switch from one pool to another. A study of the common points and differences with models that do not consider this assumption is presented in Section 4.

2.3 Comparison with previous formulations

In this section, we compare our model with previous attempts of incorporating the thick filament activation mechanisms into the Huxley'57 model equation. Following the classical model presentation, we will write the two-state model equations with the aggregated transition rates, i.e.

$$\left|\begin{array}{l} f_\gamma(s) = k_{+,\gamma}(s) + k^{\mathrm{rev}}_{-,\gamma}(s), \\ g_\gamma(s) = k_{-,\gamma}(s) + k^{\mathrm{rev}}_{+,\gamma}(s). \end{array}\right.$$

As in our model, Peskin [1975], Zahalak & Motabarzadeh [1997] and Chapelle et al. [2012] consider that the fraction of myosin heads that are available for attachment is n_0. In the conservation of myosin heads, the flux of attachment is then assumed to be $f\big[n_0 - P_1\big]$ and the model dynamics is thus governed by the equation

$$\partial_t P_1(s,t) + \dot{x}_c \partial_s P_1(s,t) = f(s)\big[n_0(e_c) - P_1(s,t)\big] - g(s)P_1(s,t). \tag{12}$$

We can first note that the modeling assumption underlying the definition of the attachment flux is only valid if $n_0 - P_1$ represents the apparent activity of the myosin heads, i.e. $n_0 - P_1 \geq 0$. However, the latter property may not be ensured by the dynamics (12) possibly leading to the non-validity of the model in some phases of the simulated contraction.

We assume that the property $n_0 \geq P_1$ holds in the rest of this section. The probability of attachment P_1 is given by (2) in our proposed formulation using two pools of myosin heads. We differentiate P_1 with respect to time and obtain

$$\partial_t P_1(s,t) = \dot{n}_0\Big[P_1(s,t,1) - P_1(s,t,0)\Big] + n_0\partial_t P_1(s,t,1) + (1-n_0)\partial_t P_1(s,t,0).$$

Substituting the time derivatives from (10), we obtain

$$\begin{aligned}\partial_t P_1(s,t) + \dot{x}_c \partial_s P_1(s,t) = \dot{n}_0 \Big[P_1(s,t,1) - P_1(s,t,0)\Big] \\ + n_0 \Big(f_1(s)\big(1 - P_1(s,t,1)\big) - g_1(s) P_1(s,t,1) \\ - \frac{|\dot{n}_0|_+}{n_0}\big[P_1(s,t,1) - P_1(s,t,0)\big]\Big) \\ + (1-n_0)\Big(f_0(s)\big(1 - P_1(s,t,0)\big) - g_0(s) P_1(s,t,0) \\ - \frac{|\dot{n}_0|_-}{1-n_0}\big[P_1(s,t,0) - P_1(s,t,1)\big]\Big).\end{aligned} \tag{13}$$

Using the property (5), (13) becomes

$$\begin{aligned}\partial_t P_1(s,t) + \dot{x}_c \partial_s P_1(s,t) = n_0 \Big(f_1(s)\big(1 - P_1(s,t,1)\big) - g_1(s) P_1(s,t,1)\Big) \\ + (1-n_0)\Big(f_0(s)\big(1 - P_1(s,t,0)\big) - g_0(s) P_1(s,t,0)\Big).\end{aligned} \tag{14}$$

The spirit of our model is that the myosin heads belonging to the pool $\gamma = 0$ have a reduced probability of being attached, i.e. $P_1(s,t,0) \approx 0$. This property can be obtained with various choices of the transition rates, for instance with $f_1 = f$, $f_0 \ll f_1$ and $g_1 = g_0 = g$ or with $f_1 = f_0 = f$ and $g_1 = g \ll g_0$.

With the approximation $P_1(s,t,0) \approx 0$, we have $P_1(s,t) \approx n_0 P_1(s,t,1)$. Equation (14) yields

$$\partial_t P_1(s,t) + \dot{x}_c \partial_s P_1(s,t) \approx f(s)\big(n_0 - P_1(s,t)\big) + g(s) P_1(s,t),$$

and we retrieve the original modified Huxley equation (12).

The previously proposed formulations are thus enclosed in our model and are equivalent in the limit when $P_1(s,t,0)$ goes to zero. Our approach provides a more rigorous modeling framework having all apparent activities of the myosin heads considered in the flux of matter unconditionally positive. Moreover, as we will see in the next section, it is thermodynamically consistent, whereas previously proposed formulations do not satisfy the second principle because they break the detailed balance. The non-satisfaction of the second principle can also be qualitatively interpreted. Decreasing n_0 from the value 1 puts a fraction of myosin heads in a state where they are not allowed to attach and they are constrained in a single state: the detached state. Putting the heads in this situation increases the level of information on the system and is thus associated with a negative entropy creation, which is in contradiction with the second principle.

3 Thermodynamics

We want to derive, from the proposed evolution equations, the first and second thermodynamic balances for our system, which will show the consistency of the newly introduced modeling ingredients. To that purpose, we extend, for equations containing the pool exchange term, the approach proposed by Hill [1977] for the original family of Huxley'57 models.

We recall here a property that is fundamental in our analysis: the choice of transitions rates (11) ensures that

$$P_1(s = s^-, t, \gamma) = P_1(s = s^+, t, \gamma) = 0, t \geq 0, \ \gamma \in \{0,1\}.$$

For all results presented in this section, the detailed calculations can be found in Appendix A.1.

3.1 First principle

To establish the thermodynamic balances, we consider a population of myosin heads. The average energy per myosin head is defined by

$$\begin{aligned}\mathcal{U}(t) &= \frac{1}{d_a}\int_{s^-}^{s^+}\Big[w_1(s)P_1(s,t) + w_0P_0(s,t)\Big]\,\mathrm{d}s,\\ &= \frac{1}{d_a}\int_{s^-}^{s^+}\Big[w_1(s)\Big(n_0(t)P_1(s,t,1) + \big(1-n_0(t)\big)P_1(s,t,0)\Big)\\ &\qquad + w_0\Big(n_0(t)P_0(s,t,1) + \big(1-n_0(t)\big)P_0(s,t,0)\Big)\Big]\,\mathrm{d}s. \end{aligned} \tag{15}$$

We differentiate with respect to time, using the calculations made in [Hill, 1977] and [Kimmig et al., 2019] for the treatment of the chemical reaction and the transport terms and noting that the contributions arising from the pool exchange term cancel out with the property (5). Defining

$$\left|\begin{aligned} J_+(s,t,\gamma) &= k_{+,\gamma}(s)P_0(s,t,\gamma) - k^{\mathrm{rev}}_{+,\gamma}(s)P_1(s,t,\gamma),\\ J_-(s,t,\gamma) &= k_{-,\gamma}(s)P_1(s,t,\gamma) - k^{\mathrm{rev}}_{-,\gamma}(s)P_0(s,t,\gamma),\\ \overline{J}_-(t) &= \frac{1}{d_a}\int_{s^-}^{s^+}\Big[n_0(t)J_-(s,t,1) + \big(1-n_0(t)\big)J_-(s,t,0)\Big]\,\mathrm{d}s, \end{aligned}\right.$$

namely, J_+ the net flux of the attachment reaction, J_- the the net flux of the detachment reaction and $\overline{J}_-$ the average net flux of ATP consumption we finally have

$$\dot{\mathcal{U}}(t) = \dot{\mathcal{W}}(t) + \dot{\mathcal{E}}(t) + \dot{\mathcal{Q}}(t), \tag{16}$$

with

$$\left|\begin{aligned} \dot{\mathcal{W}}(t) &= \dot{x}_c\tau_c(t),\\ \dot{\mathcal{E}}(t) &= \mu_T\overline{J}_-(t),\\ \dot{\mathcal{Q}}(t) &= \frac{1}{d_a}\int_{s^-}^{s^+}\Bigg(n_0\Big[(w_1(s)-w_0)J_+(s,t,1) + (w_0-(w_1(s)+\mu_T))J_-(s,t,1)\Big]\\ &\qquad + (1-n_0)\Big[(w_1(s)-w_0)J_+(s,t,0)\\ &\qquad\qquad + (w_0-(w_1(s)+\mu_T))J_-(s,t,0)\Big]\Bigg)\,\mathrm{d}s. \end{aligned}\right.$$

The variation rate of energy is thus separated into different contributions: a mechanical power $\dot{\mathcal{W}}$, a flux of chemical energy brought by ATP $\dot{\mathcal{E}}$ and a thermal transfer flux $\dot{\mathcal{Q}}$. Note that all the terms are counted positive when the flux of energy is entering the system. As expected, the pool exchange terms do not contribute in the energy balance since the state energy levels are the same in both pools.

3.2 Second principle

The average entropy per myosin head is defined as the weighted average between the entropy in each pool. It is given by

$$\begin{aligned}\mathcal{S}(t) = -\frac{k_B}{d_a}\int_{s^-}^{s^+}\Bigg(&n_0\Big[P_1(s,t,1)\ln P_1(s,t,1) + P_0(s,t,1)\ln P_0(s,t,1)\Big]\\ &+ (1-n_0)\Big[P_1(s,t,0)\ln P_1(s,t,0) + P_0(s,t,0)\ln P_0(s,t,0)\Big]\Bigg)\,\mathrm{d}s. \end{aligned}$$

Our system is maintained at constant temperature by the environment, it can thus be more easily described by the adapted thermodynamics potential: the Helmholtz free energy. It is given by

$$\mathcal{F}(t) = \mathcal{U}(t) - T\mathcal{S}(t),$$

We thus formally have

$$\frac{\mathrm{d}}{\mathrm{d}t}\mathcal{F}(t) = \frac{\mathrm{d}}{\mathrm{d}t}\mathcal{U}(t) - T\frac{\mathrm{d}}{\mathrm{d}t}\mathcal{S}(t). \tag{18}$$

The free energy can also be expressed in terms of the chemical potentials

$$\begin{cases} \mu_1(s,t,\gamma) = w_1(s) + k_B T \ln[P_1(s,t,\gamma)], \ \gamma \in \{0,1\} \\ \mu_0(s,t,\gamma) = w_0 + k_B T \ln[P_0(s,t,\gamma)], \ \gamma \in \{0,1\}. \end{cases}$$

as

$$\begin{aligned} \mathcal{F}(t) = \frac{1}{d_a}\int_{s^-}^{s^+} \Big(& n_0 \Big[P_1(s,t,1)\mu_1(s,t,1) + P_0(s,t,1)\mu_0(s,t,1) \Big] \\ & + (1-n_0)\Big[P_1(s,t,0)\mu_1(s,t,0) + P_0(s,t,0)\mu_0(s,t,0) \Big] \Big)\, \mathrm{d}s. \end{aligned} \tag{19}$$

Differentiating with respect to time, using the calculations performed in [Hill, 1977] and [Kimmig et al., 2019], and using the property (5), we obtain

$$\begin{aligned} \frac{\mathrm{d}}{\mathrm{d}t}\mathcal{F}(t) = {} & \dot{\mathcal{W}}(t) + \dot{\mathcal{E}}(t) \\ & + \frac{1}{d_a}\int_{s^-}^{s^+} \Big(n_0 \Big[J_-(s,t,1)\big[\mu_0(s,t,1) - \big(\mu_1(s,t,1) + \mu_T\big)\big] \\ & \qquad + J_+(s,t,1)\big[\mu_1(s,t,1) - \mu_0(s,t,1)\big] \Big] \\ & \quad + (1-n_0)\Big[J_-(s,t,0)\big[\mu_0(s,t,0) - \big(\mu_1(s,t,0) + \mu_T\big)\big] \\ & \qquad + J_+(s,t,0)\big[\mu_1(s,t,0) - \mu_0(s,t,0)\big] \Big] \Big)\, \mathrm{d}s \\ & - \frac{k_B T}{d_a}\int_{s^-}^{s^+} \Big[|\dot{n}_0|_+ \Big[\ln\left(\frac{P_1(s,t,0)}{P_1(s,t,1)}\right) P_1(s,t,0) \\ & \qquad + \ln\left(\frac{1-P_1(s,t,0)}{1-P_1(s,t,1)}\right)\big(1-P_1(s,t,0)\big) \Big] \\ & \quad + |\dot{n}_0|_- \Big[\ln\left(\frac{P_1(s,t,1)}{P_1(s,t,0)}\right) P_1(s,t,1) \\ & \qquad + \ln\left(\frac{1-P_1(s,t,1)}{1-P_1(s,t,0)}\right)\big(1-P_1(s,t,1)\big) \Big] \Big]\, \mathrm{d}s. \end{aligned} \tag{20}$$

Combining (20) with (18) and the first principle (16), we obtain the second principle

$$\frac{\mathrm{d}}{\mathrm{d}t}\mathcal{S}(t) = \frac{\dot{\mathcal{Q}}}{T} + \dot{\mathcal{S}}_{\mathrm{prod}}(t),$$

defining the rate of entropy production as

$$\begin{aligned}\dot{\mathcal{S}}_{\mathrm{prod}}(t) = -\frac{1}{T}\frac{1}{d_a}\int_{s^-}^{s^+}\Big(&n_0\Big[J_-(s,t,1)\big[\mu_0(s,t,1)-\big(\mu_1(s,t,1)+\mu_T\big)\big]\\ &\qquad + J_+(s,t,1)\big[\mu_1(s,t,1)-\mu_0(s,t,1)\big]\Big]\\ &+(1-n_0)\Big[J_-(s,t,0)\big[\mu_0(s,t,0)-\big(\mu_1(s,t,0)+\mu_T\big)\big]\\ &\qquad + J_+(s,t,0)\big[\mu_1(s,t,0)-\mu_0(s,t,0)\big]\Big]\Big)\,\mathrm{d}s\\ +\frac{k_B}{d_a}\int_{s^-}^{s^+}\Big[&|\dot{n}_0|_+\Big[\ln\left(\frac{P_1(s,t,0)}{P_1(s,t,1)}\right)P_1(s,t,0)+\ln\left(\frac{1-P_1(s,t,0)}{1-P_1(s,t,1)}\right)\big(1-P_1(s,t,0)\big)\Big]\\ &+|\dot{n}_0|_-\Big[\ln\left(\frac{P_1(s,t,1)}{P_1(s,t,0)}\right)P_1(s,t,1)+\ln\left(\frac{1-P_1(s,t,1)}{1-P_1(s,t,0)}\right)\big(1-P_1(s,t,1)\big)\Big]\Big]\,\mathrm{d}s.\end{aligned}$$

The second principle is thus satisfied if the above defined entropy production rate is always positive.

The establishment of the second principle requires convexity inequalities that we present first. For all $(x,y)\in]0,1[^2$, we have the classical convexity inequality

$$\ln y - \ln x \geq \frac{1}{y}\big[y-x\big], \tag{21a}$$

$$\ln(1-y)-\ln(1-x)\geq \frac{1}{1-y}\big[x-y\big]. \tag{21b}$$

Multiplying (21a) by y, (21b) by $1-y$, and summing, we obtain

$$y\ln\left(\frac{y}{x}\right)+(1-y)\ln\left(\frac{1-y}{1-x}\right)\geq 0 \tag{22}$$

or equivalently

$$y\ln\left(\frac{x}{y}\right)+(1-y)\ln\left(\frac{1-x}{1-y}\right)\leq 0. \tag{23}$$

As was shown in [Hill, 1977], the integrand of the first integral term of $\dot{\mathcal{S}}_{\mathrm{prod}}$ is always positive if the transition rates satisfy the detailed balance (3). Indeed, we have

$$\begin{aligned}\frac{k_{+,\gamma}(s)P_0(s,t,\gamma)}{k^{\mathrm{rev}}_{+,\gamma}(s)P_1(s,t,\gamma)} &= \exp\Big(\frac{w_0-w_1(s)}{k_BT}\Big)\exp\Big(k_BT\frac{\ln\big[P_0(s,t,\gamma)-P_1(s,t,\gamma)\big]}{k_BT}\Big)\\ &= \exp\Big(\frac{\mu_0(s,t,\gamma)-\big(\mu_1(s,t,\gamma)+\mu_T\big)}{k_BT}\Big).\end{aligned} \tag{24}$$

Since we have $J_-(s,t,\gamma)=k_{-,\gamma}(s)P_1(s,t,\gamma)-k^{\mathrm{rev}}_{-,\gamma}(s)P_0(s,t,\gamma)$, we conclude from (24) that J_- and $\mu_0(s,t,1)-\big(\mu_1(s,t,1)+\mu_T\big)$ are of opposite sign. Therefore, the product of these two factors is negative and contribute positively to the entropy production with the minus sign in front of the integral. Similarly, the product of J_+ and $\mu_1(s,t,1)-\mu_0(s,t,1)$ is also always negative and contributes positively to the entropy production. Moreover, using the convexity inequality (22), we deduce that the second integral term of $\dot{\mathcal{S}}_{\mathrm{prod}}$ is always positive. As a consequence, we have $\dot{\mathcal{S}}_{\mathrm{prod}}\geq 0$ and the model is compatible with the second principle.

One can note that the entropy creation is composed of two contributions. The first one involves the attachment and detachment fluxes and corresponds to the chemical creation of entropy. The second one is an entropy creation term induced by the averaging process introduced in our model by the pool exchange terms. Indeed, at each time, we mix the probability of being attached (resp. detached) of the heads switching from one pool to another and the heads remaining in their initial pool. There is a loss of information on the system and thus a creation of entropy. An illustration of this phenomenon is presented in Section 4.1.

4 Range of validity and limitations

In this section, we investigate the behavior of our newly proposed model and in particular of the consequences of the homogenized myosin heads description in the pools instead of an individual description. To do so, we first numerically investigate the behavior of the pool exchange term in our equations. Then, to put our model in perspective, we compare our formulation with two ways of treating the myosin heads individually. Finally, we numerically compare our newly proposed formulation with the integration of the thick filament activation into the Huxley'57 model equations previously proposed in [Zahalak & Motabarzadeh, 1997; Chapelle et al., 2012].

To place the focus on the variations of the myosin head availability, we assume that the filaments do not slide along each other ($\dot{x}_c = 0$). In these conditions, the distance to the nearest actin site s is a parameter. We consider the representative subset of the myosin heads population that is located at distance s to its nearest actin site (for a value of s for which $P_1(s)$ is non-zero in isometric conditions) and the reference to the parameter s will be omitted in the rest of this section. Note that, for the sake of compactness, we will use the aggregated transition rates f_γ and g_γ in this section.

4.1 Impact of the homogenized description in the pool model

We first want to isolate the effect of the pool exchange operator, We thus assume that the attachment-detachment dynamics is prevented ($k_{+,\gamma} = k_{-,\gamma} = 0,\ \alpha \in \{0,1\},\ \gamma \in \{0,1\}$).

The only effect at play is a transfer between the two pools when n_0 varies. We will assume here that n_0 has an explicit dependency on time. We choose that, in the initial situation, $P_1(t = 0, 1) = 0.9$ and $P_1(t = 0, 0) = 0.1$.

We prescribe a periodic oscillatory evolution for n_0 (see Figure 2), i.e. in each period, we alternatively transfer heads from one pool to the other. The simulation results are presented in Figure 2.

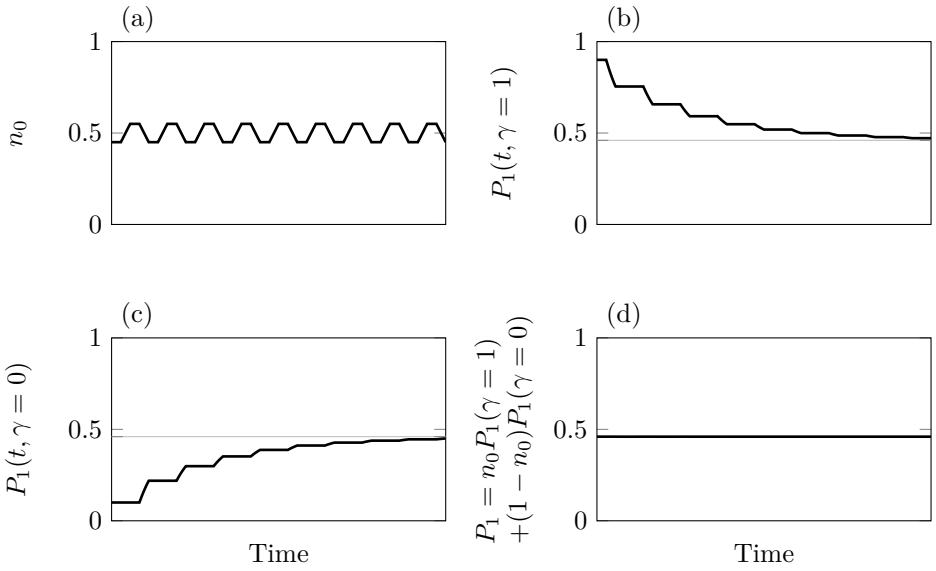

Figure 2: Illustration of the homogenization effect of the pool model. We consider here that the sliding velocity $\dot{x}_c$ vanishes and the attachment-detachment dynamics is blocked $k_{+,\gamma} = k_{-,\gamma} = 0$. (a) Prescribed evolution for n_0. (b), (c) & (d) Model outputs.

When n_0 increases, heads are transferred from the pool $\gamma = 0$ to the pool $\gamma = 1$. Since $P_1(t, 0) \leq P_1(t, 1)$, the heads arriving in the pool $\gamma = 1$ have a lower probability of being attached than the myosin heads already present in this pool. As a result the average probability of being attached in the pool $\gamma = 1$ decreases. Heads remaining in the pool $\gamma = 0$ are not mixed with any transferring myosin heads. Their probability of being attached $P_1(t, 0)$ is left unchanged. When n_0 decreases, the opposite effect takes place. Heads are transferred from the pool $\gamma = 1$ to the pool $\gamma = 0$ and

$P_1(t,0)$ increases. Since the attachment-detachment dynamics is prevented, the total probability of being attached $P_1(t) = n_0(t)P_1(t,1) + \big(1-n_0(t)\big)P_1(t,0)$ remains constant.

Repeating this process, the probability of being attached in each pool converges to the total probability of being attached $P_1(t)$. The exchanges between the pools tend to homogenize the probability of being attached between the two pools. This mixing effect is associated with a loss of information that is revealed in the entropy balance (see Section 3.2).

4.2 Comparison with individual description of the myosin heads

Our formulation (10) proposes a homogenized description of the myosin heads within the pools. To assess the impact of this assumption, we compare this homogenized formulation with stochastic individual descriptions of the myosin heads when the myosin heads availability varies. The heads are still separated into two pools, which defines their attachment-detachment dynamics, but their probability of being attached is tracked individually.

This comparison is not only an opportunity to put our modeling assumptions into perspective but also a way to determine if the distinction between different potential underlying mechanisms for the transition from one pool to the other matters in physiological conditions.

4.2.1 Heads switching pool chosen randomly

We first assume that the heads switching from one pool to the other are randomly chosen (i.e. all heads in the pool have the same probability to switch pools). The heads in the sarcomere therefore do not interact with each other. Any myosin head in the considered subset can attach and detach (the internal variable α is equal to one when the myosin head is attached, and to zero if it is detached) and switch between the pool of available heads ($\gamma = 1$) and the pool of non-available myosin heads ($\gamma = 0$). Its state at time t is described by (α^t, γ^t).

In order for this new model to be comparable with our homogenized formulation, we want the scaled number of heads in the pool $\gamma = 1$ to be controlled and equal to $n_0(t)$. In this stochastic model, this translates into the expected property $\mathbb{P}\big[\gamma^t = 1\big] = n_0(t)$ and $\mathbb{P}\big[\gamma^t = 0\big] = 1 - n_0(t)$.

Let us assume that this property holds and examine the resulting requirements on transition probabilities for the variable γ^t. Considering a small time interval τ, we would have

$$\mathbb{P}\big[\gamma^{t+\tau} = 1 | \gamma^t = 0\big] = \frac{\mathbb{P}\big[\gamma^{t+\tau} = 1, \gamma^t = 0\big]}{\mathbb{P}\big[\gamma^t = 0\big]} = \frac{|\dot{n}_0(t)|_+}{1-n_0(t)}\tau + o(\tau).$$

Similarly, we would also obtain

$$\mathbb{P}\big[\gamma^{t+\tau} = 0 | \gamma^t = 1\big] = \frac{\mathbb{P}\big[\gamma^{t+\tau} = 0, \gamma^t = 1\big]}{\mathbb{P}\big[\gamma^t = 0\big]} = \frac{|\dot{n}_0(t)|_-}{n_0(t)}\tau + o(\tau).$$

We now choose these transition probabilities for the variable γ. They imply that that the property $\mathbb{P}\big[\gamma^t = 1\big] = n_0(t)$ holds and we prescribe the initial condition $\mathbb{P}\big[\gamma^0 = 1\big] = n_0(0)$.

The complete system of probability transitions for the state of the myosin head is given by

$$\left|\begin{aligned}
&\mathbb{P}\big[\alpha^{t+\tau} = 1, \gamma^{t+\tau} = 1 | \alpha^t = 0, \gamma^t = 1\big] = f_1\,\tau + o(\tau),\\
&\mathbb{P}\big[\alpha^{t+\tau} = 0, \gamma^{t+\tau} = 1 | \alpha^t = 1, \gamma^t = 1\big] = g_1\,\tau + o(\tau),\\
&\mathbb{P}\big[\alpha^{t+\tau} = 1, \gamma^{t+\tau} = 0 | \alpha^t = 0, \gamma^t = 0\big] = f_0\,\tau + o(\tau),\\
&\mathbb{P}\big[\alpha^{t+\tau} = 0, \gamma^{t+\tau} = 0 | \alpha^t = 1, \gamma^t = 0\big] = g_0\,\tau + o(\tau),\\
&\mathbb{P}\big[\alpha^{t+\tau} = 1, \gamma^{t+\tau} = 1 | \alpha^t = 1, \gamma^t = 0\big] = \frac{|\dot{n}_0(t)|_+}{1-n_0(t)}\,\tau + o(\tau),\\
&\mathbb{P}\big[\alpha^{t+\tau} = 0, \gamma^{t+\tau} = 1 | \alpha^t = 0, \gamma^t = 0\big] = \frac{|\dot{n}_0(t)|_+}{1-n_0(t)}\,\tau + o(\tau),\\
&\mathbb{P}\big[\alpha^{t+\tau} = 1, \gamma^{t+\tau} = 0 | \alpha^t = 1, \gamma^t = 1\big] = \frac{|\dot{n}_0(t)|_-}{n_0(t)}\,\tau + o(\tau),\\
&\mathbb{P}\big[\alpha^{t+\tau} = 0, \gamma^{t+\tau} = 0 | \alpha^t = 0, \gamma^t = 1\big] = \frac{|\dot{n}_0(t)|_-}{n_0(t)}\,\tau + o(\tau).
\end{aligned}\right. \tag{25}$$

The various states in which a myosin heads can be, and the transitions between them, are summarized in Figure 3.

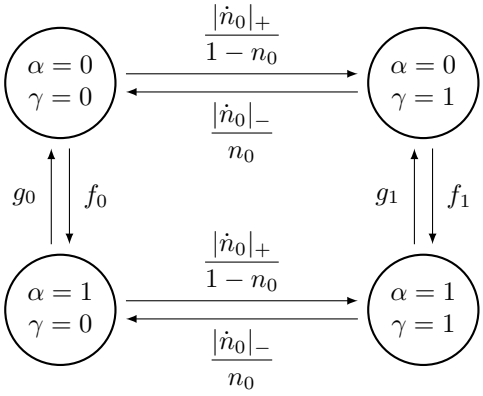

Figure 3: Diagram representation of the stochastic model tracking the myosin heads individually in the pools and using the random exchange paradigm.

We now want to analytically compare this model and the homogenized pool model. For this, we establish the Kolmogorov-forward-like equations associated with the system (25) [Le Bris & Lelievre, 2009] (the detailed calculations are presented in Appendix A.5). They take the form of the partial differential equations

$$\begin{cases} \partial_t P_1(t,1) = -\dfrac{|\dot{n}_0(t)|_+}{n_0(t)}\Big[P_1(t,1) - P_1(t,0)\Big] - g_1 P_1(t,1) + f_1 P_0(1), \\ \partial_t P_1(t,0) = -\dfrac{|\dot{n}_0(t)|_-}{1-n_0(t)}\Big[P_1(t,0) - P_1(t,1)\Big] - g_0 P_1(t,0) + f_0 P_0(t,0), \\ P_0(t,1) = 1 - P_1(t,1), \\ P_0(t,0) = 1 - P_1(t,0), \end{cases} \tag{26}$$

which are identical to (10) in the conditions considered (no filament sliding). The random exchange stochastic model and the homogenized pool model are thus equivalent.

4.2.2 Last-in first-out

It is also possible to consider that the heads are switching from one pool to the other in a last-in first-out manner. This would be a natural mechanism if an overlap effect is at the origin of the variations of myosin heads availability. In this case, the heads are, in some ways, interacting with each other through the memory of the transition order.

We assume that the subset of myosin heads considered contains N elements indexed by i of state (α_i^t, γ_i^t). They are shared in the two pools in the following manner

$$\gamma_i^t = \begin{cases} 1, & \text{if } i \leq \lfloor N n_0(t) \rfloor \\ 0, & \text{otherwise,} \end{cases}$$

where $\lfloor \bullet \rfloor$ denotes the floor function. Then, in each pool, we have the dynamics

$$\begin{cases} \mathbb{P}\big[\alpha_i^{t+\tau} = 1 | \alpha_i^t = 0, \gamma_i^t = 1\big] = f_1\,\tau + o(\tau), \\ \mathbb{P}\big[\alpha_i^{t+\tau} = 0 | \alpha_i^t = 1, \gamma_i^t = 1\big] = g_1\,\tau + o(\tau), \\ \mathbb{P}\big[\alpha_i^{t+\tau} = 1 | \alpha_i^t = 0, \gamma_i^t = 0\big] = f_0\,\tau + o(\tau), \\ \mathbb{P}\big[\alpha_i^{t+\tau} = 0 | \alpha_i^t = 1, \gamma_i^t = 0\big] = g_0\,\tau + o(\tau). \end{cases} \tag{27}$$

We do not attempt here to derive a counterpart to (26) for this model. We will simulate numerically the system of equations (27) to compare the last-in first-out model with other modeling strategies.

4.2.3 Numerical simulation

We have formally proven the equivalence between the homogenized description of the myosin heads availability and the individual description with a random pool exchange paradigm (see Section 4.2.1). In this section, we will additionally numerically compare the homogenized pool description with the individual description of the myosin head availability using the last-in first-out exchange paradigm.

To simulate stochastically the latter model with an individual description of the myosin heads, we consider N myosin heads. In the simulation results, we approximate the probabilities $\mathbb{P}_t\left[\overline{\alpha}, \overline{\gamma}\right] = \mathbb{P}\left[\alpha^t = \overline{\alpha}, \gamma^t = \overline{\gamma}\right]$ with the empirical probabilities

$$\overline{\mathbb{P}}_t\left[\overline{\alpha}, \overline{\gamma}\right] = \frac{1}{N}\sum_{i=1}^{N} \mathbb{1}_{\{\alpha^t=\overline{\alpha}, \gamma^t=\overline{\gamma}\}}(\alpha_i^t, \gamma_i^t).$$

We prescribe the time evolution of n_0 with variations that reproduce that of a heartbeat with physiological time scales. Starting from a steady-state where n_0 is constant with a value of 0.80 – heads are mainly available for attachment – the scaled number of available myosin heads is decreased to the value 0.20 – heads are mainly unavailable for attachment – in 0.1 s corresponding to the systole. This phase is then followed by a plateau in which n_0 is maintained constant for 0.2 s. The thick filament activation n_0 is then brought back to its original value in 0.1 s. This corresponds to the diastole.

For a physiological simulation, we also need to select meaningful values for the transition rates. The physiological values of the attachment f and detachment g rates for cardiac muscle remain subject to debate [Månsson, 2010; Kimmig & Caruel, 2019]. Indeed, classically, muscle contraction models – deriving from Huxley'57 model – cannot reproduce at the sarcomere level both the force-velocity relation and the tension rise dynamics, showing that this description of the cycling process actually encompasses other molecular mechanisms whose dynamics is aggregated to the attachment and detachment rates. Depending on which physiological indicators is privileged for the model calibration, different values of the transition rates are obtained with a factor six difference. In this section, we will test both options.

On the one hand, we have the transition rates proposed by [Kimmig et al., 2019] when favoring the force-velocity curve. The attachment rate is $f_1 = \overline{f}_1 = 250\,\mathrm{s}^{-1}$ and the detachment rate is $g_1 = \overline{g}_1 = 60\,\mathrm{s}^{-1}$. To take into account that heads in the pool $\gamma = 0$ attach with a lower probability, we use $\overline{f}_0 = 0.01\overline{f}_1$ and $\overline{g}_0 = \overline{g}_1$. We call this choice of parameters the reference. On the other hand, if we focus on the tension rise dynamics, we typically have $f_1 = \overline{f}_1/6 = 41.6\,\mathrm{s}^{-1}$ and the detachment rate is $g_1 = \overline{g}_1/6 = 10\,\mathrm{s}^{-1}$ (see for instance [de Tombe & Stienen, 2007]) and again we use the assumption $\overline{f}_0 = 0.01\overline{f}_1$ and $\overline{g}_0 = \overline{g}_1$. We additionally consider a non-physiological calibration for illustration purposes with $f_1 = \overline{f}_1/50 = 5\,\mathrm{s}^{-1}$ and $g_1 = \overline{g}_1/50 = 1.2\,\mathrm{s}^{-1}$ The simulation results for the two models considered and the three tested calibrations are presented in Figure 4.

We first comment on the evolution of the system with the two sets of physiological rates (Figure 4 left and middle columns). In the initial state, heads in both pools are attached with the steady-state probability $P_1(\gamma, t) = \overline{f}_\gamma/(\overline{f}_\gamma + \overline{g}_\gamma)$. During the systole, some heads switch from the pool $\gamma = 1$ to the pool $\gamma = 0$. Since the probability of being attached is higher in the pool $\gamma = 1$ than in the pool $\gamma = 0$, $P_1(\gamma = 0)$ increases. The probability of being attached in the pool $\gamma = 1$ remains unchanged. For both models, heads that change pools are equivalent, and therefore the way of choosing them does not matter and the evolution of $P_1(\gamma = 0)$ is the same for the two models. As soon as the heads stop being transferred into the other pool, the attachment-detachment dynamics leads to a return to the steady-state value of $P_1(\gamma = 0)$. Here, the time scale of the attachment-detachment dynamics is short compared to the duration of the plateau. At the end of the latter phase the heads thus have a probability of being attached in both pools that is almost equal to the steady-state probability. There is no memory of the "pool of origin". In the diastole, heads switch from the pool $\gamma = 0$ to the pool $\gamma = 1$. We have $P_1(\gamma = 1) > P_1(\gamma = 0)$, which implies that $P_1(\gamma = 1)$ decreases while $P_1(\gamma = 0)$ is almost constant. Since the state in the two models were the same at the end of the plateau, the evolution of $P_1(\gamma = 1)$ is the same for the two models.

The situation is different with the non-physiological transition rates (Figure 4 right column). The attachment-detachment dynamics time scale is not short compared to the plateau duration. Therefore, in the pool $\gamma = 0$ heads that swapped pools during the systole have a higher probability of being attached than the other heads of the pool. With the homogenized model, the probability $P_1(\gamma = 0)$ is not affected by the pool exchange in the diastole, since heads that leave the pool have the average probability of being

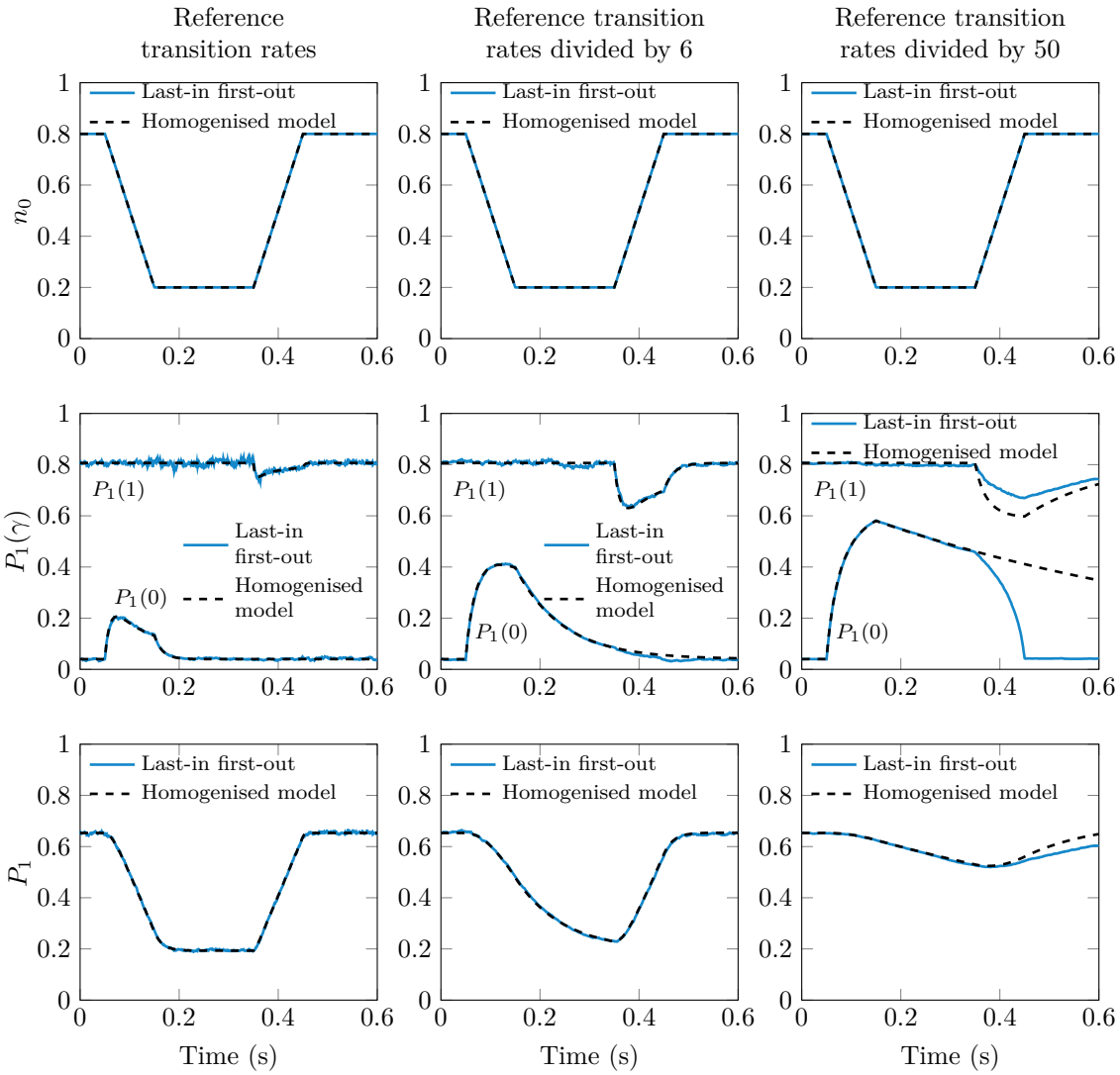

Figure 4: Model comparison between the homogenized treatment of the myosin heads changing pools, and individual tracking of those heads with the last-in first-out paradigm (quantities computed from 10000 stochastic trajectories). Note that the time scale of the transition between the pools is 0.15 s. The time scale of the attachment-detachment process is given by the duration of a cycle, i.e. $f^{-1} + g^{-1}$. Left column: simulation with reference transition rates targeting the force-velocity curve [Kimmig & Caruel, 2019]. The time scale of the attachment-detachment process is 0.02 s. Center column: reference transition rates divided by a factor six to mimic the calibration proposed by de Tombe & Stienen [2007] aiming at capturing the force rise dynamics. The time scale of the attachment-detachment process is 0.12 s. Right column: reference transition rates divided by a factor 50 to illustrate the competition between the attachment-detachment time scale and the pool exchange time scale in the model. The time scale of the attachment-detachment process is 1 s.

attached and it is governed solely by the attachment-detachment dynamics. With the last-in first-out paradigm, the heads that switch from the pool $\gamma = 0$ to the pool $\gamma = 1$ are exactly those that were in the pool $\gamma = 1$ at the beginning of the simulation and they are precisely the heads that have a higher probability of being attached. As a result, the probabilities $P_1(\gamma = 1)$ and $P_1(\gamma = 0)$ retrieve their initial level – up to attachment-detachment transitions that have occurred in the plateau. In this configuration, the last-in first-out paradigm and the homogenized pool model provide different outputs that affect the total probability of being attached P_1, which will yield variations of the ultimate quantity of interest: the active force.

In a nutshell, the last-in first-out pool exchange paradigm differs from the homogenized model (or equivalently the random pool exchange paradigm) when the dynamics of the exchanges between the pools is fast or of similar rate compared to the attachment-detachment dynamics. The two paradigms are equivalent otherwise. It is *a priori* not possible to know which exchange paradigm – random, last-in first-out, or another paradigm – is at play at the microscopic level. However, this does not harm our modeling approach because the two formulations are equivalent when physiological values of the transition rates and physiological variation time scales of the parameter function n_0 are considered. Therefore, our homogenized formulation is fully valid in the context of cardiac muscle modeling, regardless of the uncertainty on the physiological transition rates.

In another situation where the difference between both paradigms may matter, additional experimental data should be sought. It would require structural experimental measurements that are capable of distinguishing the behavior of neighboring heads in a dynamical manner. To the best of our knowledge, state-of-the-art structural measurements for cardiac muscle cells can only deal with steady states and characterize the global behavior of the myosin heads population [Reconditi et al., 2017].

4.3 Comparison with previously proposed formulation to incorporate the thick filament regulation in the Huxley'57 models family

We now compare our formulation (10), aiming at a proper treatment of the myosin heads availability in the realm of the Huxley'57 contraction model family, with previous formulations (12) [Zahalak & Motabarzadeh, 1997; Chapelle et al., 2012].

We consider again a system where n_0 is prescribed and we use the same time evolution of this input function as that presented in Figure 4. The results are shown in Figure 5. We can note that the two formulations depart from each other when $P_1(\gamma = 0)$ becomes significant.

With the model proposed by [Chapelle et al., 2012], a fraction $1-n_0$ of myosin heads is not allowed to attach. In the new formulation, it is equivalent to assuming that $P_1(\gamma = 0) = 0$. When the attachment-detachment dynamics is fast compared to the pool dynamics, the myosin heads in the pool $\gamma = 0$ quickly detach and this assumption is approximately valid (see Figure 5(a)). The two formulations provide results that differ by about 10% during systole.

However, when the cycling time scale is large compared to the myosin availability variations, we may have $P_1(\gamma = 0)$ significantly different from 0. In this case, the two formulations largely differ (see Figure 5(b)).

5 Numerical methods

In this section, we present the numerical method designed to simulate the newly introduced model (10) and derive the discretized version of the thermodynamical balances that can be obtained at the microscopic and the macroscopic levels. To benefit from the separation of time scales between the microscopic contraction model ($\sim$10 ms) and the macroscopic heart model ($\sim$1 s), we propose a double time step discretization scheme. We denote by δt and Δt the microscopic and macroscopic time steps, respectively, with the convention that $N\delta t = \Delta t$ (with $N \in \mathbb{N}^*$). This double time step scheme allows to properly capture the physical mechanisms occurring at the microscopic level while avoiding unnecessary resolutions of the macroscopic equations.

5.1 Microscopic numerical scheme

We first present the numerical scheme for the microscopic dynamics.

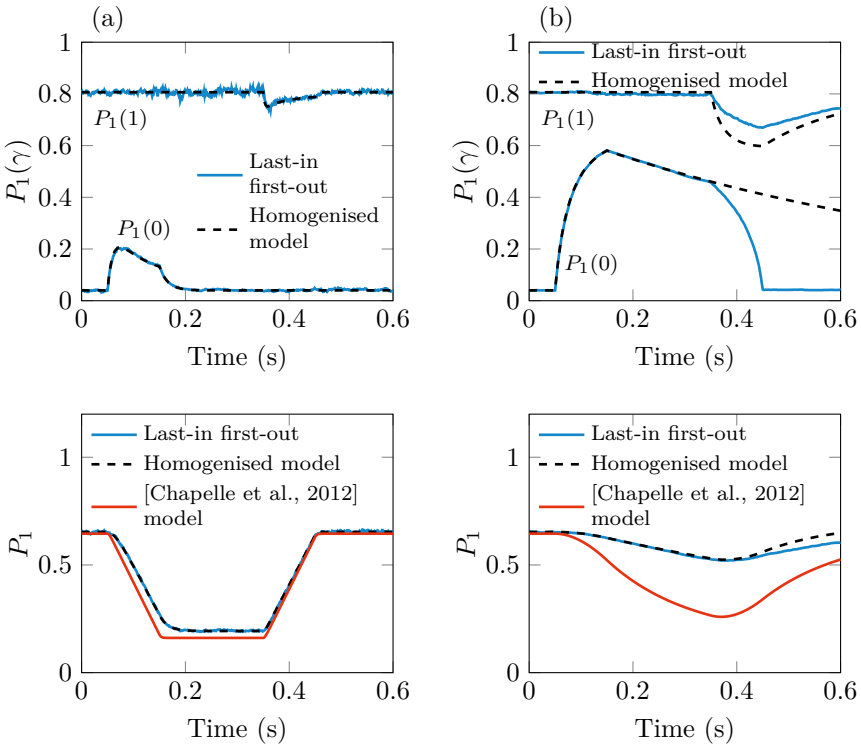

Figure 5: Comparison between the proposed thick filament activation description and that previously used by [Zahalak & Motabarzadeh, 1997; Chapelle et al., 2012]. (a) Transition rates given by [Kimmig & Caruel, 2019]. (b) Non-physiological transition rates 50 times slower than that of [Kimmig & Caruel, 2019].

The simulation range $[s^-, s^+]$ is discretized by a regular grid of discretization length δs and with the choice $s_0 = s^-$ and $s_\ell = s^+$. For the sake of compactness of the notation, we denote $P_1(s^- + i\delta s, n\Delta t + k\delta t, 1)$ by $a_i^{n,k}$ and $P_1(s^- + i\delta s, n\Delta t + k\delta t, 0)$ by $b_i^{n,k}$, $n \in \mathbb{N},\ k \in [\![0, N]\!]$.

For the chemical reaction term, we use an implicit scheme, and an upwind implicit scheme for the transport term as proposed by [Kimmig et al., 2019]. The pool exchanges terms are treated with a semi-explicit, semi-implicit scheme. The choice of such a scheme is justified by the fact that it allows to establish a discrete energy balance (see Section 5.1.2).

Note that the presentation will be restricted to positive sliding velocities $\dot{x}_c$ but the results can be straightforwardly extended to negative sliding velocities by reversing the space shift in the transport term so that the scheme keeps its upwind nature.

We denote the discrete sliding velocity by

$$v_c^{n+\frac{1}{2}\sharp} = \ell_{hs}(e_c^{n+1} - e_c^n)/\Delta t \tag{28}$$

and we assume that it is positive (i.e. $e_c^{n+1} - e_c^n \geq 0$). We define $n_0^n = n_0(e_c^n)$.

The discretization scheme then reads

$$\begin{cases} \dfrac{a_i^{n,k+1} - a_i^{n,k}}{\delta t} = -\dfrac{|n_0^{n+1} - n_0^n|_+}{n_0^{n,k+1}\Delta t}\left[a_i^{n,k} - b_i^{n,k}\right] + (k_{+,1,i} + k_{-,1,i}^{\mathrm{rev}})(1 - a_i^{n,k+1}) \\ \qquad\qquad - (k_{-,1,i} + k_{+,1,i}^{\mathrm{rev}})a_i^{n,k+1} - v_c^{n+\frac{1}{2}\sharp}\dfrac{a_i^{n,k+1} - a_{i-1}^{n,k+1}}{\delta s},\ i \in [\![1, \ell]\!] \\ \dfrac{b_i^{n,k+1} - b_i^{n,k}}{\delta t} = -\dfrac{|n_0^{n+1} - n_0^n|_-}{(1 - n_0^{n,k+1})\Delta t}\left[b_i^{n,k} - a_i^{n,k}\right] + (k_{+,0,i} + k_{-,0,i}^{\mathrm{rev}})(1 - b_i^{n,k+1}) \\ \qquad\qquad - (k_{-,0,i} + k_{+,0,i}^{\mathrm{rev}})b_i^{n,k+1} - v_c^{n+\frac{1}{2}\sharp}\dfrac{b_i^{n,k+1} - b_{i-1}^{n,k+1}}{\delta s},\ i \in [\![1, \ell]\!] \end{cases} \tag{29}$$

with the definitions

$$\begin{vmatrix} k_{+,1,i} = k_{+,1}(s^- + i\delta s) & \text{and} & k_{+,1,i}^{\mathrm{rev}} = k_{+,1}^{\mathrm{rev}}(s^- + i\delta s),\ i \in [\![1, \ell]\!] \\ k_{+,0,i} = k_{+,0}(s^- + i\delta s) & \text{and} & k_{+,0,i}^{\mathrm{rev}} = k_{+,0}^{\mathrm{rev}}(s^- + i\delta s),\ i \in [\![1, \ell]\!] \\ k_{-,1,i} = k_{-,1}(s^- + i\delta s) & \text{and} & k_{-,1,i}^{\mathrm{rev}} = k_{-,1}^{\mathrm{rev}}(s^- + i\delta s),\ i \in [\![1, \ell - 1]\!] \\ k_{-,0,i} = k_{-,0}(s^- + i\delta s) & \text{and} & k_{-,0,i}^{\mathrm{rev}} = k_{-,0}^{\mathrm{rev}}(s^- + i\delta s),\ i \in [\![1, \ell - 1]\!] \\ k_{-,1,\ell} = 200\, k_{-,1,\ell-1} & \text{and} & k_{+,1,\ell}^{\mathrm{rev}} = 200\, k_{+,1,\ell-1}^{\mathrm{rev}}, \\ k_{-,0,\ell} = 200\, k_{-,0,\ell-1} & \text{and} & k_{+,0,\ell}^{\mathrm{rev}} = 200\, k_{+,0,\ell-1}^{\mathrm{rev}}, \end{vmatrix}$$

and

$$n_0^{n,k} = n_0^n + k\frac{\delta t}{\Delta t}\left(n_0^{n+1} - n_0^n\right).$$

We define the aggregated attachment and detachment rate by $f_{\gamma,i} = k_{+,\gamma,i} + k_{-,\gamma,i}^{\mathrm{rev}}$ and $g_{\gamma,i} = k_{-,\gamma i} + k_{+,\gamma,i}^{\mathrm{rev}}$, respectively. Note that the numerical detachment rates differ from their analytical counterparts, which go to infinity on the boundaries of the interval $[s^-, s^+]$. Indeed, as proposed by Kimmig et al. [2019], we use instead a consistent finite approximation. The choice of the boundary conditions follows that of Kimmig et al. [2019] as well. We prescribe periodic boundary conditions for $a^{n,k}$ and $b^{n,k}$. We have $a_0^{n,k} = a_\ell^{n,k}$ and $b_0^{n,k} = b_\ell^{n,k}$. The initialization of the discretization is done such that $a_0^{0,0} = a_\ell^{0,0} = 0$ and $b_0^{0,0} = b_\ell^{0,0} = 0$. Moreover, we prescribe that $a_i^{0,0}$ and $b_i^{0,0} \in [0, 1], i \in [\![1, \ell]\!]$ to be consistent with the definition of $a_i^{0,0}$ and $b_i^{0,0}$ as probabilities.

Defining

$$\begin{vmatrix} \alpha^{n+\frac{1}{2}\sharp} = \ell_{hs}(e_c^{n+1} - e_c^n)/\Delta t \cdot \delta t/\delta s, \\ \beta_{1,i}^{n+\frac{1}{2}\sharp} = \delta t\left(k_{+,1,i} + k_{+,1,i}^{\mathrm{rev}} + k_{-,1,i} + k_{-,1,i}^{\mathrm{rev}}\right) + \alpha^{n+\frac{1}{2}\sharp}, \\ \beta_{0,i}^{n+\frac{1}{2}\sharp} = \delta t\left(k_{+,0,i} + k_{+,0,i}^{\mathrm{rev}} + k_{-,0,i} + k_{-,0,i}^{\mathrm{rev}}\right) + \alpha^{n+\frac{1}{2}\sharp}, \end{vmatrix}$$

the numerical scheme can be written in a vectorial form using the state vector

$$\mathbf{P}^{n,k} = \begin{bmatrix} a_1^{n,k} & \dots & a_\ell^{n,k} & b_1^{n,k} & \dots & b_\ell^{n,k} \end{bmatrix}^\mathsf{T}.$$

The system (29) becomes

$$(\mathbb{I}_d + \mathbb{I}^{n+\frac{1}{2}\sharp})\mathbf{P}^{n,k+1} = (\mathbb{I}_d - \mathbb{E}^{n,k+1})\mathbf{P}^{n,k} + \delta t \mathbf{f},$$

where $\mathbb{I}_d$ is the $2\ell \times 2\ell$ identity matrix

$$\mathbb{I}^{n+\frac{1}{2}\sharp} = \left[\begin{array}{cccc|cccc} \beta_{1,1}^{n+\frac{1}{2}\sharp} & & & -\alpha^{n+\frac{1}{2}\sharp} & & & & \\ -\alpha^{n+\frac{1}{2}\sharp} & \beta_{1,2}^{n+\frac{1}{2}\sharp} & & & & & & \\ & \ddots & \ddots & & & & & \\ & & -\alpha^{n+\frac{1}{2}\sharp} & \beta_{1,\ell}^{n+\frac{1}{2}\sharp} & & & & \\ \hline & & & & \beta_{0,1}^{n+\frac{1}{2}\sharp} & & & -\alpha^{n+\frac{1}{2}\sharp} \\ & & & & -\alpha^{n+\frac{1}{2}\sharp} & \beta_{0,2}^{n+\frac{1}{2}\sharp} & & \\ & & & & & \ddots & \ddots & \\ & & & & & & -\alpha^{n+\frac{1}{2}\sharp} & \beta_{0,\ell}^{n+\frac{1}{2}\sharp} \end{array}\right],$$

$$\mathbb{E}_1 = \left[\begin{array}{cccc|cccc} 1 & & & & -1 & & & \\ & 1 & & & & -1 & & \\ & & 1 & & & & -1 & \\ & & & 1 & & & & -1 \\ \hline & & & & & & & \\ & & & & & & & \\ & & & & & & & \\ & & & & & & & \end{array}\right], \quad \mathbb{E}_0 = \left[\begin{array}{cccc|cccc} & & & & & & & \\ & & & & & & & \\ & & & & & & & \\ & & & & & & & \\ \hline -1 & & & & 1 & & & \\ & -1 & & & & 1 & & \\ & & -1 & & & & 1 & \\ & & & -1 & & & & 1 \end{array}\right],$$

$$\mathbf{f} = \left[f_{1,1}, f_{1,2}, \ldots, f_{1,\ell}, f_{0,1}, f_{0,2}, \ldots, f_{0,\ell}\right]^{\mathsf{T}},$$

$$\text{and } \mathbb{E}^{n,k+1} = \frac{|n_0^{n+1} - n_0^n|_+}{n_0^{n,k+1}} \frac{\delta t}{\Delta t}\mathbb{E}_1 + \frac{|n_0^{n+1} - n_0^n|_-}{1 - n_0^{n,k+1}} \frac{\delta t}{\Delta t}\mathbb{E}_0.$$

5.1.1 Uniform positivity and boundeness

We want to ensure that, at all time steps and discretized positions of s in the interval $[s^-, s^+]$, the numerical solutions $a_i^{n,k}$ and $b_i^{n,k}$ satisfy the property

$$0 \le a_i^{n,k} \le 1 \quad \text{and} \quad 0 \le b_i^{n,k} \le 1 \quad \Longleftrightarrow \quad 0 \le \mathbf{P}^{n,k} \le 1,\ n \in \mathbb{N},\ k \in [\![0, N]\!],$$

where vector inequalities should be understood component by component. This property allows to keep the interpretation of $a_i^{n,k}$ and $b_i^{n,k}$ as probabilities, but it is also essential from a numerical point of view since the calculation of some thermodynamic quantities requires to evaluate the logarithm of the probabilities of being attached.

We proceed by induction and we assume that

$$0 \le \mathbf{P}^{n,k} \le 1. \tag{30}$$

We introduce the vector $\mathbf{1} - \mathbf{P}^{n,k}$. Its dynamics is governed by

$$(\mathbb{I}_d + \mathbb{I}^{n+\frac{1}{2}\sharp})(\mathbf{1} - \mathbf{P}^{n,k+1}) = (\mathbb{I}_d - \mathbb{E}^{n,k+1})(\mathbf{1} - \mathbf{P}^{n,k}) + \delta t \mathbf{g}.$$

We want to show that

$$\left|\begin{array}{l} 0 \le \mathbf{P}^{n,k+1}, \\ 0 \le \mathbf{1} - \mathbf{P}^{n,k+1}. \end{array}\right.$$

We know from [Kimmig et al., 2019], that the matrix $\mathbb{I}_d + \mathbb{I}^{n+\frac{1}{2}\sharp}$ preserves the positivity – ie. $\forall \mathbf{P} \in \mathbb{R}^{2\ell}$, $(\mathbb{I}_d + \mathbb{I}^{n+\frac{1}{2}\sharp})\mathbf{P} \geq 0 \Rightarrow \mathbf{P} \geq 0$. Therefore, the desired property $0 \leq \mathbf{P}^{n,k+1} \leq 1$ is obtained if

$$(\mathbb{I}_d - \mathbb{E}^{n,k+1})\mathbf{P}^{n,k} + \delta t \mathbf{f} \geq 0 \quad \text{and} \quad (\mathbb{I}_d - \mathbb{E}^{n,k+1})(\mathbf{1} - \mathbf{P}^{n,k}) + \delta t \mathbf{g} \geq 0.$$

A sufficient condition is given by

$$\left|\begin{aligned}
&0 \leq \Big(1 - \delta t \frac{|n_0^{n+1} - n_0^n|_+}{n_0^{n,k+1}\Delta t}\Big) a_i^{n,k} + \delta t \frac{|n_0^{n+1} - n_0^n|_+}{n_0^{n,k+1}\Delta t} b_i^{n,k} + \delta t f_{1,i} \\
&0 \leq \delta t \frac{|n_0^{n+1} - n_0^n|_+}{n_0^{n,k+1}\Delta t} a_i^{n,k} + \Big(1 - \delta t \frac{|n_0^{n+1} - n_0^n|_-}{(1 - n_0^{n,k+1})\Delta t}\Big) b_i^{n,k} + \delta t f_{0,i} \\
&0 \leq \Big(1 - \delta t \frac{|n_0^{n+1} - n_0^n|_+}{n_0^{n,k+1}\Delta t}\Big)(1 - a_i^{n,k}) + \delta t \frac{|n_0^{n+1} - n_0^n|_+}{n_0^{n,k+1}\Delta t}(1 - b_i^{n,k}) + \delta t g_{1,i} \\
&0 \leq \delta t \frac{|n_0^{n+1} - n_0^n|_+}{n_0^{n,k+1}\Delta t}(1 - a_i^{n,k}) + \Big(1 - \delta t \frac{|n_0^{n+1} - n_0^n|_-}{(1 - n_0^{n,k+1})\Delta t}\Big)(1 - b_i^{n,k}) + \delta t g_{0,i}.
\end{aligned}\right. \tag{31}$$

The induction hypothesis (30) gives $0 \leq a_i^{n,k} \leq 1$ and $0 \leq b_i^{n,k} \leq 1$. It is thus sufficient, in order to have the property (31), that δt satisfies the (non-optimal) CFL-like condition

$$\delta t \leq \min\Big(\frac{n_0^n}{|n_0^{n+1} - n_0^n|_+}\Delta t, \frac{1 - n_0^{n+1}}{|n_0^{n+1} - n_0^n|_-}\Delta t\Big). \tag{32}$$

In all numerical results presented in what follows, we will make sure that this condition is satisfied.

5.1.2 First principle

We now aim at establishing a discrete counterpart to the continuous first principle (16). We only present here the main results; their detailed proof is given in Section A.6.1. We discretize the attached state energy level on $[s^-, s^+]$ by

$$\left|\begin{aligned}
&w_{1,i} = w_1(s^- + i\delta s), \ i \in [\![1, \ell - 1]\!] \\
&w_{1,\ell} = 150\, w_{1,\ell-1}.
\end{aligned}\right.$$

We define the discrete average energy per myosin head by

$$\mathcal{U}^{n,k} = \frac{\delta s}{d_a} \sum_{i=1}^{\ell} \Big[w_{1,i}\big(n_0^{n,k} a_i^{n,k} + (1 - n_0^{n,k}) b_i^{n,k}\big) + w_0\big(n_0^{n,k}(1 - a_i^{n,k}) + (1 - n_0^{n,k})(1 - b_i^{n,k})\big)\Big].$$

Defining the attachment-detachment fluxes as

$$\left|\begin{aligned}
&J_{+,1,i}^{n,k} = k_{+,1,i} a_i^{n,k} - k_{+,1,i}^{\text{rev}}(1 - a_i^{n,k}), \\
&J_{+,0,i}^{n,k} = k_{+,0,i} b_i^{n,k} - k_{+,0,i}^{\text{rev}}(1 - b_i^{n,k}), \\
&J_{-,1,i}^{n,k} = k_{-,1,i}(1 - a_i^{n,k}) - k_{-,1,i}^{\text{rev}} a_i^{n,k}, \\
&J_{-,1,i}^{n,k} = k_{-,0,i}(1 - b_i^{n,k}) - k_{-,0,i}^{\text{rev}} b_i^{n,k},
\end{aligned}\right. \tag{33}$$

we obtain the first principle formulation at local time steps

$$\frac{\mathcal{U}^{n,k+1} - \mathcal{U}^{n,k}}{\delta t} = \frac{\mathcal{W}^{n,k+1} - \mathcal{W}^{n,k}}{\delta t} + \frac{\mathcal{Q}^{n,k+1} - \mathcal{Q}^{n,k}}{\delta t} + \frac{\mathcal{E}^{n,k+1} - \mathcal{E}^{n,k}}{\delta t}, \tag{34}$$

with

$$\left|\begin{aligned}
&\frac{\mathcal{W}^{n,k+1} - \mathcal{W}^{n,k}}{\delta t} = v_c^{n+\frac{1}{2}\sharp} \tau_c^{n,k+1}, \\
&\frac{\mathcal{Q}^{n,k+1} - \mathcal{Q}^{n,k}}{\delta t} = \frac{\delta s}{d_a} \sum_{i=1}^{\ell} \Big[\Big(n_0^{n,k+1} J_{+,1,i}^{n,k+1} + (1 - n_0^{n,k+1}) J_{+,0,i}^{n,k+1}\Big)(w_{1,i} - w_0) \\
&\qquad\qquad + \Big(n_0^{n,k+1} J_{-,1,i}^{n,k+1} + (1 - n_0^{n,k+1}) J_{-,0,i}^{n,k+1}\Big)\big(w_0 - (w_{1,i} + \mu_T)\big)\Big], \\
&\frac{\mathcal{E}^{n,k+1} - \mathcal{E}^{n,k}}{\delta t} = \mu_T \frac{\delta s}{d_a} \sum_{i=1}^{\ell} \Big(n_0^{n,k+1} J_{-,1,i}^{n,k+1} + (1 - n_0^{n,k+1}) J_{-,0,i}^{n,k+1}\Big),
\end{aligned}\right.$$

where the force per myosin head $\tau_c^{n,k+1}$ is defined by

$$\tau_c^{n,k+1} = \frac{\delta s}{d_a} \sum_{i=1}^{\ell} \frac{w_{1,i+1} - w_{1,i}}{\delta s} \Big(n_0^{n,k+1} a^{n,k+1} + (1 - n_0^{n,k+1}) b^{n,k+1} \Big).$$

5.1.3 Second principle

As for the first principle, we only present here the results; their detailed proof is given in Section A.6.2.

To derive a discrete version of the second principle, we first define the chemical potentials in each pool

$$\left| \begin{array}{l} \mu^{n,k}_{\alpha=1,\gamma=1,i} = \mu^{n,k}_{1,1,i} = w_{1,i} + k_B T \ln a_i^{n,k}, \\ \mu^{n,k}_{\alpha=1,\gamma=0,i} = \mu^{n,k}_{1,0,i} = w_{1,i} + k_B T \ln b_i^{n,k}, \\ \mu^{n,k}_{\alpha=0,\gamma=1,i} = \mu^{n,k}_{0,1,i} = w_0 + k_B T \ln(1 - a_i^{n,k}), \\ \mu^{n,k}_{\alpha=0,\gamma=0,i} = \mu^{n,k}_{0,0,i} = w_0 + k_B T \ln(1 - b_i^{n,k}). \end{array} \right.$$

We define the entropy per myosin head as

$$\mathcal{S}^{n,k} = -k_B \frac{\delta s}{d_a} \sum_{i=1}^{\ell} \Big[n_0^{n,k} \Big(a_i^{n,k} \ln a_i^{n,k} + (1 - a_i^{n,k}) \ln(1 - a_i^{n,k}) \Big) + (1 - n_0^{n,k}) \Big(b_i^{n,k} \ln b_i^{n,k} + (1 - b_i^{n,k}) \ln(1 - b_i^{n,k}) \Big) \Big].$$

Note that the entropy is well-defined for $a^{n,k} \in [0,1]$ and $b^{n,k} \in [0,1]$.

Using the numerical scheme (29), we obtain the second principle inequality

$$\frac{\mathcal{S}^{n,k+1} - \mathcal{S}^{n,k}}{\delta t} \geq \frac{1}{T} \frac{\mathcal{Q}^{n,k+1} - \mathcal{Q}^{n,k}}{\delta t}, \text{ for } a^{n,k} \in [0,1] \text{ and } b^{n,k} \in [0,1], \ n \in \mathbb{N}, \ k \in [\![0, N]\!]. \tag{36}$$

If the property $a^{n,k} \in]0,1[$ and $b^{n,k} \in]0,1[$, $n \in \mathbb{N}$, $k \in [\![0, N]\!]$ holds, we can give an explicit expression of the entropy creation and we have

$$\frac{\mathcal{S}^{n,k+1} - \mathcal{S}^{n,k}}{\delta t} = \frac{\mathcal{S}^{n,k+1}_{\text{prod}} - \mathcal{S}^{n,k}_{\text{prod}}}{\delta t} + \frac{1}{T} \frac{\mathcal{Q}^{n,k+1} - \mathcal{Q}^{n,k}}{\delta t}, \tag{37}$$

with

$$
\begin{aligned}
&\frac{\mathcal{S}_{\text{prod}}^{n,k+1}-\mathcal{S}_{\text{prod}}^{n,k}}{\delta t} = \\
&\quad -\left(n_0^{n,k+1}\frac{1}{T}\frac{\delta s}{d_a}\sum_{i=1}^{\ell}\left[J_{+,1,i}^{n,k+1}\left(\mu_{1,1,i}^{n,k+1}-\mu_{0,1,i}^{n,k+1}\right)+J_{-,1,i}^{n,k+1}\left(\mu_{0,1,i}^{n,k+1}-\mu_{1,1,i}^{n,k+1}-\mu_T\right)\right]\right. \\
&\qquad \left.+(1-n_0^{n,k+1})\frac{1}{T}\frac{\delta s}{d_a}\sum_{i=1}^{\ell}\left[J_{+,0,i}^{n,k+1}\left(\mu_{1,0,i}^{n,k+1}-\mu_{0,0,i}^{n,k+1}\right)\right.\right. \\
&\qquad\qquad \left.\left.+J_{-,0,i}^{n,k+1}\left(\mu_{0,0,i}^{n,k+1}-\mu_{1,0,i}^{n,k+1}-\mu_T\right)\right]\right) \\
&\quad -v_c^{n,k+\frac{1}{2}\sharp}k_B\left(n_0^{n,k+1}\frac{1}{d_a}\sum_{i=1}^{\ell}\left[a_i^{n,k+1}\ln\left(\frac{a_{i+1}^{n,k+1}}{a_i^{n,k+1}}\right)+(1-a_i^{n,k+1})\ln\left(\frac{1-a_{i+1}^{n,k+1}}{1-a_i^{n,k+1}}\right)\right]\right. \\
&\qquad \left.+(1-n_0^{n,k+1})\frac{1}{d_a}\sum_{i=1}^{\ell}\left[b_i^{n,k+1}\ln\left(\frac{b_{i+1}^{n,k+1}}{b_i^{n,k+1}}\right)+(1-b_i^{n,k+1})\ln\left(\frac{1-b_{i+1}^{n,k+1}}{1-b_i^{n,k+1}}\right)\right]\right) \\
&\quad -\frac{k_B}{\delta t}\left(n_0^{n,k+1}\frac{\delta s}{d_a}\sum_{i=1}^{\ell}\left[a_i^{n,k}\ln\left(\frac{a_i^{n,k+1}}{a_i^{n,k}}\right)+(1-a_i^{n,k})\ln\left(\frac{1-a_i^{n,k+1}}{1-a_i^{n,k}}\right)\right]\right) \\
&\qquad \left.+(1-n_0^{n,k+1})\frac{\delta s}{d_a}\sum_{i=1}^{\ell}\left[b_i^{n,k}\ln\left(\frac{b_i^{n,k+1}}{b_i^{n,k}}\right)+(1-b_i^{n,k})\ln\left(\frac{1-b_i^{n,k+1}}{1-b_i^{n,k}}\right)\right]\right) \\
&\quad -k_B\frac{|n_0^{n,k+1}-n_0^{n,k}|_+}{\delta t}\frac{\delta s}{d_a}\sum_{i=1}^{\ell}\left[b_i^{n,k}\ln\left(\frac{a_i^{n,k+1}}{b_i^{n,k}}\right)+(1-b_i^{n,k})\ln\left(\frac{1-a_i^{n,k+1}}{1-b_i^{n,k}}\right)\right] \\
&\quad -k_B\frac{|n_0^{n,k+1}-n_0^{n,k}|_-}{\delta t}\frac{\delta s}{d_a}\sum_{i=1}^{\ell}\left[a_i^{n,k}\ln\left(\frac{a_i^{n,k}}{b_i^{n,k+1}}\right)+(1-a_i^{n,k})\ln\left(\frac{1-a_i^{n,k}}{1-b_i^{n,k+1}}\right)\right]
\end{aligned}
$$

satisfying the inequality

$$
\frac{\mathcal{S}_{\text{prod}}^{n,k+1}-\mathcal{S}_{\text{prod}}^{n,k}}{\delta t}\geq 0.
$$

If we re-write the second principle under the form of an inequality on the free energy, we have for $a^{n,k}\in[0,1]$ and $b^{n,k}\in[0,1]$

$$
\begin{aligned}
\frac{\mathcal{F}^{n,k+1}-\mathcal{F}^{n,k}}{\delta t} &= \frac{\mathcal{U}^{n,k+1}-\mathcal{U}^{n,k}}{\delta t}-T\frac{\mathcal{S}^{n,k+1}-\mathcal{S}^{n,k}}{\delta t} \\
&\leq \frac{\mathcal{W}^{n,k+1}-\mathcal{W}^{n,k}}{\delta t}+\frac{\mathcal{E}^{n,k+1}-\mathcal{E}^{n,k}}{\delta t}
\end{aligned}
$$

5.2 Numerical illustration

To illustrate the discrete thermodynamic balance, we perform a simulation of the equations (29) in a single time step scheme, i.e. $\delta t=\Delta t$. The evolution of the sliding velocity is prescribed over time. Note that this is equivalent to imposing the extension e_c^n from an initial condition e_c^0 because these two quantities are linked through (28). We choose here the initial condition $e_c^0=0.06$ and a time step $\Delta t=0.01\,\text{ms}$. The myosin head population is initially in a configuration in which all heads are detached.

The simulation starts with an isometric tension rise phase; the extension e_c^n remains constant. After a duration that is sufficient for the active force to reach its peak isometric value, the sarcomere is progressively shortened until reaching a steady-state shortening velocity of $-1\,\mu\text{m}\,\text{s}^{-1}$.

The dependency between the scaled number of available heads n_0 and the extension e_c is the same as the function that is used for the simulation of physiological heartbeats, which is presented in Figure 8(a). For the simulation, we use the transition rates and energy levels presented in Figure 12.

The results are presented in Figure 6. It can first be checked that the CFL condition (32) is satisfied in this simulation. In the initial isometric phase, myosin heads attach and the developed force increases. In

the shortening phase, the tension decreases due to two factors. When the sarcomere shortens, the force is reduced compared to isometric conditions following the classical force-velocity relation. Simultaneously, the decrease of the sarcomere extension implies a decrease in the number of available myosin heads (as shown by the decrease of $n_0(e_c)$) and thus of the force.

Being able to write consistent thermodynamical balances at the discrete level allows to investigate the elements of the energy transduction performed by the molecular motors. The work production, which is zero in the absence of displacement, increases as the muscle starts to shorten. Note that the work rate is negative because, in our length-controlled numerical experiment, the mechanical energy is transferred from the system to the environment. We now consider the consumption of chemical energy brought by ATP. As myosin heads start to cycle in the tension rise phase, the consumption of ATP increases. In the shortening phase, myosin heads are transported in a region where the detachment rate is higher. The cycling rate increases, leading to a higher consumption of ATP. We can note that the consumption of ATP is always strictly positive, even when no work is produced. This highlights the active nature of muscle contraction, i.e. the force is developed "in exchange" of a continuous supply in chemical energy. One can also note that, as expected, the entropy production term is always positive. Note that with the initial conditions ($a_i^0 = b_i^0 = 0,\ i \in [\![1, \ell]\!]$), the entropy creation term is not well defined at the initial time. After the first time step, the numerical noise combined with the non-divergence of the detachment rates on the boundaries of the interval $[s^-, s^+]$ implies that we have, for all $n > 0$ and all $i \in [\![0, \ell]\!]$, the property $a_i^n \in]0, 1[$ and $b_i^n \in]0, 1[$. The entropy creation term is thus defined for $n > 0$.

Note that a proof of the established discrete thermodynamic principles is presented in Appendix A.6.

5.3 Link with discrete macroscopic model: a multi-time step strategy

5.3.1 Macroscopic time scheme

We recall here the time scheme proposed in Kimmig et al. [2019] to discretize the macroscopic part of the system (43) and we extend it to embed the microscopic time scale dynamics in a multi-time step manner.

The numerical scheme reads

$$\begin{cases} \dfrac{\mathbf{y}^{n+1} - \mathbf{y}^n}{\Delta t} = \mathbf{v}^{n+\frac{1}{2}} = \dfrac{\mathbf{v}^{n+1} + \mathbf{v}^n}{2} & \text{(38a)} \\[2ex] \displaystyle\int_{\Omega^0} \rho_0 \frac{\mathbf{v}^{n+1} - \mathbf{v}^n}{\Delta t} \cdot \mathbf{w}\, \mathrm{d}\Omega + \int_{\Omega^0} \boldsymbol{\Sigma}^{n+\frac{1}{2}\sharp} : \mathrm{D}\mathbf{e}^{n+\frac{1}{2}\sharp} \cdot \mathbf{w}\, \mathrm{d}\Omega = \mathcal{P}_{\text{ext}}^{n+\frac{1}{2}}(\mathbf{w}),\ \mathbf{w} \in \mathscr{V}_{\text{ad}} \\ \qquad \text{with } \boldsymbol{\Sigma}^{n+\frac{1}{2}\sharp} = \dfrac{\partial \Psi}{\partial \mathbf{e}}\Big|^{n+\frac{1}{2}\sharp} + \eta \dfrac{\mathbf{e}^{n+1} - \mathbf{e}^n}{\Delta t} + \dfrac{T_{\text{fib}}^{n+\frac{1}{2}\sharp}}{(1 + 2\mathrm{f}_{\mathbf{0}} \cdot \mathbf{e}^n \cdot \mathrm{f}_{\mathbf{0}})^{\frac{1}{2}}} \mathrm{f}_{\mathbf{0}} \otimes \mathrm{f}_{\mathbf{0}} & \text{(38b)} \\[2ex] T_{\text{fib}}^{n+\frac{1}{2}\sharp} = \nu \dfrac{\dot{e}_c^{n+1} - \dot{e}_c^n}{\Delta t} + T_c^{n+1} = E_s e_s^{n+\frac{1}{2}} \\ \qquad \text{with } T_c^{n+1} = \rho_{\text{surf}} \dfrac{\delta t}{\Delta t} \displaystyle\sum_{k=0}^{N-1} \tau_c^{n,k+1} & \text{(38c)} \end{cases}$$

where we define

$$\mathbf{v}^{n+\frac{1}{2}} = \frac{\mathbf{v}^{n+1} - \mathbf{v}^n}{\delta t}, \quad \mathbf{e}^{n+\frac{1}{2}\sharp} = \mathbf{e}(\mathbf{y}^{n+\frac{1}{2}}), \quad \dot{\mathbf{e}}^{n+\frac{1}{2}\sharp} = \frac{\mathbf{e}^{n+1} - \mathbf{e}^n}{\delta t},$$
$$\mathrm{D}\,\mathbf{e}^{n+\frac{1}{2}\sharp} \cdot \mathbf{w} = \frac{1}{2}\Big(\nabla \mathbf{w} + (\nabla \mathbf{w})^{\mathsf{T}} + (\nabla \mathbf{y}^{n+\frac{1}{2}})^{\mathsf{T}} \cdot \nabla \mathbf{w} + (\nabla \mathbf{w})^{\mathsf{T}} \cdot \nabla \mathbf{y}^{n+\frac{1}{2}}\Big),$$

and

$$\frac{\partial \Psi}{\partial \mathbf{e}}\Big|^{n+\frac{1}{2}\sharp} = \frac{\partial \Psi}{\partial \mathbf{e}}(\mathbf{e}^{n+\frac{1}{2}\sharp}) + \left(\frac{\Psi(\mathbf{e}^{n+1}) - \Psi(\mathbf{e}^n)}{\delta t} - \frac{\partial \Psi}{\partial \mathbf{e}}(\mathbf{e}^{n+\frac{1}{2}\sharp}) : \dot{\mathbf{e}}^{n+\frac{1}{2}\sharp}\right) \frac{\dot{\mathbf{e}}^{n+\frac{1}{2}\sharp}}{\dot{\mathbf{e}}^{n+\frac{1}{2}\sharp} : \dot{\mathbf{e}}^{n+\frac{1}{2}\sharp}}.$$

The question that arises, when linking the time micro- and macro-dynamics, is how to properly define the macroscopic active tension T_c^{n+1} as a function of the microscopic variables. The choice made in (38c)

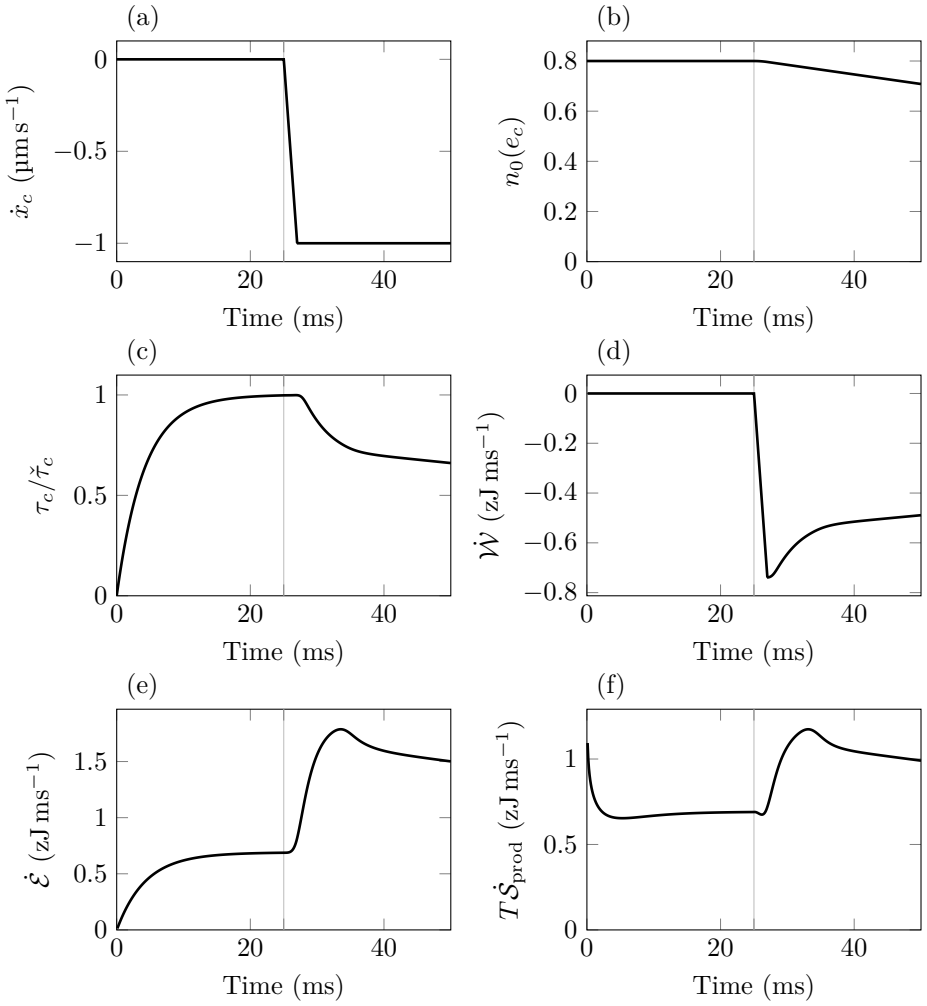

Figure 6: Simulation of the microscopic contraction model (10) with an prescribed extension e_c^n time evolution using the numerical scheme (29). (a) Sliding velocity. (b) Ratio of heads in the pool $\gamma = 1$. (c) Normalized average force per myosin head. (d) Work rate per myosin head. (e) Energy input rate per myosin head. (f) Entropy production rate per myosin head multiplied by the temperature.

will be motivated in the subsequent paragraph with the use of the discrete thermodynamic balance to lead this choice.

It is important to note that the equations in (38) must be written at each quadrature point. For the sake of compactness, this spatial dependency is omitted here.

5.3.2 Microscopic first principle at global time steps

We first extend the first thermodynamical balance of the microscopic dynamics. At a macroscopic time step, we have

$$\frac{\mathcal{U}^{n+1}-\mathcal{U}^{n}}{\Delta t}=\frac{\delta t}{\Delta t}\sum_{k=0}^{N-1}\frac{\mathcal{U}^{n,k+1}-\mathcal{U}^{n,k}}{\delta t}.$$

Using the micro time step energy balance (34), we have

$$\begin{aligned}\frac{\mathcal{U}^{n+1}-\mathcal{U}^{n}}{\Delta t}&=\frac{\delta t}{\Delta t}\sum_{k=0}^{N-1}v_c^{n+\frac{1}{2}\sharp}\tau_c^{n,k+1}+\frac{\delta t}{\Delta t}\sum_{k=0}^{N-1}\left[\frac{\mathcal{Q}^{n,k+1}-\mathcal{Q}^{n,k}}{\delta t}+\frac{\mathcal{E}^{n,k+1}-\mathcal{E}^{n,k}}{\delta t}\right]\\&=\frac{\mathcal{W}^{n+1}-\mathcal{W}^{n}}{\Delta t}+\frac{\mathcal{Q}^{n+1}-\mathcal{Q}^{n}}{\Delta t}+\frac{\mathcal{E}^{n+1}-\mathcal{E}^{n}}{\Delta t}\end{aligned}$$

where we define the macroscopic force by

$$T_c^{n+1}=\frac{\delta t}{\Delta t}\sum_{k=0}^{N-1}\tau_c^{n,k+1}=\frac{\delta t}{\Delta t}\sum_{k=0}^{N-1}\frac{\delta s}{d_a}\sum_{i=1}^{\ell}\frac{w_{1,i+1}-w_{1,i}}{\delta s}\left(n_0^{n,k+1}a^{n,k+1}+(1-n_0^{n,k+1})b^{n,k+1}\right)$$

and the macroscopic time step work flux per myosin head by

$$\frac{\mathcal{W}^{n+1}-\mathcal{W}^{n}}{\Delta t}=v_c^{n+\frac{1}{2}\sharp}T_c^{n+1}.$$

We can note that the force at macroscopic time step is not the force corresponding to the simultaneous microscopic time step but the time average of the microscopic time force over the macro time step. The energy balance thus allows to properly perform the link between time scales.

5.3.3 Microscopic second principle at global time steps

Then, we extend the second thermodynamical balance of the microscopic dynamics. At a macroscopic time step, we have

$$\frac{\mathcal{F}^{n+1}-\mathcal{F}^{n}}{\Delta t}=\frac{\delta t}{\Delta t}\sum_{k=0}^{N-1}\frac{\mathcal{F}^{n,k+1}-\mathcal{F}^{n,k}}{\delta t}.$$

Using the micro time step free energy inequality (36), we have

$$\begin{aligned}\frac{\mathcal{F}^{n+1}-\mathcal{F}^{n}}{\Delta t}&\leq\frac{\delta t}{\Delta t}\sum_{k=0}^{N-1}\frac{\mathcal{W}^{n,k+1}-\mathcal{W}^{n,k}}{\delta t}+\frac{\delta t}{\Delta t}\sum_{k=0}^{N-1}\frac{\mathcal{E}^{n,k+1}-\mathcal{E}^{n,k}}{\delta t}\\&\leq\frac{\mathcal{W}^{n+1}-\mathcal{W}^{n}}{\Delta t}+\frac{\mathcal{E}^{n+1}-\mathcal{E}^{n}}{\Delta t},\end{aligned}\tag{39}$$

with the definition of the macroscopic time step energy input flux

$$\frac{\mathcal{E}^{n+1}-\mathcal{E}^{n}}{\Delta t}=\frac{\delta t}{\Delta t}\sum_{k=0}^{N-1}\frac{\mathcal{E}^{n,k+1}-\mathcal{E}^{n,k}}{\delta t}.$$

The inequality on the free-energy is thus straightforwardly transferred to the macroscopic time scale.

5.3.4 Discrete time Clausius-Duhem relation for the complete model

Having a microscopic discrete model, which satisfies the macroscopic time step inequality (39), we can apply and adapt the thermodynamic balance obtained in [Kimmig et al., 2019] for the micro-macro coupled model. We have

$$\frac{\mathcal{K}^{n+1}-\mathcal{K}^{n}}{\delta t}+\int_{\Omega^0}\Big[\frac{\Psi^{n+1}-\Psi^{n}}{\delta t}+E_s\frac{|e_s^{n+1}|^2-|e_s^{n}|^2}{2\delta t}+\rho_v\frac{\mathcal{F}^{n+1}-\mathcal{F}^{n}}{\delta t}\Big]\,\mathrm{d}\Omega \\ \leq \mathcal{P}_{\mathrm{ext}}^{n+\frac{1}{2}}-\int_{\Omega^0}\Big[\eta\frac{|\mathbf{e}^{n+1}-\mathbf{e}^{n}|^2}{\delta t^2}+\nu\frac{(e_c^{n+1}-e_c^{n})^2}{\delta t^2}\Big]\,\mathrm{d}\Omega+\int_{\Omega^0}\rho_v\frac{\mathcal{E}^{n+1}-\mathcal{E}^{n}}{\delta t},$$

where the density of myosin head per unit volume is defined as $\rho_v=\rho_{\mathrm{surf}}/\ell_{hs}$.

In summary, the proposed numerical scheme satisfies discrete thermodynamical balances at the microscopic time step. A definition of the macroscopic active force guided by thermodynamics allows to extend these discrete thermodynamic balances to the micro-macro coupled model.

6 Numerical illustration: physiological simulations of a heartbeat

We now want to show the ability of our model to produce a physiologically relevant behavior in the context of cardiovascular modeling. To this end, we incorporate our microscopic contraction model in a macroscopic heart model with a simplified geometry [Caruel et al., 2013a], which is an intermediate modeling hypothesis between a complete 3D finite element description of the heart and a model with Laplace estimates [Gsell et al., 2018]. A dedicated – thermodynamically consistent – numerical scheme is formulated for this model, extending that proposed in [Kimmig et al., 2019] for the system without the pool exchange terms. The discrete thermodynamic balances at the microscopic level can then be followed up to the macroscopic level. A detailed presentation of the numerical method proposed was given in Section 5.

We first need to embed into the model the regulation of the thin filament activation. It is done here in a phenomenological way. Then, we present the physiological calibration used in our simulations and the simulation results.

6.1 Modification to account for the thin filament activation

We have presented above a model allowing to capture the varying levels of thick filament activation in the sarcomere. However, it is not the only regulation mechanism in a physiological contraction. The thin filament activation level is also varied as a function of the sarcomere stretch (intrinsic regulation) and the intracellular calcium dynamics depends on the inputs of the neuroendocrine system (extrinsic regulation) [de Tombe et al., 2010].

Many models have been developed following the seminal work of Rice et al. [2003] for the description of the thin filament activation underlying mechanisms displaying various levels of refinement and computational efficiency [Rice & de Tombe, 2004; Hussan et al., 2006; Rice et al., 2008; Washio et al., 2011; Regazzoni et al., 2018]. Moreover, a coupled model of the thin filament activation and the actin-myosin interaction has been proposed for a special case of thick filament activation model in [Regazzoni et al., 2020]. In this paper, however, we focus our modeling effort on the activation of the thick filament, and we treat the activation of the thin filament phenomenologically.

Following the idea proposed by Zahalak & Motabarzadeh [1997] and Chapelle et al. [2012], we place the impact of the thin filament regulation on the transition rates. We assume that the attachment rate $k_{+,\gamma}(s)$ and its reverse $k_{+,\gamma}^{\mathrm{rev}}(s)$ is modulated multiplicatively by a phenomenological activation function u. The complexity of the underlying mechanisms is incorporated into the freedom in the choice of the activation function u. This function varies between zero and one, representing a level of activation that

modulates the rate of attachment. The model dynamics equation (10) becomes

$$\begin{cases} \partial_t P_1(s,t,1) + \dot{x}_c\,\partial_s P_1(s,t,1) + \dfrac{|\dot{n}_0|_+}{n_0}\big[P_1(s,t,1) - P_1(s,t,0)\big] = \\ \qquad\qquad \big(u(t)k_{+,1}(s) + k^{\mathrm{rev}}_{-,1}(s)\big)P_0(s,t,1) - \big(k_{-,1}(s) + u(t)k^{\mathrm{rev}}_{+,1}(s)\big)P_1(s,t,1), \\ \partial_t P_1(s,t,0) + \dot{x}_c\,\partial_s P_1(s,t,0) + \dfrac{|\dot{n}_0|_-}{1-n_0}\big[P_1(s,t,0) - P_1(s,t,1)\big] = \\ \qquad\qquad \big(u(t)k_{+,0}(s) + k^{\mathrm{rev}}_{-,0}(s)\big)P_0(s,t,0) - \big(k_{-,0}(s) + u(t)k^{\mathrm{rev}}_{+,0}(s)\big)P_1(s,t,0), \\ P_0(s,t,\gamma) = 1 - P_1(s,t,\gamma). \end{cases} \tag{40}$$

With this modification that preserves the detailed balance (3), the model remains straightforwardly compatible with the second principle.

6.2 Model calibration

We now want to calibrate our model. Our objective is to show the ability of the model to semi-quantitatively capture the Frank-Starling mechanism and not to precisely match physiological pressure-volume data for a given individual. We thus take the liberty to use data coming from different species. The heart model parameters, except for the actin-myosin interaction model, are calibrated to represent a human physiological behavior (patient-specific calibrations can be found in [Le Gall et al., 2020]). The proposed micro-scale model of the actin-myosin interaction and its regulation provide a detailed description of the mechanisms involved. The model calibration thus requires accurate data obtained *ex vivo* targeting the short time and space scales of the muscle contraction. These data are not available for human to the best of our knowledge and we will use instead measurements from rats obtained at sub-physiological temperatures. For the actin-myosin interaction model, we rely on the calibration proposed in [Kimmig & Caruel, 2019] based on data obtained by physiologists Caremani et al. [2016]; de Tombe & ter Keurs [1992] and adapted for the non-aggregated transition rates for the pool $\gamma = 1$ (see Appendix A.4). For the pool $\gamma = 0$, we use the modeling assumption $k_{+,0} = 0.01k_{+,1}$ and $k_{-,0} = k_{-,1}$. Note that this calibration allows to capture the force-velocity relation and the isometric indicators (ratio of attached myosin heads and force per attached myosin head).

We then calibrate the input function $n_0(e_c)$ and finally define the thin filament activation function $u(t)$.

6.2.1 Myosin activation function

To relate the measured force to the scaled number of available myosin heads n_0, we use experiments performed on *ex vivo* muscle cells, which are either intact tetanised cells or skinned cells, measuring the relation between the steady-state isometric peak force and the sarcomere length in full thin filament activation conditions, so that the variation in force can be attributed solely to variations in the myosin heads availability. We aggregate here data collected by Kentish et al. [1986], ter Keurs et al. [2008] and Dobesh et al. [2002].

Note that the extension e_c, which we consider as the argument of the thick filament activation function n_0, adds up to the filament self extension e_s, which depends on the developed active force, to give the sarcomere extension e_{fib}. The latter quantity is the extension that can be directly linked to the sarcomere length, which is observed experimentally. We thus need to consider the experimental data in the light of the rheology model (the complete rheology is presented in Appendix A.2 Figure 11). The range of sarcomere length that is used in experimental conditions spans between 1.65 µm and 2.25 µm. In this range, the passive force is small compared to the active force (see for instance [ter Keurs et al., 2008, Fig. 2] or [Caremani et al., 2016, Fig. 1B]). We thus interpret the measured force as resulting solely from the 1D sarcomere-based branch of the rheology (see Figure 7(a)). Recalling that the sarcomere half-length corresponding to zero passive force – called *slack length* – is denoted by ℓ_{hs}, the half-sarcomere length in steady-state contraction conditions is given by $\ell_{hs}\big(1 + e_{\mathrm{fib}}\big)$ with

$$\begin{cases} e_{\mathrm{fib}} = e_c + e_s, \\ E_s e_s = \check{T}_c\big(n_0(e_c)\big), \end{cases}$$

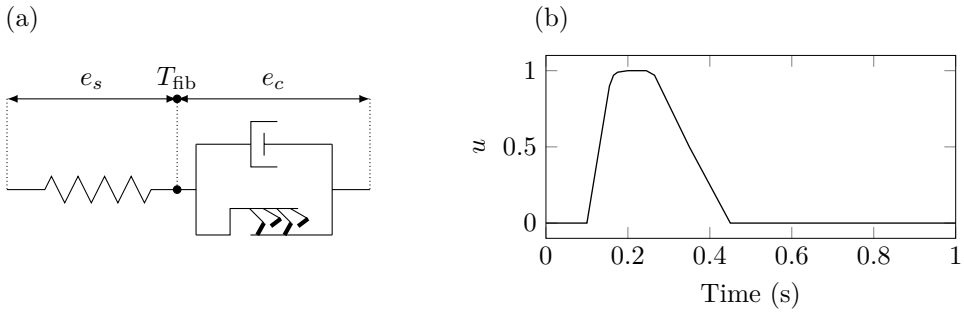

Figure 7: (a) Part of the half-sarcomere rheology that accounts for the actin and myosin filaments contribution. The spring and dashpot represent the intrinsic elastic and viscous properties of the filament, while the myosin heads sketch represent the cross-bridges, which are here described with the newly proposed extended Huxley'57-model. (b) Phenomenological thin filament activation function. This function aggregates the calcium triggered activation and the effects of the intrinsic thin filament regulation.

denoting by $\check{T}_c$ the steady state value of T_c given by

$$\check{T}_c\big(n_0(e_c)\big) = \rho_{\text{surf}} \frac{1}{d_a} \int_{s^-}^{s^+} \big[n_0 \check{P}_1(s,1) + (1-n_0)\check{P}_1(s,0)\big] \partial_s w_1(s)\, \mathrm{d}s,$$

where $\check{P}_1(\gamma) = \frac{f_\gamma}{f_\gamma + g_\gamma}$ is the steady-state solution of (40) with $\dot{x}_c = 0$ and in maximal activation conditions ($n_0 = 1$ and $u = 1$). Normalizing the tensions by the maximal isometric tension

$$T_0 = \rho_{\text{surf}} \frac{1}{d_a} \int_{s^-}^{s^+} \check{P}_1(s,1) \partial_s w_1(s)\, \mathrm{d}s,$$

we seek a function $n_0(e_c)$ such that the model predicted $\big(\ell_{hs}(e_{\text{fib}}), \check{T}_c\big(n_0(e_c)\big)/T_0\big)$-curve matches the experimental data. These data corresponding to a complete thin filament activation, the function u is maintained equal to one here and we simulate the steady-state response in force of the model. As for most elements of the rheology, the slack length is taken from measurements on human cardiac cells. We use the value $\ell_{hs} = 1.7\,\mu\text{m}$ [van der Velden et al., 2000]. The calibration results and the validation are presented in Figure 8.

6.2.2 Actin activation function

The actin activation function u is phenomenologically defined to mimic the transient activation of the thin filament following the triggering of the action potential in the cell. In a first phase, calcium is released from the sarcoplasmic reticulum and transiently adsorbed by the thin filament; the level of activation increases and reaches its maximal value – assumed here to be equal to one. The calcium ions are then re-uptaken by the sarcoplasmic reticulum and the level of activation decreases until it vanishes. The liberation of calcium is then prevented during a so-called *refractory period*, which ensures that the heart has time to relax before the next contraction. The proposed function $u(t)$ is presented in Figure 7(b).

6.3 Numerical results

At the macroscopic level, de Tombe et al. [2010] characterize the Frank-Starling mechanism by two features: (1) the stroke volume is increased with an increase of the end-diastolic volume (i.e. increasing the pre-load) and (2) the stroke volume can be maintained in case of an increased after-load by increasing the end-diastolic volume. Altogether, they state that a comprehensive view of this mechanism is to say that there is a single end-systolic pressure-volume relation (ESPVR).

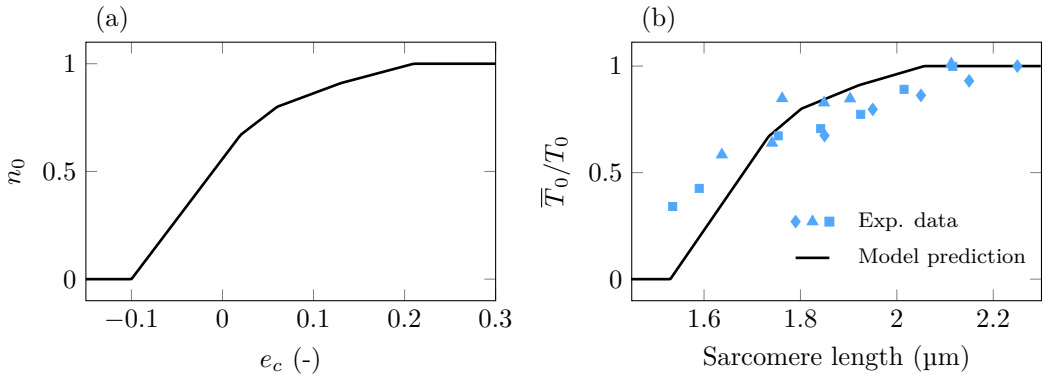

Figure 8: (a) Calibrated input parameter function $n_0(e_c)$. (b) Validation of the calibration with the relation between the sarcomere length and the isometric force in maximal thin filament activation conditions. Solid line: model prediction. Diamonds: data from skinned rat cells [Dobesh et al., 2002]. Triangles: data from intact tetanised rat cardiac muscle cells [ter Keurs et al., 2008]. Squares: data from skinned rat ventricular trabeculae [Kentish et al., 1986].

6.3.1 Physiological pressure-volume loop

The simulation results with the calibrated thick and thin filament activation functions are presented in Figure 9. We see in the panel (a) that an increase in the pre-load results in an increase of the ejected blood volume. Our model thus captures the first feature of the Frank-Starling mechanism. In the panel (b), we show that the second feature is also encompassed in our model.

Additionally, we plot the static (ESPVR) that can be computed from the simplified 0D-model equation in the static case (see [Caruel et al., 2013a]). The analytical expression of the ESPVR is recalled in Appendix A.3.

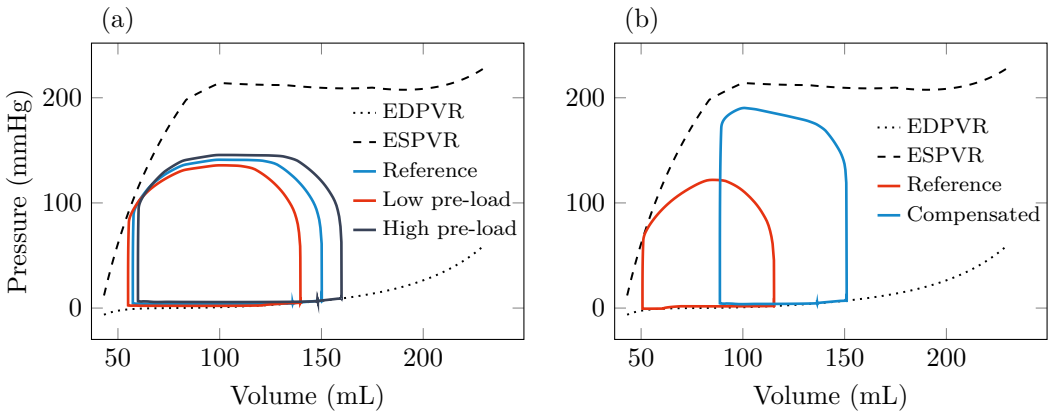

Figure 9: Relation between the ventricular pressure and the ventricular volume during a simulated heartbeat (PV-loop). We present here the limit cycle for the pressure-volume relationship. (a) Variation of the pre-load, which changes the end-diastolic volume. (b) Comparison between a reference and a case where a higher after-load is compensated by an increased pre-load to maintain the ejected blood volume constant. (a) & (b) The dashed line represents the static ESPVR. The dotted line represents the End-Diastolic Pressure Volume Relation (EDPVR).

In a nutshell, our model based on a microscopic description of the actin-myosin interaction coupled with a macroscopic description of the muscle tissue and embedded into a cardiovascular model is able to capture the key features of the Frank-Starling mechanism at the macroscopic level.

6.3.2 Impact of the micro models on the macroscopic physiology

In this section, we want to highlight the impact of the force-velocity relationship captured by the model for a physiological heartbeat.

We compare the simulations of a heartbeat with two different calibrations of the transition rates. The isometric values of the transitions rates are either taken from [Kimmig & Caruel, 2019] or mimic those proposed in [de Tombe & Stienen, 2007] (see Figure 10(a) & (b)). The force-velocity relation associated with these two model calibrations are presented in Figure 10(c). With the calibration from [Kimmig & Caruel, 2019], the steady-state force is higher for all velocities than the same relation computed with the calibration inspired by [de Tombe & Stienen, 2007]. We thus denote this first calibration *high force-velocity* (HFV) and as opposed to the *low force-velocity* calibration (LFV).

Note that both simulations use the calibration of n_0 and u presented in Section 6.2.1. In the early contraction phase, the aortic valve is closed and the muscle works in isometric conditions. As soon as the valve opens, the heart cavity volume decreases and the sarcomere shortens. This shortening results in a decrease in the force following the force-velocity curve, under the approximation that the population probability $P_1(s,t)$ quickly converges to its steady-state counterpart (this is true if the cycling time scale is shorter than the duration of the systole).

We now compare the pressure-volume loops obtained with the two calibrations. When the force-velocity relation predicts a strong decrease of the force with increasing shortening velocities, the opening of the valve (and the beginning of the sarcomere shortening) leads to a drastic decrease of the active force. As a result, the pressure that can be created in the heart cavity is limited due to the limited time of activation (see Figure 10(d)). This further leads to a reduction of the stroke volume because the heart is not able to oppose the aortic pressure long enough.

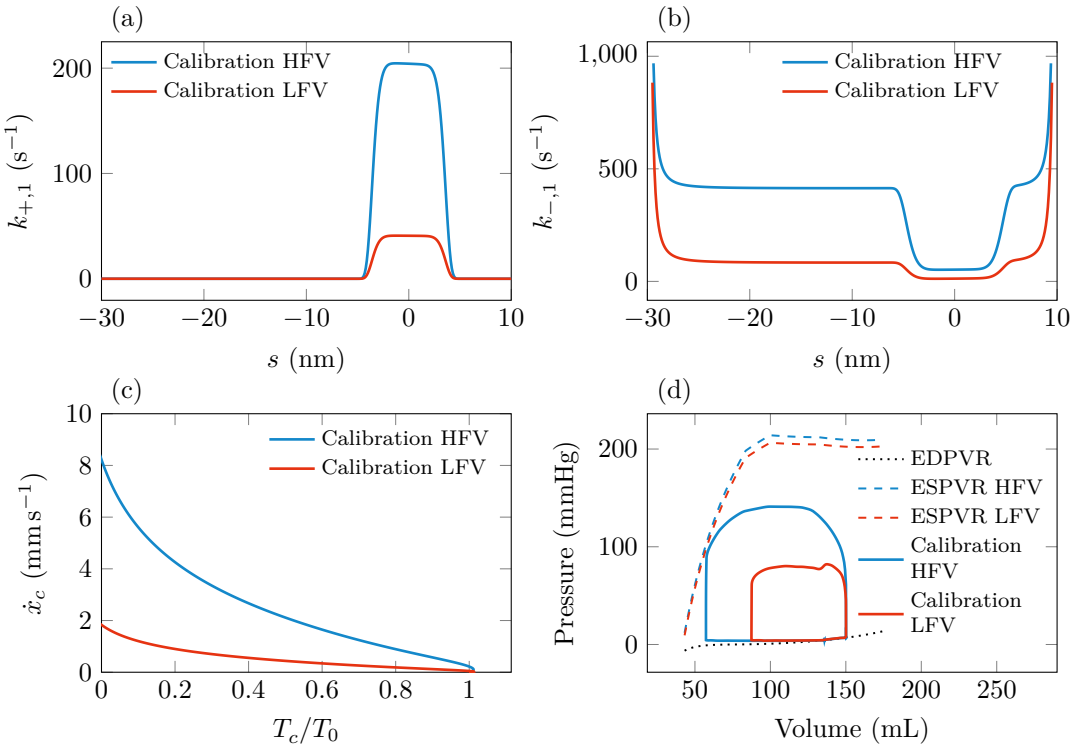

Figure 10: Comparison of high force-velocity calibration (HFV) with low force-velocity calibration (LFV). The two calibrations only differ by the choice of the transition rates. We present here the limit cycle for the pressure-volume relationship. (a) Attachment rates for both calibrations. (b) Detachment rates for both calibrations. (c) Resulting force-velocity relation with both calibrations. (d) Force-velocity relation obtained in a heartbeat simulation with both calibrations.

The force-velocity is thus important in the calibration to allow the heart to eject blood sufficiently fast while maintaining a high enough blood pressure to avoid the closing of the aortic valve.

7 Conclusion

In this paper, we have presented a new paradigm that extends the family of models derived from the seminal work of A.F. Huxley [Huxley, 1957] to take into account the activation of the thick filament. The thermodynamical compatibility of the newly proposed model is established. A discrete counterpart of the thermodynamics balances is also obtained with a dedicated discretization scheme.

As a consequence of the investigation of our model range of validity, we showed that the inclusion of a memory effect in the transition between the available and non-available states for the myosin heads is not useful in physiological conditions. Indeed, the attachment-detachment process occurs fast enough to eliminate this memory effect.

This work suffers from two main limitations in the context of physiological heart modeling. First, the activation of the thin filament has been incorporated in a phenomenological way. There remains a need for the development of a rigorous thin filament activation modeling. Secondly, the extrinsic regulation controlled by the neuroendocrine system is not considered in this model. A limitation in this regard is the difficulty to obtain sarcomere level data – with which the microscopic level model can be calibrated – that also consider the impact of the neuroendocrine system, because extraction of muscle samples from the body separates them from this system. In our approach, we get around these two limitations by incorporating these effects phenomenologically into the activation function u. We are then able to display the ability of our model to capture the two essential features of the Frank-Starling mechanism.

Note that a physiological pressure-volume relation can also be obtained with less refined models of the actomyosin interaction, for instance models that only track the first two moments of the probability of being attached P_1 [Chapelle et al., 2012]. This is because the heartbeat time scale is long compared to the actin-myosin interaction time scales and thus capturing the main features of this interaction is enough to produce physiological results at the heartbeat time scale. However, our framework allows to better describe the physical mechanisms underlying the contraction and thus allows to take into account changes in these mechanisms – for instance as a result of pathologies – more easily.

A Appendices

A.1 Proof of the thermodynamical balances at the continuous level

In this section, we detail, for the sake of completness, the derivation of the thermodynamical balances presented in Section 3.

A.1.1 First principle

The differentiation of the internal energy (15) yields

$$\begin{aligned}\frac{\mathrm{d}}{\mathrm{d}t}\mathcal{U}(t) = \frac{1}{d_a}\int_{s^-}^{s^+}\Big(&\dot{n}_0\Big[w_1(s)\big[P_1(s,t,1)-P_1(s,t,0)\big]+w_0\big[P_0(s,t,1)-P_0(s,t,0)\big]\Big]\\ &+n_0(t)\Big[w_1(s)\,\partial_t P_1(s,t,1)+w_0\,\partial_t P_0(s,t,1)\Big]\\ &+\big(1-n_0(t)\big)\Big[w_1(s)\,\partial_t P_1(s,t,0)+w_0\,\partial_t P_0(s,t,0)\Big]\Big)\,\mathrm{d}s.\end{aligned} \tag{41}$$

The treatment of the chemical reaction and the transport terms arising from $\partial_t P_1(s,t,\gamma)$ and $\partial_t P_0(s,t,\gamma)$ is given in [Hill, 1977] (see also [Kimmig et al., 2019] for the detailed calculation). Therefore, we just

detail here the contribution arising from the pool exchange term. Equation (41) becomes

$$\begin{aligned}\frac{\mathrm{d}}{\mathrm{d}t}\mathcal{U}(t) &= \mu_T \overline{J}_-(t) + \dot{x}_c \tau_c(t) \\ &+ \frac{1}{d_a}\int_{s^-}^{s^+} \Big(n_0 \Big[(w_1(s) - w_0) J_+(s,t,1) + (w_0 - (w_1(s) + \mu_T)) J_-(s,t,1) \Big] \\ &\qquad + (1-n_0)\Big[(w_1(s) - w_0) J_+(s,t,0) + (w_0 - (w_1(s) + \mu_T)) J_-(s,t,0) \Big] \Big)\, \mathrm{d}s \\ &+ \frac{1}{d_a}\int_{s^-}^{s^+} \dot{n}_0 \Big[w_1(s)\big[P_1(s,t,1) - P_1(s,t,0)\big] + w_0\big[P_0(s,t,1) - P_0(s,t,0)\big] \Big]\, \mathrm{d}s \\ &- \frac{1}{d_a}\int_{s^-}^{s^+} \Big(n_0 \Big[w_1(s) \frac{|\dot{n}_0|_+}{n_0}\big[P_1(s,t,1) - P_1(s,t,0)\big] + w_0 \frac{|\dot{n}_0|_+}{n_0}\big[P_0(s,t,1) - P_0(s,t,0)\big] \Big] \\ &\qquad + (1-n_0)\Big[w_1(s)\frac{|\dot{n}_0|_-}{1-n_0}\big[P_1(s,t,0) - P_1(s,t,1)\big] \\ &\qquad\qquad + w_0 \frac{|\dot{n}_0|_-}{1-n_0}\big[P_0(s,t,0) - P_0(s,t,1)\big] \Big] \Big)\, \mathrm{d}s.\end{aligned}$$

Using the property (5), the last two integrals in (A.1.1) cancel out. We finally have (16),

$$\dot{\mathcal{U}}(t) = \dot{\mathcal{W}}(t) + \dot{\mathcal{E}}(t) + \dot{\mathcal{Q}}(t).$$

A.1.2 Second principle

We differentiate the free energy defined in (19).

We have

$$\begin{aligned}\frac{\mathrm{d}}{\mathrm{d}t}\mathcal{F}(t) = \frac{1}{d_a}\int_{s^-}^{s^+} \Big(&\dot{n}_0 \Big[P_1(s,t,1)\mu_1(s,t,1) + P_0(s,t,1)\mu_0(s,t,1) \\ &\qquad - P_1(s,t,0)\mu_1(s,t,0) - P_0(s,t,0)\mu_0(s,t,0) \Big] \\ &+ n_0 \Big[P_1(s,t,1)\,\partial_t\mu_1(s,t,1) + \mu_1(s,t,1)\,\partial_t P_1(s,t,1) \\ &\qquad + P_0(s,t,1)\,\partial_t\mu_0(s,t,1) + \mu_0(s,t,1)\,\partial_t P_0(s,t,1) \Big] \\ &+ (1-n_0)\Big[P_1(s,t,0)\,\partial_t\mu_1(s,t,0) + \mu_1(s,t,0)\,\partial_t P_1(s,t,0) \\ &\qquad + P_0(s,t,0)\,\partial_t\mu_0(s,t,0) + \mu_0(s,t,0)\,\partial_t P_0(s,t,0) \Big] \Big)\, \mathrm{d}s.\end{aligned}$$

The time derivative of the chemical potentials times the probability P_α being given by

$$P_\alpha(s,t,\gamma)\,\partial_t\mu_\alpha(s,t,\gamma) = k_B T\,\partial_t P_\alpha(s,t,\gamma)\, \alpha \in \{0,1\} \text{ and } \gamma \in \{0,1\},$$

we obtain that

$$\begin{aligned}&n_0\Big[P_1(s,t,1)\,\partial_t\mu_1(s,t,1) + P_0(s,t,1)\,\partial_t\mu_0(s,t,1)\Big] \\ &\qquad + (1-n_0)\Big[P_1(s,t,0)\,\partial_t\mu_1(s,t,0) + P_0(s,t,0)\,\partial_t\mu_0(s,t,0)\Big] \\ &\qquad = n_0 k_B T\,\partial_t\Big[P_1(s,t,1) + P_0(s,t,1)\Big] + (1-n_0)k_B T\,\partial_t\Big[P_1(s,t,0) + P_0(s,t,0)\Big],\end{aligned}$$

which is equal to zero from the conservation of myosin heads. Introducing the dynamics equations (10),

the time derivative of the free energy becomes

$$
\begin{aligned}
\frac{\mathrm{d}}{\mathrm{d}t}\mathcal{F}(t) = \frac{1}{d_a}\int_{s^-}^{s^+}\Big(&\dot{n}_0\Big[P_1(s,t,1)\mu_1(s,t,1) + P_0(s,t,1)\mu_0(s,t,1) \\
&\qquad - P_1(s,t,0)\mu_1(s,t,0) - P_0(s,t,0)\mu_0(s,t,0)\Big] \\
&+ n_0\Big[\mu_1(s,t,1)\Big(- \dot{x}_c\partial_s P_1(s,t,1) - \frac{|\dot{n}_0|_+}{n_0}\big[P_1(s,t,1) - P_1(s,t,0)\big] \\
&\qquad + \big(k_{+,1}(s) + k^{\mathrm{rev}}_{-,1}(s)\big)\big(1 - P_1(s,t,1)\big) - \big(k_{-,1}(s) + k^{\mathrm{rev}}_{+,1}(s)\big)P_1(s,t,1)\Big) \\
&\qquad + \mu_0(s,t,1)\Big(\dot{x}_c\partial_s P_1(s,t,1) + \frac{|\dot{n}_0|_+}{n_0}\big[P_1(s,t,1) - P_1(s,t,0)\big] \\
&\qquad\quad - \big(k_{+,1}(s) + k^{\mathrm{rev}}_{-,1}(s)\big)\big(1 - P_1(s,t,1)\big) + \big(k_{-,1}(s) + k^{\mathrm{rev}}_{+,1}(s)\big)P_1(s,t,1)\Big)\Big] \\
&+ (1-n_0)\Big[\mu_1(s,t,0)\Big(- \dot{x}_c\partial_s P_1(s,t,0) - \frac{|\dot{n}_0|_-}{1-n_0}\big[P_1(s,t,0) - P_1(s,t,1)\big] \\
&\qquad + \big(k_{+,0}(s) + k^{\mathrm{rev}}_{-,0}(s)\big)\big(1 - P_1(s,t,0)\big) - \big(k_{-,0}(s) + k^{\mathrm{rev}}_{+,0}(s)\big)P_1(s,t,0)\Big) \\
&\qquad + \mu_0(s,t,0)\Big(\dot{x}_c\partial_s P_1(s,t,0) + \frac{|\dot{n}_0|_-}{1-n_0}\big[P_1(s,t,0) - P_1(s,t,1)\big] \\
&\qquad\quad - \big(k_{+,0}(s) + k^{\mathrm{rev}}_{-,0}(s)\big)\big(1 - P_1(s,t,0)\big) + \big(k_{-,0}(s) + k^{\mathrm{rev}}_{+,0}(s)\big)P_1(s,t,0)\Big)\Big]\Big)\,\mathrm{d}s.
\end{aligned}
\tag{42}
$$

Adapting the calculation performed in [Kimmig et al., 2019] for the derivation of the second principle in the usual family of Huxley'57 models, we obtain that

$$
\begin{aligned}
&\frac{1}{d_a}\int_{s^-}^{s^+}\Big(n_0\Big[\mu_1(s,t,1)\Big(\big(k_{+,1}(s) + k^{\mathrm{rev}}_{-,1}(s)\big)\big(1 - P_1(s,t,1)\big) \\
&\qquad\qquad - \big(k_{-,1}(s) + k^{\mathrm{rev}}_{+,1}(s)\big)P_1(s,t,1) - \dot{x}_c\,\partial_s P_1(s,t,1)\Big) \\
&\qquad + \mu_0(s,t,1)\Big(- \big(k_{+,1}(s) + k^{\mathrm{rev}}_{-,1}(s)\big)\big(1 - P_1(s,t,1)\big) \\
&\qquad\qquad + \big(k_{-,1}(s) + k^{\mathrm{rev}}_{+,1}(s)\big)P_1(s,t,1) + \dot{x}_c\,\partial_s P_1(s,t,1)\Big)\Big] \\
&\quad + (1-n_0)\Big[\mu_1(s,t,0)\Big(\big(k_{+,0}(s) + k^{\mathrm{rev}}_{-,0}(s)\big)\big(1 - P_1(s,t,0)\big) \\
&\qquad\qquad - \big(k_{-,0}(s) + k^{\mathrm{rev}}_{+,0}(s)\big)P_1(s,t,0) - \dot{x}_c\,\partial_s P_1(s,t,0)\Big) \\
&\qquad + \mu_0(s,t,0)\Big(- \big(k_{+,0}(s) + k^{\mathrm{rev}}_{-,0}(s)\big)\big(1 - P_1(s,t,0)\big) \\
&\qquad\qquad + \big(k_{-,0}(s) + k^{\mathrm{rev}}_{+,0}(s)\big)P_1(s,t,0) + \dot{x}_c\,\partial_s P_1(s,t,0)\Big)\Big]\Big)\,\mathrm{d}s \\
&= \dot{\mathcal{W}}(t) + \dot{\mathcal{E}}(t) \\
&\quad + \frac{1}{d_a}\int_{s^-}^{s^+}\Big(n_0\Big[J_-(s,t,1)\big[\mu_0(s,t,1) - \big(\mu_1(s,t,1) + \mu_T\big)\big] \\
&\qquad\qquad + J_+(s,t,1)\big[\mu_1(s,t,1) - \mu_0(s,t,1)\big]\Big] \\
&\qquad + (1-n_0)\Big[J_-(s,t,0)\big[\mu_0(s,t,0) - \big(\mu_1(s,t,0) + \mu_T\big)\big] \\
&\qquad\qquad + J_+(s,t,0)\big[\mu_1(s,t,0) - \mu_0(s,t,0)\big]\Big]\Big)\,\mathrm{d}s.
\end{aligned}
$$

Using the calculation made for the derivation of the energy balance, we have

$$\begin{aligned}
&\dot{n}_0\Big[P_1(s,t,1)w_1(s) + P_0(s,t,1)w_0 - P_1(s,t,0)w_1(s) - P_0(s,t,0)w_0\Big] \\
&\qquad - \Bigg(n_0\Big[w_1(s)\frac{|\dot{n}_0|_+}{n_0}\big[P_1(s,t,1) - P_1(s,t,0)\big] - w_0\frac{|\dot{n}_0|_+}{n_0}\big[P_1(s,t,1) - P_1(s,t,0)\big]\Big] \\
&\qquad + (1-n_0)\Big[w_1(s)\frac{|\dot{n}_0|_-}{1-n_0}\big[P_1(s,t,0) - P_1(s,t,1)\big] - w_0\frac{|\dot{n}_0|_-}{1-n_0}\big[P_1(s,t,0) - P_1(s,t,1)\big]\Big]\Bigg) = 0.
\end{aligned}$$

Finally, we have using the property (5)

$$\begin{aligned}
&\dot{n}_0 k_B T\Big[P_1(s,t,1)\ln\big[P_1(s,t,1)\big] + P_0(s,t,1)\ln\big[P_0(s,t,1)\big] \\
&\qquad\qquad - P_1(s,t,0)\ln\big[P_1(s,t,0)\big] - P_0(s,t,0)\ln\big[P_0(s,t,0)\big]\Big] \\
&- n_0 k_B T\Big[\ln\big[P_1(s,t,1)\big]\frac{|\dot{n}_0|_+}{n_0}\big[P_1(s,t,1) - P_1(s,t,0)\big] \\
&\qquad\qquad + \ln\big[P_0(s,t,1)\big]\frac{|\dot{n}_0|_+}{n_0}\big[P_0(s,t,1) - P_0(s,t,0)\big]\Big] \\
&- (1-n_0)k_B T\Big[\ln\big[P_1(s,t,0)\big]\frac{|\dot{n}_0|_-}{1-n_0}\big[P_1(s,t,0) - P_1(s,t,1)\big] \\
&\qquad\qquad + \ln\big[P_0(s,t,0)\big]\frac{|\dot{n}_0|_-}{1-n_0}\big[P_0(s,t,0) - P_0(s,t,1)\big]\Big] \\
&= k_B T\Bigg(P_1(s,t,1)|\dot{n}_0|_-\Big[-\ln\big[P_1(s,t,1)\big] + \ln\big[P_1(s,t,0)\big]\Big] \\
&\qquad\qquad + P_0(s,t,1)|\dot{n}_0|_-\Big[-\ln\big[P_0(s,t,1)\big] + \ln\big[P_0(s,t,0)\big]\Big] \\
&\qquad\qquad + P_1(s,t,0)|\dot{n}_0|_+\Big[-\ln\big[P_1(s,t,0)\big] + \ln\big[P_1(s,t,1)\big]\Big] \\
&\qquad\qquad + P_0(s,t,0)|\dot{n}_0|_+\Big[-\ln\big[P_0(s,t,0)\big] + \ln\big[P_0(s,t,1)\big]\Big]\Bigg) \\
&= -k_B T\Bigg[|\dot{n}_0|_+\Big[\ln\left(\frac{P_1(s,t,0)}{P_1(s,t,1)}\right)P_1(s,t,0) + \ln\left(\frac{1-P_1(s,t,0)}{1-P_1(s,t,1)}\right)\big(1-P_1(s,t,0)\big)\Big] \\
&\qquad\qquad + |\dot{n}_0|_-\Big[\ln\left(\frac{P_1(s,t,1)}{P_1(s,t,0)}\right)P_1(s,t,1) + \ln\left(\frac{1-P_1(s,t,1)}{1-P_1(s,t,0)}\right)\big(1-P_1(s,t,1)\big)\Big]\Bigg].
\end{aligned}$$

Altogether, (42) becomes

$$\begin{aligned}\frac{\mathrm{d}}{\mathrm{d}t}\mathcal{F}(t) = \dot{\mathcal{W}}(t) + \dot{\mathcal{E}}(t)\\ + \frac{1}{d_a}\int_{s^-}^{s^+}\Big(n_0\Big[J_-(s,t,1)\big[\mu_0(s,t,1) - \big(\mu_1(s,t,1)+\mu_T\big)\big]\\ + J_+(s,t,1)\big[\mu_1(s,t,1) - \mu_0(s,t,1)\big]\Big]\\ + (1-n_0)\Big[J_-(s,t,0)\big[\mu_0(s,t,0) - \big(\mu_1(s,t,0)+\mu_T\big)\big]\\ + J_+(s,t,0)\big[\mu_1(s,t,0) - \mu_0(s,t,0)\big]\Big]\Big)\,\mathrm{d}s\\ - \frac{k_BT}{d_a}\int_{s^-}^{s^+}\Big[|\dot{n}_0|_+\Big[\ln\left(\frac{P_1(s,t,0)}{P_1(s,t,1)}\right)P_1(s,t,0)\\ + \ln\left(\frac{1-P_1(s,t,0)}{1-P_1(s,t,1)}\right)\big(1-P_1(s,t,0)\big)\Big]\\ + |\dot{n}_0|_-\Big[\ln\left(\frac{P_1(s,t,1)}{P_1(s,t,0)}\right)P_1(s,t,1)\\ + \ln\left(\frac{1-P_1(s,t,1)}{1-P_1(s,t,0)}\right)\big(1-P_1(s,t,1)\big)\Big]\Big]\,\mathrm{d}s,\end{aligned}$$

which yields (20).

A.2 Coupling with a macroscopic continuous mechanical model

We now want to couple our model describing the microscopic interaction between actin and myosin to the macroscopic model of a muscle fibre. Let us define a domain Ω^0 in the reference configuration. We assume that the domain is subjected to a boundary traction $\mathbf{t}_N$ on the subpart of the boundary Γ_N. We introduce the rheology proposed in [Kimmig et al., 2019] in the realm of finite strains as presented in Figure 11. The upper branch models the one dimensional half-sarcomere of direction $\mathrm{f}_\mathbf{0}$.

The length change of the filaments due to their passive properties is accounted for by ℓ_s. Defining the extensions

$$e_c = \frac{x_c}{\ell_{hs}} \qquad \text{and} \qquad e_s = \frac{\ell_s}{\ell_{hs}},$$

the rheology assumes the following additive law to define the total 1D extension $e_{\mathrm{fib}} = e_s + e_c$. The tension in the branch is naturally given by

$$T_{\mathrm{fib}} = E_s e_s = T_c + \nu\dot{e}_c.$$

In this context, the filament sliding velocity $\dot{x}_c$, which appears in the microscopic dynamic equation, is given by $\ell_{hs}\dot{e}_c$.

The remaining part of the rheology models the 3D visco-hyperelastic passive properties of the tissue. The total second Piola-Kirchhoff stress tensor is given by $\mathbf{\Sigma} = \mathbf{\Sigma}_p + \mathbf{\Sigma}_a$ with

$$\mathbf{\Sigma}_p = \frac{\partial\Psi}{\partial\mathbf{e}} + \eta\dot{\mathbf{e}} \qquad \text{and} \qquad \mathbf{\Sigma}_a = \frac{T_{\mathrm{fib}}}{1+e_{\mathrm{fib}}}\mathrm{f}_\mathbf{0}\otimes\mathrm{f}_\mathbf{0},$$

where Ψ is the constitutive hyperelastic potential, η the 3D viscosity coefficient, $\mathbf{e}$ is the Green-Lagrange deformation tensor and $\mathrm{f}_\mathbf{0}$ the local fiber direction [Kimmig et al., 2019]. Note that the 1D extension and the 3D Green-Lagrange tensor are linked through the relation

$$1 + e_{\mathrm{fib}} = (1 + 2\mathrm{f}_\mathbf{0}\cdot\mathbf{e}\cdot\mathrm{f}_\mathbf{0})^{\frac{1}{2}}.$$

The principle of virtual work written on Ω^0 yields the macro-micro coupled model

$$
\begin{cases}
\displaystyle\int_{\Omega^0} \rho_0 \ddot{\mathbf{y}} \cdot \mathbf{w}\,\mathrm{d}\Omega + \int_{\Omega^0} \boldsymbol{\Sigma} : \mathrm{d}_{\mathbf{y}}\mathbf{e} \cdot \mathbf{w}\,\mathrm{d}\Omega = \int_{\Gamma_N} \mathbf{t}_N \cdot \mathbf{w}\,\mathrm{d}\Gamma, \quad \mathbf{w} \in \mathscr{V}_{\mathrm{ad}}, \\
\qquad \text{with } \boldsymbol{\Sigma} = \dfrac{\partial \Psi}{\partial \mathbf{e}} + \eta \dot{\mathbf{e}} + \dfrac{T_{\mathrm{fib}}}{(1 + 2\mathrm{f}_{\mathbf{0}} \cdot \mathbf{e} \cdot \mathrm{f}_{\mathbf{0}})^{\frac{1}{2}}} \mathrm{f}_{\mathbf{0}} \otimes \mathrm{f}_{\mathbf{0}}, \\
T_{\mathrm{fib}} = \nu \dot{e}_c + T_c = E_s e_s, \\
\qquad \text{with } T_c(\mathbf{x},t) = \dfrac{\rho_{\mathrm{surf}}}{d_a} \displaystyle\int_{s^-}^{s^+} \Big[n_0(\mathbf{x}, e_c) P_1(\mathbf{x}, s, t, 1) \\
\qquad\qquad + \big(1 - n_0(\mathbf{x}, e_c)\big) P_1(\mathbf{x}, s, t, 0) \Big] \dfrac{\partial w_1}{\partial s}(s,t)\mathrm{d}s, \ \mathbf{x} \in \Omega^0, \\
\dfrac{\partial P_1}{\partial t}(\mathbf{x}, s, t, 1) = -\dfrac{|\dot{n}_0|_+}{n_0} \big[P_1(\mathbf{x}, s, t, 1) - P_1(\mathbf{x}, s, t, 0) \big] \\
\qquad\qquad - \ell_{hs} \dot{e}_c(\mathbf{x}, t) \dfrac{\partial P_1}{\partial s}(\mathbf{x}, s, t, 1) \\
\qquad\qquad + \big(k_{+,1}(s) + k^{\mathrm{rev}}_{-,1}(s) \big) \big(1 - P_1(\mathbf{x}, s, t, 1) \big) \\
\qquad\qquad - \big(k_{-,1}(s) + k^{\mathrm{rev}}_{+,1}(s) \big) P_1(\mathbf{x}, s, t, 1) \\
\dfrac{\partial P_1}{\partial t}(\mathbf{x}, s, t, 0) = -\dfrac{|\dot{n}_0|_-}{1 - n_0} \big[P_1(\mathbf{x}, s, t, 0) - P_1(\mathbf{x}, s, t, 1) \big] \\
\qquad\qquad - \ell_{hs} \dot{e}_c(\mathbf{x}, t) \dfrac{\partial P_1}{\partial s}(\mathbf{x}, s, t, 0) \\
\qquad\qquad + \big(k_{+,0}(s) + k^{\mathrm{rev}}_{-,0}(s) \big) \big(1 - P_1(\mathbf{x}, s, t, 0) \big) \\
\qquad\qquad - \big(k_{-,0}(s) + k^{\mathrm{rev}}_{+,0}(s) \big) P_1(\mathbf{x}, s, t, 0)
\end{cases}
$$

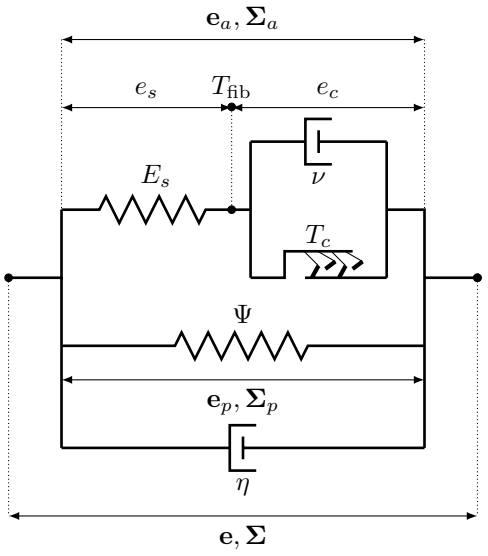

Figure 11: Tissue rheology. The upper branch represents the 1D filaments inside the sarcomere, which comprises the active cross-bridges represented here by the attached myosin heads. The lower branch represents the 3D passive visco-hyperelastic contribution of the remaining muscle cell constituents to the mechanical behavior. The rheology being constructed in the framework of finite strains, the constitutive elements are thus assembled together in a non-linear way.

A.3 Closed form expression of the ESPVR

The End Systolic Pressure Volume Relation (ESPVR) (V, P_V) is given in a parametric form by

$$\begin{cases} V = \frac{4}{3}\pi R_0^3\Big(1 + e_{\text{fib}} - \dfrac{\epsilon h(1+e_{\text{fib}})^{-2}}{2R_0}\Big)^3, \\ \Big(1 + e_{\text{fib}} - \dfrac{\epsilon}{2}(1+e_{\text{fib}})^{-2}\Big)^2\Big(1 + \epsilon(1+e_{\text{fib}})^{-3}\Big)P_V = \epsilon\big(1+e_{\text{fib}}\big)\Sigma_{\text{sph}}, \\ \Sigma_{\text{sph}} = \dfrac{\check{T}_c\big(n_0(e_c)\big)}{1+e_{\text{fib}}} + 4\big(1-(1+e_{\text{fib}})^{-6}\big)\dfrac{\partial \Psi}{\partial J_1} + 2\dfrac{\partial \Psi}{\partial J_4}, \\ J_1 = 2(1+e_{\text{fib}})^2 + (1+e_{\text{fib}})^{-4}, \\ J_4 = (1+e_{\text{fib}})^2, \\ e_{\text{fib}} = e_c + e_s, \\ E_s e_s = T_c\big(n_0(e_c)\big), \end{cases}$$

where R_0 is the radius of the ventricle in rest conditions, ϵ is the sphere aspect ratio defined as $\epsilon = h/R_0$ with h the ventricle wall thickness in the reference configuration, Σ_{sph} an effective stress quantity, J_1 and J_4 are the first and fourth reduced invariants of the Cauchy-Green strain tensor, respectively [Caruel et al., 2013b]. The first equation gives the volume of the spherical ventricle as a function of the fiber extension accounting for the wall thickness variation, the second one is the relation between the pressure inside the ventricle and the stress in the ventricular wall (an extension of Laplace's Law), the third equation gives the total – active and passive – stress as prescribed by the rheology, the fourth and fifth equations yield the tensor invariants for the chosen kinematics assumptions, and the sixth and seven equations reflect the kinematical assumptions and the mechanical equilibrium introduced by the one dimensional half-sarcomere part of the rheology, respectively.

A.4 Calibration

The calibration used for the cardiac simulation is presented in Table 1. Note that the reverse transition rates are directly derived from the detailed balance (3). The corresponding energy potentials and transition rates are displayed in Figure 12.

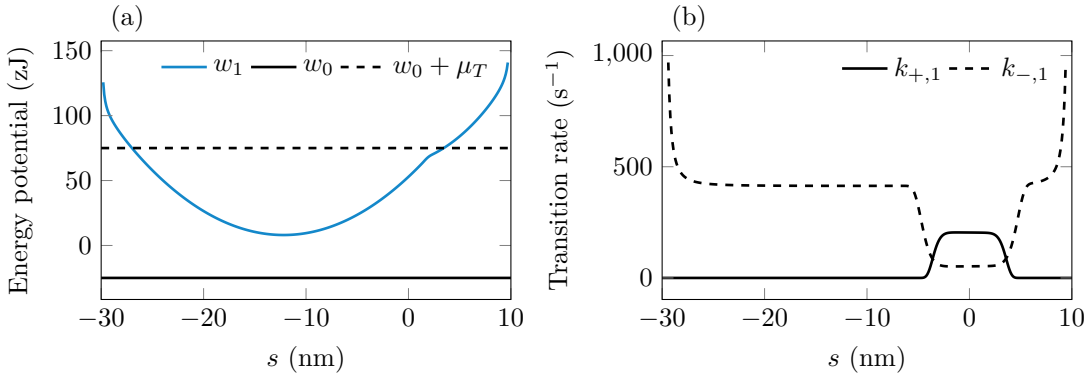

Figure 12: (a) Attached and detached energy potentials. (b) Forward transition rates for the pool $\gamma = 1$.

A.5 Proof of the equivalence between the random exchange model and the homogenized pool model

We detail here the proof that the stochastic model described by (25) and the homogenized pool model (10) are equivalent. For that, we look for the equation satisfied by $\mathbb{P}\big[\alpha^t = \overline{\alpha}, \gamma^t = \overline{\gamma}\big]$ in the stochastic random

Table 1: Calibration of the model for cardiac data.

Parameter	Symbol	Value
Energy potentials (see Figure 12(a))		
Attached potential energy w_1		
$w_1(s) = \hat{w}_1 + \alpha_w\Big(1/(s^+ - s) + 1/(s - s^-)\Big)$	α_w	$5\,\mathrm{zJ\,nm^{-1}}$
	$\hat{w}_1$	$62\,\mathrm{zJ}$
$\tilde{w}_1(s) = \begin{cases} \overline{\kappa}/2\,(s-\overline{s})^2 + \overline{w}_1 & \text{if } s < s_1, \\ \tilde{\kappa}/2\,(s-\tilde{s})^2 & \text{if } s > s_1, \\ \big(\overline{\kappa}/2\,(s_{1,\ell}-\overline{s})^2 + \overline{w}_1\big)\phi_1(s) & \\ + \quad \overline{\kappa}\,(s_{1,\ell}-\overline{s})\phi_2(s) & \\ + \quad \big(\tilde{\kappa}/2\,(s_{1,r}-\tilde{s})^2\big)\phi_3(s) & \\ + \quad \tilde{\kappa}\,(s_{1,r}-\tilde{s})\phi_4(s) & \\ + \quad \check{w}_1\phi_5(s) & \text{if } s \in [\overline{s}, \tilde{s}] \end{cases}$	$\overline{\kappa}$	$0.60\,\mathrm{pN\,nm^{-1}}$
	$\tilde{\kappa}$	$0.99\,\mathrm{pN\,nm^{-1}}$
	$\overline{s}$	$-12.2\,\mathrm{nm}$
	$\tilde{s}$	$-1.5\,\mathrm{nm}$
	$s_{1,\ell}$	$1.3\,\mathrm{nm}$
	$s_{1,r}$	$2.5\,\mathrm{nm}$
	$\check{w}_1$	$5.70\,\mathrm{zJ}$
$\overline{w}_1 = -\overline{\kappa}/2\,(s_1-\overline{s})^2 + \tilde{\kappa}/2\,(s_1-\tilde{s})^2$	s_1	$2\,\mathrm{nm}$
Interpolation functions		
$\begin{cases} \phi_1(s) &= (s-s_{1,r})^2/(s_{1,r}-s_{1,\ell})^2 \cdot \Big(2(s-s_{1,\ell})/(s_{1,r}-s_{1,\ell}) + 1\Big) \\ \phi_2(s) &= (s-s_{1,r})^2/(s_{1,r}-s_{1,\ell})^2 \cdot (s-s_{1,\ell}) \\ \phi_3(s) &= (s-s_{1,\ell})^2/(s_{1,r}-s_{1,\ell})^2 \cdot \Big(3 - 2(s-s_{1,\ell})/(s_{1,r}-s_{1,\ell})\Big) \\ \phi_4(s) &= (s-s_{1,\ell})^2/(s_{1,r}-s_{1,\ell})^2 \cdot (s-s_{1,r}) \\ \phi_5(s) &= \phi_1(s)\phi_3(s)/(\phi_1(s_1)\phi_3(s_1)) \end{cases}$		
Detached potential energy $w_0 = \hat{w}_0$	$\hat{w}_0$	$-25\,\mathrm{zJ}$
Transition rates (Figure 12(b))		
$\begin{cases} k_{+,1}(s) &= k_{\max}\exp\Big[-\lambda_1(s-s_k)^8 \\ &\quad + \alpha_{k,\mathrm{att}}\Big(1/(s^+-s)^2 + 1/(s-s^-)^2\Big)\Big] \\ k_{-,1}(s) &= k_{\mathrm{mid}} - (k_{\mathrm{mid}} - k_{\min})\exp\Big[-\lambda_2(s-s_k)^8 \\ &\quad + \alpha_{k,\mathrm{det}}\Big(1/(s^+-s)^2 + 1/(s-s^-)^2\Big) \\ k_{+,0}(s) &= 0.01 k_{+,1}(s) \\ k_{-,0}(s) &= k_{-,1}(s) \end{cases}$	$k_{\max}$	$206.5\,\mathrm{s^{-1}}$
	k_{mid}	$413\,\mathrm{s^{-1}}$
	$k_{\min}$	$50\,\mathrm{s^{-1}}$
	λ_1	$3.1 \times 10^{-6}\,/\mathrm{nm^8}$
	λ_2	$0.11 \times 10^{-6}\,/\mathrm{nm^8}$
	s_k	$0\,\mathrm{nm}$
	$\alpha_{k,\mathrm{att}}$	$1\,/\mathrm{s/nm^2}$
	$\alpha_{k,\mathrm{det}}$	$200\,/\mathrm{s/nm^2}$
Thermodynamics		
Temperature	T	$310\,\mathrm{K}$
ATP chemical potential	μ_T	$100\,\mathrm{zJ}$
Geometrical parameters		
Actin position interval left boundary	s^-	$-30\,\mathrm{nm}$
Actin position interval right boundary	s^+	$10\,\mathrm{nm}$
Sarcomere reference length	SL	$1.70\,\mu\mathrm{m}$

exchange model and we compare it to the corresponding equation in the homogenized pool model. To establish the former equation, we follow the procedure described in Le Bris & Lelievre [2009].

Let $\phi(\alpha, \gamma)$ be a test function. Denoting the joint probability $\mathbb{P}\big[\alpha^t = \overline{\alpha}, \gamma^t = \overline{\gamma}\big]$ by $\mathbb{P}_t\big[\overline{\alpha}, \overline{\gamma}\big]$, we have

$$\begin{aligned}\frac{\mathrm{d}}{\mathrm{d}t}\mathbb{E}\big[\phi(\alpha^t,\gamma^t)\big] &= \big[\phi(0,1)-\phi(1,1)\big]g_1\mathbb{P}_t\big[1,1\big] + \big[\phi(1,1)-\phi(0,1)\big]f_1\mathbb{P}_t\big[0,1\big] \\ &+ \big[\phi(0,0)-\phi(1,0)\big]g_0\mathbb{P}_t\big[1,0\big] + \big[\phi(1,0)-\phi(0,0)\big]f_0\mathbb{P}_t\big[0,0\big] \\ &+ \big[\phi(1,0)-\phi(1,1)\big]\frac{|\dot{n}_0(t)|_-}{n_0(t)}\mathbb{P}_t\big[1,1\big] + \big[\phi(0,0)-\phi(0,1)\big]\frac{|\dot{n}_0(t)|_-}{n_0(t)}\mathbb{P}_t\big[0,1\big] \\ &+ \big[\phi(1,1)-\phi(1,0)\big]\frac{|\dot{n}_0(t)|_+}{1-n_0(t)}\mathbb{P}_t\big[1,0\big] + \big[\phi(0,1)-\phi(0,0)\big]\frac{|\dot{n}_0(t)|_+}{1-n_0(t)}\mathbb{P}_t\big[0,0\big].\end{aligned} \tag{44}$$

Furthermore, the time derivative of the expectation is also given by

$$\frac{\mathrm{d}}{\mathrm{d}t}\mathbb{E}\big[\phi(\alpha^t,\gamma^t)\big] = \sum_{\alpha=\{0,1\}}\sum_{\gamma=\{0,1\}}\Big(\phi(\alpha^t,\gamma^t)\partial_t\mathbb{P}\big[\alpha^t,\gamma^t\big]\Big). \tag{45}$$

Since the test function can be chosen arbitrary, we can identify the coefficients of (44) and (45). We obtain

$$\left|\begin{aligned}\partial_t\mathbb{P}_t\big[1,1\big] &= -g_1\mathbb{P}_t\big[1,1\big] + f_1\mathbb{P}_t\big[0,1\big] + \frac{|\dot{n}_0(t)|_+}{1-n_0(t)}\mathbb{P}_t\big[1,0\big] - \frac{|\dot{n}_0(t)|_-}{n_0(t)}\mathbb{P}_t\big[1,1\big], \\ \partial_t\mathbb{P}_t\big[1,0\big] &= -g_0\mathbb{P}_t\big[1,0\big] + f_0\mathbb{P}_t\big[0,0\big] - \frac{|\dot{n}_0(t)|_+}{1-n_0(t)}\mathbb{P}_t\big[1,0\big] + \frac{|\dot{n}_0(t)|_-}{n_0(t)}\mathbb{P}_t\big[1,1\big], \\ \partial_t\mathbb{P}_t\big[0,1\big] &= g_1\mathbb{P}_t\big[1,1\big] - f_1\mathbb{P}_t\big[0,1\big] + \frac{|\dot{n}_0(t)|_+}{1-n_0(t)}\mathbb{P}_t\big[0,0\big] - \frac{|\dot{n}_0(t)|_-}{n_0(t)}\mathbb{P}_t\big[0,1\big], \\ \partial_t\mathbb{P}_t\big[0,0\big] &= g_0\mathbb{P}_t\big[1,0\big] - f_0\mathbb{P}_t\big[0,0\big] - \frac{|\dot{n}_0(t)|_+}{1-n_0(t)}\mathbb{P}_t\big[0,0\big] + \frac{|\dot{n}_0(t)|_-}{n_0(t)}\mathbb{P}_t\big[0,1\big].\end{aligned}\right. \tag{46}$$

Noting that we have

$$\left|\begin{aligned}\mathbb{P}_t\big[1,1\big] &= \mathbb{P}_t\big[1|1\big]\mathbb{P}_t\big[\gamma=1\big] = P_1(t,1)n_0(t), \\ \mathbb{P}_t\big[1,0\big] &= \mathbb{P}_t\big[1|0\big]\mathbb{P}_t\big[\gamma=0\big] = P_1(t,0)\cdot\big(1-n_0(t)\big), \\ \mathbb{P}_t\big[0,1\big] &= \mathbb{P}_t\big[0|1\big]\mathbb{P}_t\big[\gamma=1\big] = P_0(t,1)n_0(t), \\ \mathbb{P}_t\big[0,0\big] &= \mathbb{P}_t\big[0|0\big]\mathbb{P}_t\big[\gamma=0\big] = P_0(t,0)\cdot\big(1-n_0(t)\big).\end{aligned}\right.$$

and with the property

$$\dot{n}_0(t) = |\dot{n}_0(t)|_+ - |\dot{n}_0(t)|_-,$$

the system (46) becomes

$$\left|\begin{aligned}\frac{\partial}{\partial t}P_1(t,1) &= -g_1P_1(t,1) + f_1P_0(t,1) + \frac{|\dot{n}_0(t)|_+}{n_0(t)}P_1(t,0) - \frac{|\dot{n}_0(t)|_+}{n_0(t)}P_1(t,1), \\ \frac{\partial}{\partial t}P_1(t,0) &= -g_0P_1(t,0) + f_0P_0(t,0) - \frac{|\dot{n}_0(t)|_-}{1-n_0(t)}P_1(t,0) + \frac{|\dot{n}_0(t)|_-}{1-n_0(t)}P_1(t,1), \\ \frac{\partial}{\partial t}P_0(t,1) &= g_1P_1(t,1) - f_1P_0(t,1) + \frac{|\dot{n}_0(t)|_+}{n_0(t)}P_0(t,0) - \frac{|\dot{n}_0(t)|_+}{n_0(t)}P_0(t,1), \\ \frac{\partial}{\partial t}P_0(t,0) &= g_0P_1(t,0) - f_0P_0(t,0) - \frac{|\dot{n}_0(t)|_-}{1-n_0(t)}P_0(t,0) + \frac{|\dot{n}_0(t)|_-}{1-n_0(t)}P_0(t,1).\end{aligned}\right. \tag{47}$$

Moreover, we also have

$$\begin{aligned}P_1(t,1) + P_0(t,1) &= \frac{\mathbb{P}_t\big[1,1\big] + \mathbb{P}_t\big[0,1\big]}{n_0(t)} = 1, \\ P_1(t,0) + P_0(t,0) &= \frac{\mathbb{P}_t\big[1,0\big] + \mathbb{P}_t\big[0,0\big]}{1-n_0(t)} = 1.\end{aligned}$$

The system (47) becomes

$$\left|\begin{aligned}
&\frac{\partial}{\partial t}P_1(t,1) = -\frac{|\dot{n}_0(t)|_+}{n_0(t)}\Big[P_1(t,1) - P_1(t,0)\Big] - g_1 P_1(t,1) + f_1 P_0(t,1),\\
&\frac{\partial}{\partial t}P_1(t,0) = -\frac{|\dot{n}_0(t)|_-}{1-n_0(t)}\Big[P_1(t,0) - P_1(t,1)\Big] - g_0 P_1(t,0) + f_0 P_0(t,0),\\
&P_0(t,1) = 1 - P_1(t,1),\\
&P_0(t,0) = 1 - P_1(t,0).
\end{aligned}\right.$$

and we retrieve the equation system (10) in the absence of filament sliding. Our averaging assumption in the homogenized pool formulation is thus equivalent to an individual description of the myosin heads if the myosin heads that change pools are selected randomly.

A.6 Proof of the thermodynamical balances obtained at the discrete level

In this section, we detail the proof of the discrete thermodynamic balances presented in Section 5. The calculations are only performed for positive sliding velocities $v_c^{n+\frac{1}{2}\sharp}$ (i.e. $e_c^{n+1} \geq e_c^n$)). They can be straightforwardly extended to negative sliding velocities with a modification of the numerical scheme so that the transport term remains treated in an upwind manner.

A.6.1 First principle

We first aim at establishing a discrete counterpart to the continuous first principle (16). We discretize the attached state energy level on $[s^-, s^+]$ by

$$\left|\begin{aligned}
&w_{1,i} = w_1(s^- + i\delta s),\ i \in [\![1, \ell-1]\!]\\
&w_{1,\ell} = 150\, w_{1,\ell-1}.
\end{aligned}\right.$$

We define the discrete average energy per myosin head by

$$\mathcal{U}^{n,k} = \frac{\delta s}{d_a}\sum_{i=1}^{\ell}\Big[w_{1,i}\big(n_0^{n,k}a_i^{n,k} + (1-n_0^{n,k})b_i^{n,k}\big) + w_0\big(n_0^{n,k}(1-a_i^{n,k}) + (1-n_0^{n,k})(1-b_i^{n,k})\big)\Big].$$

We have at local time steps

$$\begin{aligned}
\frac{\mathcal{U}^{n,k+1}-\mathcal{U}^{n,k}}{\delta t} = \frac{\delta s}{d_a}\sum_{i=1}^{\ell}\Bigg(& w_{1,i}\Bigg[n_0^{n,k+1}\left(\frac{a_i^{n,k+1}-a_i^{n,k}}{\delta t}\right) + a_i^{n,k}\left(\frac{n_0^{n,k+1}-n_0^{n,k}}{\delta t}\right)\\
&+ (1-n_0^{n,k+1})\left(\frac{b_i^{n,k+1}-b_i^{n,k}}{\delta t}\right) + b_i^{n,k}\left(\frac{(1-n_0^{n,k+1})-(1-n_0^{n,k})}{\delta t}\right)\Bigg]\\
&+ w_0\Bigg[n_0^{n,k+1}\left(\frac{(1-a_i^{n,k+1})-(1-a_i^{n,k})}{\delta t}\right) + (1-a_i^{n,k})\left(\frac{n_0^{n,k+1}-n_0^{n,k}}{\delta t}\right)\\
&+ (1-n_0^{n,k+1})\left(\frac{(1-b_i^{n,k+1})-(1-b_i^{n,k})}{\delta t}\right)\\
&\qquad + (1-b_i^{n,k})\left(\frac{(1-n_0^{n,k+1})-(1-n_0^{n,k})}{\delta t}\right)\Bigg]\Bigg).
\end{aligned}$$

With the fluxes defined in (33) and the calculations done in [Kimmig et al., 2019] we obtain, using the

periodicity of the solution to handle the discrete transport term,

$$
\begin{aligned}
\frac{\mathcal{U}^{n,k+1}-\mathcal{U}^{n,k}}{\delta t} = \\
&\frac{\delta s}{d_a}\sum_{i=1}^{\ell}\Bigg(w_{1,i}\Bigg[n_0^{n,k+1}\Big(-\frac{|n_0^{n+1}-n_0^n|_+}{n_0^{n,k+1}\Delta t}\Big[a_i^{n,k}-b_i^{n,k}\Big]\Big)+a_i^{n,k}\left(\frac{n_0^{n,k+1}-n_0^{n,k}}{\delta t}\right)\\
&\quad+(1-n_0^{n,k+1})\Big(-\frac{|n_0^{n+1}-n_0^n|_-}{(1-n_0^{n,k+1})\Delta t}\Big[b_i^{n,k}-a_i^{n,k}\Big]\Big)+b_i^{n,k}\left(\frac{n_0^{n,k+1}-n_0^{n,k}}{\delta t}\right)\Bigg]\\
&\quad+w_0\Bigg[n_0^{n,k+1}\Big(\frac{|n_0^{n+1}-n_0^n|_+}{n_0^{n,k+1}\Delta t}\Big[a_i^{n,k}-b_i^{n,k}\Big]\Big)+(1-a_i^{n,k})\left(\frac{n_0^{n,k+1}-n_0^{n,k}}{\delta t}\right)\\
&\quad+(1-n_0^{n,k+1})\Big(\frac{|n_0^{n+1}-n_0^n|_-}{(1-n_0^{n,k+1})\Delta t}\Big[a_i^{n,k}-b_i^{n,k}\Big]\Big)\\
&\qquad\qquad+(1-b_i^{n,k})\left(\frac{n_0^{n,k+1}-n_0^{n,k}}{\delta t}\right)\Bigg]\Bigg)\\
&+v_c^{n+\frac{1}{2}\sharp}\frac{\delta s}{d_a}\sum_{i=1}^{\ell}\frac{w_{1,i+1}-w_{1,i}}{\delta s}\Big(n_0^{n,k+1}a^{n,k+1}+(1-n_0^{n,k+1})b^{n,k+1}\Big)\\
&+\frac{\delta s}{d_a}\sum_{i=1}^{\ell}\Big[\Big(n_0^{n,k+1}J_{+,1,i}^{n,k+1}+(1-n_0^{n,k+1})J_{+,0,i}^{n,k+1}\Big)(w_{1,i}-w_0)\\
&+\Big(n_0^{n,k+1}J_{-,1,i}^{n,k+1}+(1-n_0^{n,k+1})J_{-,0,i}^{n,k+1}\Big)\big(w_0-(w_{1,i}+\mu_T)\big)\Big]\\
&+\mu_T\frac{\delta s}{d_a}\sum_{i=1}^{\ell}\Big(n_0^{n,k+1}J_{-,1,i}^{n,k+1}+(1-n_0^{n,k+1})J_{-,0,i}^{n,k+1}\Big).
\end{aligned}
$$

Noting that

$$\frac{n_0^{n,k+1}-n_0^{n,k}}{\delta t}=\frac{n_0^{n+1}-n_0^n}{\Delta t},$$

and with the property (5), the pool exchange terms cancel out. We define the force per myosin head by

$$\tau_c^{n,k+1}=\frac{\delta s}{d_a}\sum_{i=1}^{\ell}\frac{w_{1,i+1}-w_{1,i}}{\delta s}\Big(n_0^{n,k+1}a^{n,k+1}+(1-n_0^{n,k+1})b^{n,k+1}\Big).$$

It is the average of the force between the two pools weighted by n_0. We finally obtain the first principle formulation at local time steps

$$\frac{\mathcal{U}^{n,k+1}-\mathcal{U}^{n,k}}{\delta t}=\frac{\mathcal{W}^{n,k+1}-\mathcal{W}^{n,k}}{\delta t}+\frac{\mathcal{Q}^{n,k+1}-\mathcal{Q}^{n,k}}{\delta t}+\frac{\mathcal{E}^{n,k+1}-\mathcal{E}^{n,k}}{\delta t},\tag{48}$$

with

$$
\left|\begin{aligned}
&\frac{\mathcal{W}^{n,k+1}-\mathcal{W}^{n,k}}{\delta t}=v_c^{n+\frac{1}{2}\sharp}\tau_c^{n,k+1},\\
&\frac{\mathcal{Q}^{n,k+1}-\mathcal{Q}^{n,k}}{\delta t}=\frac{\delta s}{d_a}\sum_{i=1}^{\ell}\Big[\Big(n_0^{n,k+1}J_{+,1,i}^{n,k+1}+(1-n_0^{n,k+1})J_{+,0,i}^{n,k+1}\Big)(w_{1,i}-w_0)\\
&\qquad\qquad+\Big(n_0^{n,k+1}J_{-,1,i}^{n,k+1}+(1-n_0^{n,k+1})J_{-,0,i}^{n,k+1}\Big)\big(w_0-(w_{1,i}+\mu_T)\big)\Big],\\
&\frac{\mathcal{E}^{n,k+1}-\mathcal{E}^{n,k}}{\delta t}=\mu_T\frac{\delta s}{d_a}\sum_{i=1}^{\ell}\Big(n_0^{n,k+1}J_{-,1,i}^{n,k+1}+(1-n_0^{n,k+1})J_{-,0,i}^{n,k+1}\Big).
\end{aligned}\right.
$$

A.6.2 Second principle

To derive a discrete version of the second principle, we recall the definition of the chemical potentials in each pool

$$\begin{vmatrix}\mu^{n,k}_{\alpha=1,\gamma=1,i} = \mu^{n,k}_{1,1,i} = w_{1,i} + k_B T \ln a_i^{n,k},\\ \mu^{n,k}_{\alpha=1,\gamma=0,i} = \mu^{n,k}_{1,0,i} = w_{1,i} + k_B T \ln b_i^{n,k},\\ \mu^{n,k}_{\alpha=0,\gamma=1,i} = \mu^{n,k}_{0,1,i} = w_0 + k_B T \ln(1-a_i^{n,k}),\\ \mu^{n,k}_{\alpha=0,\gamma=0,i} = \mu^{n,k}_{0,0,i} = w_0 + k_B T \ln(1-b_i^{n,k}).\end{vmatrix}$$

We define the entropy per myosin head as

$$\frac{\mathcal{S}^{n,k}}{k_B} = -\frac{\delta s}{d_a}\sum_{i=1}^{\ell}\Big[n_0^{n,k}\Big(a_i^{n,k}\ln a_i^{n,k} + (1-a_i^{n,k})\ln(1-a_i^{n,k})\Big) + (1-n_0^{n,k})\Big(b_i^{n,k}\ln b_i^{n,k} + (1-b_i^{n,k})\ln(1-b_i^{n,k})\Big)\Big].$$

Note that the entropy is well-defined for $a^{n,k} \in [0,1]$ and $b^{n,k} \in [0,1]$. For the derivation of the discrete second principle, we first assume that $a^{n,k} \in]0,1[$ and $b^{n,k} \in]0,1[$. We have

$$\begin{aligned}-\frac{1}{k_B}\frac{\mathcal{S}^{n,k+1}-\mathcal{S}^{n,k}}{\delta t} = \frac{\delta s}{d_a}\sum_{i=1}^{\ell}\Big[&n_0^{n,k+1}\Big(\frac{a_i^{n,k+1}-a_i^{n,k}}{\delta t}\ln a_i^{n,k+1} + a_i^{n,k}\frac{\ln a_i^{n,k+1}-\ln a_i^{n,k}}{\delta t}\Big)\\ &+ a_i^{n,k}\ln a_i^{n,k}\frac{n_0^{n,k+1}-n_0^{n,k}}{\delta t}\\ &+ n_0^{n,k+1}\Big(\frac{(1-a_i^{n,k+1})-(1-a_i^{n,k})}{\delta t}\ln(1-a_i^{n,k+1})\\ &\quad + (1-a_i^{n,k})\frac{\ln(1-a_i^{n,k+1})-\ln(1-a_i^{n,k})}{\delta t}\Big)\\ &+ (1-a_i^{n,k})\ln(1-a_i^{n,k})\frac{n_0^{n,k+1}-n_0^{n,k}}{\delta t}\\ &+ (1-n_0^{n,k+1})\Big(\frac{b_i^{n,k+1}-b_i^{n,k}}{\delta t}\ln b_i^{n,k+1} + b_i^{n,k}\frac{\ln b_i^{n,k+1}-\ln b_i^{n,k}}{\delta t}\Big)\\ &+ b_i^{n,k}\ln b_i^{n,k}\frac{(1-n_0^{n,k+1})-(1-n_0^{n,k})}{\delta t}\\ &+ (1-n_0^{n,k+1})\Big(\frac{(1-b_i^{n,k+1})-(1-b_i^{n,k})}{\delta t}\ln(1-b_i^{n,k+1})\\ &\quad + (1-b_i^{n,k})\frac{\ln(1-b_i^{n,k+1})-\ln(1-b_i^{n,k})}{\delta t}\Big)\\ &+ (1-b_i^{n,k})\ln(1-b_i^{n,k})\frac{(1-n_0^{n,k+1})-(1-n_0^{n,k})}{\delta t}\Big].\end{aligned}$$

We now consider the numerical scheme (29). Using the calculation made in [Kimmig et al., 2019], we

have

$$
\begin{aligned}
-\frac{1}{k_B}\frac{\mathcal{S}^{n,k+1}-\mathcal{S}^{n,k}}{\delta t} = & \\
& -\frac{1}{k_B}\frac{\tilde{\mathcal{S}}^{n,k+1}_{\text{prod}}-\tilde{\mathcal{S}}^{n,k}_{\text{prod}}}{\delta t}-\frac{1}{k_BT}\frac{\mathcal{Q}^{n,k+1}-\mathcal{Q}^{n,k}}{\delta t} \\
& +\frac{n_0^{n,k+1}-n_0^{n,k}}{\delta t}\frac{\delta s}{d_a}\sum_{i=1}^{\ell}\Big[a_i^{n,k}\ln a_i^{n,k}+(1-a_i^{n,k})\ln(1-a_i^{n,k}) \\
& \qquad -b_i^{n,k}\ln b_i^{n,k}-(1-b_i^{n,k})\ln(1-b_i^{n,k})\Big] \\
& -\frac{|n_0^{n,k+1}-n_0^{n,k}|_+}{\delta t}\frac{\delta s}{d_a}\sum_{i=1}^{\ell}\Big[\big[a_i^{n,k}-b_i^{n,k}\big]\ln a_i^{n,k+1} \\
& \qquad +\big[(1-a_i^{n,k})-(1-b_i^{n,k})\big]\ln(1-a_i^{n,k+1})\Big] \\
& -\frac{|n_0^{n,k+1}-n_0^{n,k}|_-}{\delta t}\frac{\delta s}{d_a}\sum_{i=1}^{\ell}\Big[\big[b_i^{n,k}-a_i^{n,k}\big]\ln b_i^{n,k+1} \\
& \qquad +\big[(1-b_i^{n,k})-(1-a_i^{n,k})\big]\ln(1-b_i^{n,k+1})\Big] \\
& +\frac{n_0^{n,k+1}\delta s}{d_a\delta t}\sum_{i=1}^{\ell}\left[a_i^{n,k}\ln\left(\frac{a_i^{n,k+1}}{a_i^{n,k}}\right)+(1-a_i^{n,k})\ln\left(\frac{1-a_i^{n,k+1}}{1-a_i^{n,k}}\right)\right] \\
& +\frac{(1-n_0^{n,k+1})\delta s}{d_a\delta t}\sum_{i=1}^{\ell}\left[b_i^{n,k}\ln\left(\frac{b_i^{n,k+1}}{b_i^{n,k}}\right)+(1-b_i^{n,k})\ln\left(\frac{1-b_i^{n,k+1}}{1-b_i^{n,k}}\right)\right],
\end{aligned}
$$

with

$$
\begin{aligned}
\frac{\tilde{\mathcal{S}}^{n,k+1}_{\text{prod}}-\tilde{\mathcal{S}}^{n,k}_{\text{prod}}}{\delta t} = & \\
& -\frac{n_0^{n,k+1}}{T}\left(\frac{\delta s}{d_a}\sum_{i=1}^{\ell}\left[J^{n,k+1}_{+,1,i}\left(\mu^{n,k+1}_{1,1,i}-\mu^{n,k+1}_{0,1,i}\right)+J^{n,k+1}_{-,1,i}\left(\mu^{n,k+1}_{0,1,i}-\mu^{n,k+1}_{1,1,i}-\mu_T\right)\right]\right. \\
& \qquad \left.+\frac{v_c^{n+\frac{1}{2}\sharp}k_BT}{d_a}\sum_{i=1}^{\ell}\left[a_i^{n,k+1}\ln\left(\frac{a_{i+1}^{n,k+1}}{a_i^{n,k+1}}\right)+(1-a_i^{n,k+1})\ln\left(\frac{1-a_{i+1}^{n,k+1}}{1-a_i^{n,k+1}}\right)\right]\right) \\
& -\frac{1-n_0^{n,k+1}}{T}\left(\frac{\delta s}{d_a}\sum_{i=1}^{\ell}\left[J^{n,k+1}_{+,0,i}\left(\mu^{n,k+1}_{1,0,i}-\mu^{n,k+1}_{0,0,i}\right)\right.\right. \\
& \qquad \left.\left.+J^{n,k+1}_{-,0,i}\left(\mu^{n,k+1}_{0,0,i}-\mu^{n,k+1}_{1,0,i}-\mu_T\right)\right]\right. \\
& \qquad \left.+\frac{v_c^{n+\frac{1}{2}\sharp}k_BT}{d_a}\sum_{i=1}^{\ell}\left[b_i^{n,k+1}\ln\left(\frac{b_{i+1}^{n,k+1}}{b_i^{n,k+1}}\right)+(1-b_i^{n,k+1})\ln\left(\frac{1-b_{i+1}^{n,k+1}}{1-b_i^{n,k+1}}\right)\right]\right)
\end{aligned}
$$

which is positive from the calculation made in [Kimmig et al., 2019], given that $1-n_0^{n,k+1}\geq 0$ and $n_0^{n,k+1}\geq 0$.

We first assume that $n_0^{n,k+1} \geq n_0^{n,k}$. We have

$$\begin{aligned}
\frac{1}{k_B}\frac{\mathcal{S}^{n,k+1}-\mathcal{S}^{n,k}}{\delta t} = \\
&\frac{1}{k_B}\frac{\tilde{\mathcal{S}}_{\text{prod}}^{n,k+1}-\tilde{\mathcal{S}}_{\text{prod}}^{n,k}}{\delta t} + \frac{1}{k_B T}\frac{\mathcal{Q}^{n,k+1}-\mathcal{Q}^{n,k}}{\delta t} \\
&\quad - \frac{n_0^{n,k+1}-n_0^{n,k}}{\delta t}\frac{\delta s}{d_a}\sum_{i=1}^{\ell}\left[b_i^{n,k}\ln\left(\frac{a_i^{n,k+1}}{b_i^{n,k}}\right) + (1-b_i^{n,k})\ln\left(\frac{1-a_i^{n,k+1}}{1-b_i^{n,k}}\right)\right] \\
&\quad + \frac{n_0^{n,k}}{\delta t}\frac{\delta s}{d_a}\sum_{i=1}^{\ell}\left[a_i^{n,k}\ln\left(\frac{a_i^{n,k}}{a_i^{n+1,k}}\right) + (1-a_i^{n,k})\ln\left(\frac{1-a_i^{n,k}}{1-a_i^{n,k+1}}\right)\right] \\
&\quad + \frac{1-n_0^{n,k+1}}{\delta t}\frac{\delta s}{d_a}\sum_{i=1}^{\ell}\left[b_i^{n,k+1}\ln\left(\frac{b_i^{n,k+1}}{b_i^{n,k}}\right) + (1-b_i^{n,k+1})\ln\left(\frac{1-b_i^{n,k+1}}{1-b_i^{n,k}}\right)\right].
\end{aligned}$$

With the property that $a^{n,k} \in]0,1[$ and $b^{n,k} \in]0,1[$, we can use the convexity inequalities (22) and (23), and, noting that we have

$$\left|\begin{array}{r} n_0^{n,k+1}-n_0^{n,k} \geq 0, \\ 1-n_0^{n,k+1} \geq 0, \\ n_0^{n,k+1} \geq 0, \end{array}\right.$$

we obtain

$$\frac{\mathcal{S}^{n,k+1}-\mathcal{S}^{n,k}}{\delta t} = \frac{\mathcal{S}_{\text{prod}}^{n,k+1}-\mathcal{S}_{\text{prod}}^{n,k}}{\delta t} + \frac{1}{T}\frac{\mathcal{Q}^{n,k+1}-\mathcal{Q}^{n,k}}{\delta t}, \tag{49}$$

with the entropy creation term

$$\begin{aligned}
&\frac{1}{k_B}\frac{\mathcal{S}_{\text{prod}}^{n,k+1}-\mathcal{S}_{\text{prod}}^{n,k}}{\delta t} \\
&\qquad = \frac{1}{k_B}\frac{\tilde{\mathcal{S}}_{\text{prod}}^{n,k+1}-\tilde{\mathcal{S}}_{\text{prod}}^{n,k}}{\delta t} \\
&\qquad\quad - \frac{n_0^{n,k+1}-n_0^{n,k}}{\delta t}\frac{\delta s}{d_a}\sum_{i=1}^{\ell}\left[b_i^{n,k}\ln\left(\frac{a_i^{n,k+1}}{b_i^{n,k}}\right) + (1-b_i^{n,k})\ln\left(\frac{1-a_i^{n,k+1}}{1-b_i^{n,k}}\right)\right] \\
&\qquad\quad + \frac{n_0^{n,k}}{\delta t}\frac{\delta s}{d_a}\sum_{i=1}^{\ell}\left[a_i^{n,k}\ln\left(\frac{a_i^{n,k}}{a_i^{n,k+1}}\right) + (1-a_i^{n,k})\ln\left(\frac{1-a_i^{n,k}}{1-a_i^{n,k+1}}\right)\right] \\
&\qquad\quad - \frac{1-n_0^{n,k+1}}{\delta t}\frac{\delta s}{d_a}\sum_{i=1}^{\ell}\left[b_i^{n,k+1}\ln\left(\frac{b_i^{n,k+1}}{b_i^{n,k}}\right) + (1-b_i^{n,k+1})\ln\left(\frac{1-b_i^{n,k+1}}{1-b_i^{n,k}}\right)\right]
\end{aligned}$$

satisfying the inequality

$$\frac{\mathcal{S}_{\text{prod}}^{n,k+1}-\mathcal{S}_{\text{prod}}^{n,k}}{\delta t} \geq 0. \tag{50}$$

Similarly, we have, for $n_0^{n,k+1} < n_0^{n,k}$, the second principle (49) with

$$\begin{aligned}\frac{1}{k_B}\frac{\mathcal{S}_{\text{prod}}^{n,k+1}-\mathcal{S}_{\text{prod}}^{n,k}}{\delta t} = &\\ &\frac{1}{k_B}\frac{\tilde{\mathcal{S}}_{\text{prod}}^{n,k+1}-\tilde{\mathcal{S}}_{\text{prod}}^{n,k}}{\delta t}\\ &-\frac{n_0^{n,k+1}-n_0^{n,k}}{\delta t}\frac{\delta s}{d_a}\sum_{i=1}^{\ell}\left[a_i^{n,k}\ln\left(\frac{a_i^{n,k}}{b_i^{n,k+1}}\right)+(1-a_i^{n,k})\ln\left(\frac{1-a_i^{n,k}}{1-b_i^{n,k+1}}\right)\right]\\ &-\frac{n_0^{n,k+1}}{\delta t}\frac{\delta s}{d_a}\sum_{i=1}^{\ell}\left[a_i^{n,k}\ln\left(\frac{a_i^{n,k+1}}{a_i^{n,k}}\right)+(1-a_i^{n,k})\ln\left(\frac{1-a_i^{n,k+1}}{1-a_i^{n,k}}\right)\right]\\ &-\frac{1-n_0^{n,k}}{\delta t}\frac{\delta s}{d_a}\sum_{i=1}^{\ell}\left[b_i^{n,k}\ln\left(\frac{b_i^{n,k+1}}{b_i^{n,k}}\right)+(1-b_i^{n,k})\ln\left(\frac{1-b_i^{n,k+1}}{1-b_i^{n,k}}\right)\right],\end{aligned}$$

which satisfies the positivity of the entropy creation property (50). In summary, we have

$$\frac{\mathcal{S}^{n,k+1}-\mathcal{S}^{n,k}}{\delta t}\geq\frac{1}{T}\frac{\mathcal{Q}^{n,k+1}-\mathcal{Q}^{n,k}}{\delta t},\ \text{for } a^{n,k}\in]0,1[\text{ and } b^{n,k}\in]0,1[,\ n\in N,\ k\in[\![0,N]\!]. \tag{51}$$

Noting that the heat transfer rate term and the entropy rate term are properly defined for $a^{n,k}\in[0,1]$ and $b^{n,k}\in[0,1]$, we pass to the limit in the inequality (51) and we obtain

$$\frac{\mathcal{S}^{n,k+1}-\mathcal{S}^{n,k}}{\delta t}\geq\frac{1}{T}\frac{\mathcal{Q}^{n,k+1}-\mathcal{Q}^{n,k}}{\delta t},\ \text{for } a^{n,k}\in[0,1]\text{ and } b^{n,k}\in[0,1],\ n\in N,\ k\in[\![0,N]\!].$$

A.6.3 Numerical validation

We present in this section the numerical computation of the residuals (48) and (49) corresponding to the discrete thermodynamics balances (34) and (37) defined as

$$\left|\begin{aligned}e_{\mathcal{U}}^{n+\frac{1}{2}\sharp}&=\frac{\mathcal{U}^{n+1}-\mathcal{U}^{n}}{\delta t}-\frac{\mathcal{W}^{n+1}-\mathcal{W}^{n}}{\delta t}-\frac{\mathcal{Q}^{n+1}-\mathcal{Q}^{n}}{\delta t}-\frac{\mathcal{E}^{n+1}-\mathcal{E}^{n}}{\delta t},\\ e_{\mathcal{F}}^{n+\frac{1}{2}\sharp}&=\frac{\mathcal{F}^{n+1}-\mathcal{F}^{n}}{\delta t}-\frac{\mathcal{W}^{n+1}-\mathcal{W}^{n}}{\delta t}-\frac{\mathcal{E}^{n+1}-\mathcal{E}^{n}}{\delta t}-T\frac{\mathcal{S}_{\text{prod}}^{n+1}-\mathcal{S}_{\text{prod}}^{n}}{\delta t}.\end{aligned}\right. \tag{52}$$

It may serve as a validation of the algebraic derivation of the first and second thermodynamic balances, as well as a validation of the correct implementation of the proposed numerical scheme. The results are presented in Figure 13.

We can notice that the value of the residuals are eight orders of magnitude lower that the various terms that compose them (see Figure 6). We conclude that the observed oscillations solely reflect the numerical noise. It therefore substantiates our derivation of the discrete thermodynamics principles.

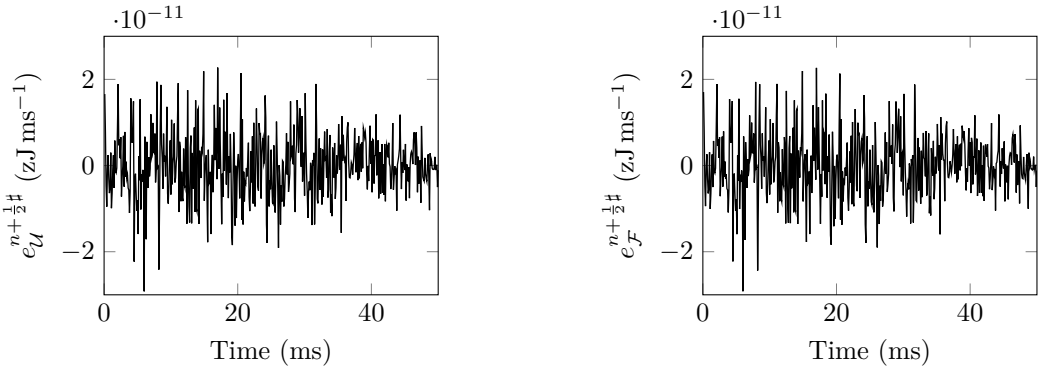

Figure 13: Numerical evaluation of the discrete thermodynamic residuals (52) during the simulation presented in Figure 6. For this simulation, we used $\Delta t = 0.001\,\mathrm{s}$ and $\delta t = \Delta t$.

References

Amiad Pavlov, D., & Landesberg, A. (2016). The cross-bridge dynamics is determined by two length-independent kinetics: Implications on muscle economy and Frank–Starling Law. *Journal of molecular and cellular cardiology*, *90*, 94–101.

Baillargeon, B., Rebelo, N., Fox, D.D., Taylor, R.L., & Kuhl, E. (2014). The Living Heart Project: A robust and integrative simulator for human heart function. *European Journal of Mechanics / A Solids*, *48*(C), 38–47.

Caremani, M., Melli, L., Dolfi, M., Lombardi, V., & Linari, M. (2015). Force and number of myosin motors during muscle shortening and the coupling with the release of the ATP hydrolysis products. *The Journal of Physiology*, *593*(15), 3313–3332.

Caremani, M., Pinzauti, F., Reconditi, M., Piazzesi, G., Stienen, G.J.M., Lombardi, V., & Linari, M. (2016). Size and speed of the working stroke of cardiac myosin in situ. *Proceedings of the National Academy of Sciences*, *113*(13), 3675–3680.

Caruel, M., Allain, J.-M., & Truskinovsky, L. (2013a). Muscle as a Metamaterial Operating Near a Critical Point. *Physical review letters*, *110*(24), 248103.

Caruel, M., Chabiniok, R., Moireau, P., Lecarpentier, Y., & Chapelle, D. (2013b). Dimensional reductions of a cardiac model for effective validation and calibration. *Biomechanics and Modeling in Mechanobiology*, *13*(4), 897–914.

Caruel, M., Moireau, P., & Chapelle, D. (2019). Stochastic modeling of chemical-mechanical coupling in striated muscles. *Biomechanics and Modeling in Mechanobiology*, *18*(3), 563–587.

Chabiniok, R., Moireau, P., Lesault, P.F., Rahmouni, A., Deux, J.F., & Chapelle, D. (2012). Estimation of tissue contractility from cardiac cine-MRI using a biomechanical heart model. *Biomechanics and Modeling in Mechanobiology*, *11*(5), 609–630.

Chabiniok, R., Wang, V.Y., Hadjicharalambous, M., Asner, L., Lee, J., Sermesant, M., Kuhl, E., Young, A.A., Moireau, P., Nash, M.P., Chapelle, D., & Nordsletten, D.A. (2016). Multiphysics and multiscale modelling, data-model fusion and integration of organ physiology in the clinic: ventricular cardiac mechanics. *Interface focus*, *6*(2), 20150083.

Chapelle, D., Le Tallec, P., Moireau, P., & Sorine, M. (2012). Energy-preserving muscle tissue model: formulation and compatible discretizations. *Journal for Multiscale Computational Engineering*.

de Tombe, P.P., Mateja, R.D., Tachampa, K., Mou, YA, Farman, G.P., & Irving, T.C. (2010). Myofilament length dependent activation. *Journal of molecular and cellular cardiology*, *48*(5), 851–858.

de Tombe, P.P., & Stienen, G.J.M. (2007). Impact of temperature on cross-bridge cycling kinetics in rat myocardium. *The Journal of Physiology*, *584*(2), 591–600.

de Tombe, P.P., & ter Keurs, H.E.D.J. (1992). An internal viscous element limits unloaded velocity of sarcomere shortening in rat myocardium. *The Journal of Physiology*, *454*(1), 619–642.

de Tombe, P.P., & ter Keurs, H.E.D.J. (2016). Cardiac muscle mechanics: Sarcomere length matters. *Journal of molecular and cellular cardiology*, *91*(C), 148–150.

Dobesh, D.P., Konhilas, J.P., & de Tombe, P.P. (2002). Cooperative activation in cardiac muscle: impact of sarcomere length. *AJP: Heart and Circulatory Physiology*, *282*(3), H1055–H1062.

Eisenberg, E., & Hill, T.L. (1978). A cross-bridge model of muscle contraction. *Progress in biophysics and molecular biology*, *33*(1), 55–82.

Eisenberg, E., Hill, T.L., & Chen, Y. (1980). Cross-bridge model of muscle contraction. Quantitative analysis. *Biophysical Journal*, *29*(2), 195–227.

Frank, O. (1895). *Zur Dynamik des Herzmuskels*, vol. 32. Zeitschrift für Biologie.

Gsell, M.A.F., Augustin, C.M., Prassl, A.J., Karabelas, E., Fernandes, J.F., Kelm, M., Goubergrits, L., Kuehne, T., & Plank, G. (2018). Assessment of wall stresses and mechanical heart power in the left ventricle: Finite element modeling versus Laplace analysis. *International Journal for Numerical Methods in Biomedical Engineering*, *34*(12), e3147.

Hill, T.L. (1977). *Free Energy Transduction in Biology*. Academic Press.

Hirschvogel, M., Bassilious, M., Jagschies, L., Wildhirt, S.M., & Gee, M.W. (2017). A monolithic 3D-0D coupled closed-loop model of the heart and the vascular system: Experiment-based parameter estimation for patient-specific cardiac mechanics. *International Journal for Numerical Methods in Biomedical Engineering*, *84*(3), e2842–22.

Hussan, J, de Tombe, P P, & Rice, J J (2006). A spatially detailed myofilament model as a basis for large-scale biological simulations. *IBM journal of research and ...*, *50*(6), 583–600.

Huxley, A.F. (1957). Muscle structures and theories of contraction. *Progr. Biophys. Chem.*.

Huxley, A.F., & Simmons, R.M. (1971). Proposed mechanism of force generation in striated muscle. *Nature*.

Kentish, J.C., Ter Keurs, H.E.D.J., Ricciardi, L., Bucx, J.J., & Noble, M.I. (1986). Comparison between the sarcomere length-force relations of intact and skinned trabeculae from rat right ventricle. influence of calcium concentrations on these relations. *Circulation research*, *58*(6), 755–768.

Kimmig, F., & Caruel, M. (2019). Hierarchical modeling of muscle contraction. *submitted*.

Kimmig, F., Chapelle, D., & Moireau, P. (2019). Thermodynamic properties of muscle contraction models and associated discrete-time principles. *Advanced Modeling and Simulation in Engineering Sciences*, *6*(1), 6.

Le Bris, Claude, & Lelievre, Tony (2009). Multiscale modelling of complex fluids: a mathematical initiation. In *Multiscale modeling and simulation in science*, (pp. 49–137). Springer.

Le Gall, A., Vallée, F., Mebazaa, A., Chapelle, D., Gayat, E., & Chabiniok, R. (2020). Monitoring of cardiovascular physiology augmented by a patient-specific biomechanical model during general anaesthesia. a proof of concept study. *PloS ONE, Public Library of Science, in press*, *15*(5), e0232830.

Månsson, Alf (2010). Actomyosin-ADP states, interhead cooperativity, and the force-velocity relation of skeletal muscle. *Biophysical Journal*, *98*(7), 1237–1246.

Marcucci, L., & Truskinovsky, L. (2010). Mechanics of the power stroke in myosin II. *Physical Review E*, *81*(5), 051915–8.

Marcucci, L., Washio, T., & Yanagida, T. (2016). Including thermal fluctuations in actomyosin stable states increases the predicted force per motor and macroscopic efficiency in muscle modelling. *PLoS Computational Biology*, *12*(9).

Marcucci, L., Washio, T., & Yanagida, T. (2017). Titin-mediated thick filament activation, through a mechanosensing mechanism, introduces sarcomere-length dependencies in mathematical models of rat trabecula and whole ventricle. *Scientific Reports*, (pp. 1–10).

Marcucci, L., & Yanagida, T. (2012). From Single Molecule Fluctuations to Muscle Contraction: A Brownian Model of A.F. Huxley's Hypotheses. *PLoS ONE*, *7*(7), e40042–8.

Mateja, R.D., & de Tombe, P.P. (2012). Myofilament Length-Dependent Activation Develops within 5 ms in Guinea-Pig Myocardium. *Biophysical Journal*, *103*(1), L13–L15.

Niestrawska, J.A., Augustin, C.M., & Plank, G. (2020). Computational modeling of cardiac growth and remodeling in pressure overloaded hearts—Linking microstructure to organ phenotype. *Acta Biomaterialia*, *106*, 34–53.

Patterson, S.W., & Starling, E.H. (1914). On the mechanical factors which determine the output of the ventricles. *The Journal of Physiology*, *48*(5), 357–379.

Pertici, I., Bongini, L., Melli, L., Bianchi, G., Salvi, L., Falorsi, G., Squarci, C., Bozó, T., Cojoc, D., Kellermayer, M.S.Z., Lombardi, V., & Bianco, P. (2018). A myosin II nanomachine mimicking the striated muscle. *Nature Communications*, (pp. 1–10).

Peskin, C.S. (1975). *Mathematical aspects of heart physiology*. Courant Institute of Mathematical Sciences - NYU.

Piazzesi, G., & Lombardi, V. (1995). A cross-bridge model that is able to explain mechanical and energetic properties of shortening muscle. *Biophysical Journal*, *68*, 1966–1979.

Pinzauti, F., Pertici, I., Reconditi, M., Narayanan, T., Stienen, G.J.M., Piazzesi, G., Lombardi, V., Linari, M., & Caremani, M. (2018). The force and stiffness of myosin motors in the isometric twitch of a cardiac trabecula and the effect of the extracellular calcium concentration. *The Journal of Physiology*, *596*(13), 2581–2596.

Quarteroni, A., Lassila, T., Rossi, S., & Ruiz-Baier, R. (2017). Integrated Heart-Coupling multiscale and multiphysics models for the simulation of the cardiac function. *Computer Methods in Applied Mechanics and Engineering*, *314*, 345–407.

Reconditi, M., Caremani, M., Pinzauti, F., Powers, J.D., Narayanan, T., Stienen, G.J.M., Linari, M., Lombardi, V., & Piazzesi, G. (2017). Myosin filament activation in the heart is tuned to the mechanical task. *Proceedings of the National Academy of Sciences*, (pp. 3240–3245).

Regazzoni, F., Dede', L., & Quarteroni, A. (2018). Active contraction of cardiac cells: a reduced model for sarcomere dynamics with cooperative interactions. *Biomechanics and Modeling in Mechanobiology*, (pp. 1–24).

Regazzoni, Francesco, Dedè, Luca, & Quarteroni, Alfio (2020). Biophysically detailed mathematical models of multiscale cardiac active mechanics. *PLOS Computational Biology*, *16*(10), e1008294.

Rice, J.J., & de Tombe, P.P. (2004). Approaches to modeling crossbridges and calcium-dependent activation in cardiac muscle. *Progress in biophysics and molecular biology*, *85*(2-3), 179–195.

Rice, J.J., Stolovitzky, G., Tu, Y., & de Tombe, P.P. (2003). Ising Model of Cardiac Thin Filament Activation with Nearest-Neighbor Cooperative Interactions. *Biophysical Journal*, *84*(2), 897–909.

Rice, J.J., Wang, F., Bers, D.M., & de Tombe, P.P. (2008). Approximate Model of Cooperative Activation and Crossbridge Cycling in Cardiac Muscle Using Ordinary Differential Equations. *Biophysical Journal*, *95*(5), 2368–2390.

Rossi, S., Lassila, T., Ruiz-Baier, R., Sequeira, A., & Quarteroni, A. (2014). Thermodynamically consistent orthotropic activation model capturing ventricular systolic wall thickening in cardiac electromechanics. *European Journal of Mechanics / A Solids*, *48*(C), 129–142.

Sequeira, V., & Velden, J. (2017). The Frank–Starling Law: a jigsaw of titin proportions. *Biophysical reviews*, *9*(3), 259–267.

Silverthorn, D.U., Ober, W.C., Garrison, C.W., & Silverthorn, A.C. (2009). *Human physiology: an integrated approach*. Pearson.

Sugiura, S., Washio, T., Hatano, A., Okada, J., Watanabe, H., & Hisada, T. (2012). Multi-scale simulations of cardiac electrophysiology and mechanics using the University of Tokyo heart simulator. *Progress in biophysics and molecular biology*, *110*(2-3), 380–389.

ter Keurs, H.E.D.J., Shinozaki, T., Zhang, Y.M., Zhang, M.L., Wakayama, Y., Sugai, Y., Kagaya, Y., Miura, M., Boyden, P.A., Stuyvers, B.D.M., & Landesberg, A. (2008). Sarcomere mechanics in uniform and non-uniform cardiac muscle: A link between pump function and arrhythmias. *Progress in biophysics and molecular biology*, *97*(2-3), 312–331.

van der Velden, J., de Jong, J.W., Owen, V.J., Burton, P.B., & Stienen, G.J. (2000). Effect of protein kinase A on calcium sensitivity of force and its sarcomere length dependence in human cardiomyocytes. *Cardiovascular Research*, *46*(3), 487–495.

Wannenburg, T., Janssen, P.M., Fan, D., & de Tombe, P.P. (1997). The Frank-Starling mechanism is not mediated by changes in rate of cross-bridge detachment. *The American journal of physiology*, *273*(5 Pt 2), H2428–35.

Washio, T., Okada, J.-I., Sugiura, S., & Hisada, T. (2011). Approximation for Cooperative Interactions of a Spatially-Detailed Cardiac Sarcomere Model. *Cellular and Molecular Bioengineering*, *5*(1), 113–126.

Zahalak, G.I., & Motabarzadeh, I. (1997). A Re-examination of Calcium Activation in the Huxley Cross-Bridge Model. *Journal of Biomechanical Engineering*, *119*(1), 20–29.

Zahalak, G I (2000). The two-state cross-bridge model of muscle is an asymptotic limit of multi-state models. *Journal of Theoretical Biology*.